NASA TECHNICAL NOTE

NASA TN D-3644

$c.\ 1$

HEAT-TRANSFER AND PRESSURE DISTRIBUTIONS ON 60° AND 70° SWEPT DELTA WINGS HAVING TURBULENT BOUNDARY LAYERS

by William M. Murray, Jr., and Robert L. Stallings, Jr.

Langley Research Center
Langley Station, Hampton, Va.

NATIONAL AERONAUTICS AND SPACE ADMINISTRATION • WASHINGTON, D. C. • OCTOBER 1966

HEAT-TRANSFER AND PRESSURE DISTRIBUTIONS

ON 60° AND 70° SWEPT DELTA WINGS HAVING

TURBULENT BOUNDARY LAYERS

By William M. Murray, Jr., and Robert L. Stallings, Jr.

Langley Research Center
Langley Station, Hampton, Va.

NATIONAL AERONAUTICS AND SPACE ADMINISTRATION

HEAT-TRANSFER AND PRESSURE DISTRIBUTIONS

ON 60° AND 70° SWEPT DELTA WINGS HAVING

TURBULENT BOUNDARY LAYERS

By William M. Murray, Jr., and Robert L. Stallings, Jr.
Langley Research Center

SUMMARY

Heat-transfer and pressure distributions were obtained on 60° and 70° swept delta wings with sharp and blunt wing leading edges in the Langley Unitary Plan wind tunnel. All models were tested with an artificially tripped boundary layer at Mach numbers of 2.98, 3.71, and 4.44 at nominal Reynolds numbers per meter of 9.85×10^6 and 19.7×10^6 and through an angle-of-attack range from -10° to 10°.

For angles of attack from 0° to 10° (instrumentation windward) both the magnitude and distribution of heat-transfer measurements throughout the range of test conditions were generally in good agreement with turbulent flat-plate theory. Heat-transfer and pressure measurements and oil-flow photographs revealed the presence of a vortex formation over the leeward surface for Mach numbers of 2.98 and 3.71, nominal Reynolds numbers per meter of 9.85×10^6 and 19.7×10^6, and angles of attack of -5° and -10°. Throughout the range of test conditions there was no noticeable effect on either the heat-transfer or pressure measurements when the leading-edge radius of both wings was increased from a sharp leading edge to a cylindrical leading edge of 0.635-centimeter radius.

INTRODUCTION

A winged vehicle in high-altitude, high-speed flight will most likely have a fully developed turbulent boundary layer over a large portion of its wing surface. The extent of this turbulent flow will be influenced by many factors including Mach number, Reynolds number, angle of attack, and the geometric design of the vehicle. This geometric design includes such things as (1) sweep angle of the wing leading edge, (2) degree of leading-edge bluntness, (3) amount of dihedral, and (4) airfoil shape.

The delta planform appears to be a logical choice for such a vehicle, hence information concerning the heating and pressure distributions for a turbulent boundary layer on such a wing might be highly useful. Available information about the aerodynamic heating

on the surface of delta wings is very limited. Previous investigations (refs. 1 to 16) have resulted in large amounts of data in the laminar and transitional regimes and little or no data under conditions of turbulent boundary-layer flow. No known previous attempt has been made to study, in detail, the fully turbulent heating and pressure distributions on delta wings with sharp and blunt leading edges.

The purpose of this test was to obtain and analyze turbulent heat-transfer and pressure data on two delta-planform wings having no dihedral, sweep angles of 60° and 70°, and leading-edge radii of ≈0, 0.317, and 0.635 centimeter. These wings were tested with an artificially tripped boundary layer through an angle-of-attack range from -10° to 10° at Mach numbers of 2.98, 3.71, and 4.44. The nominal Reynolds number per meter was 9.85×10^6 and 19.7×10^6, yielding a maximum Reynolds number based on center-line chord of about 17×10^6.

SYMBOLS

A	aspect ratio
c	specific heat of model skin, joules per (kilogram)(degree Kelvin)
h	heat-transfer coefficient, joules per (meter^2)(second)(degree Kelvin)
l	characteristic dimension of blunt leading edges, centimeters (see fig. 3)
M	Mach number
p	pressure, newtons per meter^2
r	wing leading-edge radius, centimeters
R	Reynolds number per unit length, 1/meter
s	distance behind wing leading edge, parallel to wing center line, meters or centimeters as noted
t	time, seconds
T	temperature, degrees Kelvin
V	velocity, meters per second
W	weight of model skin per unit area, kilograms per meter^2

2

y   spanwise coordinate, meters or centimeters as noted

z   coordinate perpendicular to wing surface, meters or centimeters as noted

α angle of attack, degrees

$\beta = \sqrt{M_\infty^2 - 1}$

Λ wing leading-edge sweep angle, degrees

Subscripts:

e   equilibrium conditions

l local conditions

t   stagnation conditions

w   wall conditions

∞ free-stream conditions

0,1,2,3, . . .,n   time sequence

MODELS AND INSTRUMENTATION

The models used in this investigation were 60° and 70° delta wings with zero dihedral and leading-edge radii of ≈ 0, 0.317, and 0.635 cm.

Models 1 and 2, shown in figures 1(a), 1(b), 1(c), and 1(d) were used to obtain both heat-transfer and pressure data. These models were constructed by bonding 0.0762-cm-thick inconel plates to fiber-glass shells having several internal ribs. The shell ribs not only provided strength and rigidity for the shells but also limited plate deflections due to aerodynamic loads and provided additional surface area to which the plates were bonded. The use of fiber glass as a shell and rib material maintained a low rate of conduction from the plate to the supporting structure.

The plates of models 1 and 2 were instrumented over half their surface with static-pressure orifices and over the other half with iron-constantan thermocouples spotwelded to the undersurface. The location of the instrumentation is shown in figures 1(a) and 1(c),

and a complete list of ordinates is presented in table I. The longitudinal thermocouple rows are located midway between shell ribs to minimize the possibility of conduction errors.

Model 3 was formed from 1.3-cm-thick mild steel plate as shown in figure 2. This model was used to obtain oil-flow photographs and a more detailed pressure distribution. Figure 2(a) shows the location of the static-pressure orifices on model 3.

The leading-edge bluntness was varied by attaching strips of fiber glass to the undersurface of the wings as shown in figure 3. None of these strips contained any instrumentation.

For the schlierens and the pressure and heat-transfer tests, the models were installed in the test section as shown in figure 4, with the instrumented surface downward.

To insure that the boundary layer was fully turbulent over a large portion of the wings, an artificial trip was used on all configurations. This trip consisted of large sand particles (≈ 0.10-cm diameter) which were spaced 0.635 cm apart on lines parallel to and 0.635 cm behind the leading edges. These trips may be seen in the photographs of figures 1(b), 1(d), 2(b), and 4.

The following table presents the geometric characteristics of the eight configurations used in this investigation:

Configuration	Model	Λ, deg	r, cm
1	1	60	≈ 0
2	1	60	.317
3	1	60	.635
4	2	70	≈ 0
5	2	70	.317
6	2	70	.635
7	3	70	≈ 0
8	3	70	.635

Total-pressure distributions in the flow field of configuration 7 were obtained by using the probe head and traversing mechanism shown in figure 5. The probe head (fig. 5(a)) contains two pitot-type probes 1 cm apart and 0.0508 cm thick. The traversing mechanism (fig. 5(b)) consists of a gear-driven threaded rod capable of positioning the probe head with an accuracy of better than 0.00254 cm. Whereas the traversing mechanism positioned the probes perpendicular to the wing surface, spanwise and chordwise positioning was accomplished by using an offset sting and rotating a plug in the test-section door and by using a movable model support strut, respectively. Note that it was necessary to roll the model 90° to obtain these surveys.

4

The pressure orifices of all models and the pitot probes were connected with 0.1778-cm-outside-diameter inconel tubing to electrical pressure transducers outside the tunnel. The output of each transducer was recorded on a digital self-balancing potentiometer. The output of each thermocouple was recorded on a multichannel sequential analog-digital converter discussed in reference 17. The tunnel free-stream static and stagnation pressures were measured on precision mercury manometers. Stagnation temperature within the test section was measured by probes mounted on a rod attached to the sting and located just aft of, but outside the boundary layer on, the model.

APPARATUS AND TEST CONDITIONS

This investigation was conducted in the high Mach number test section of the Langley Unitary Plan wind tunnel described in reference 18. This variable-pressure, continuous-flow tunnel has an asymmetric sliding-block nozzle that permits a continuous variation in the test-section Mach number from 2.30 to 4.63. The deviation in Mach number in the entire 1.22- by 1.22-meter test section for $M = 2.98$ is ±0.015 and for $M = 3.71$ and 4.44 is ±0.050. The effects of nonuniform Mach number were minimized by using a knuckle and sting that pivoted the model about a point near the center line of the tunnel as the angle of attack was changed. In general, the value of T_w/T_e was between 0.85 and 0.90 at the time the heat-transfer data were evaluated. Heat-transfer and pressure measurements were obtained for the following test conditions:

M	R per meter	T_t, $^{\circ}$K	α, deg
2.98	9.85×10^6 and 19.7×10^6	397	0 ±5 ±10
3.71	9.85×10^6 and 19.7×10^6	397	0 ±5 ±10
4.44	9.85×10^6 and 19.7×10^6	380	0 ±5

METHOD OF HEAT-TRANSFER DATA REDUCTION

The heat-transfer coefficients were obtained from transient skin-temperature measurements resulting from a stepwise increase in stagnation temperature. This technique is described in detail in reference 17.

The following relation, which assumes constant temperature through the skin, negligible lateral heat flow, negligible heat flow to the model interior, and no heat losses due to radiation, was used:

$$h = \frac{Wc \dfrac{dT_w}{dt}}{T_e - T_w}$$

This equation can be integrated and written in the following form for complete machine calculation:

$$h = \frac{Wc\left(T_{w,n} - T_{w,0}\right)}{\dfrac{T_e}{T_t} \displaystyle\int T_t \, dt - \int T_w \, dt}$$

The integrals are evaluated over increments of 0.5 second, according to the trapezoidal rule, which yields

$$\int T \, dt = \Delta t\left(\frac{1}{2} T_0 + \frac{1}{2} T_n + T_1 + T_2 \dots + T_{n-1}\right)$$

and the ratio T_e/T_t is experimentally determined.

The magnitude of the lateral heat flow was evaluated at several locations and was found to be negligible. The heat flow by radiation was also evaluated and found to be negligible.

ACCURACY

The accuracy of the temperature measurements, including recorder resolution, thermocouple-wire calibration, and cold-junction temperature, is $\pm 1.0^\circ$ K; however, this error occurs in temperature level rather than in random temperature fluctuations. A temperature error of $\pm 1.0^\circ$ K could result in ratios of wall equilibrium temperature to stagnation temperature T_e/T_t greater than 1 in stagnation regions of the model. Also, as mentioned in reference 19, in regions of low heat transfer $(h < 20 \text{ J/m}^2\text{-sec-}^\circ\text{K})$ the ratio T_e/T_t may be questionable because the wall temperature may not have reached equilibrium from the preceding test point.

An estimation of the accuracy of heat-transfer measurements in the Langley Unitary Plan wind tunnel has been determined by the repeatability of data in the tests discussed in reference 19. The accuracy is dependent on the magnitude of the heat-transfer coefficient. For $h > 306 \text{ J/m}^2\text{-sec-}^\circ\text{K}$, the accuracy is within 10 percent; for $20 \text{ J/m}^2\text{-sec-}^\circ\text{K} < h < 306 \text{ J/m}^2\text{-sec-}^\circ\text{K}$, within 15 percent; and for $h < 20 \text{ J/m}^2\text{-sec-}^\circ\text{K}$, within 20 percent. Although $h < 20 \text{ J/m}^2\text{-sec-}^\circ\text{K}$ is within the accuracy of data reduction, no significance is attached to the magnitude of h, other than to indicate the regions of low heat transfer.

The accuracy of the precision manometers is within 23.94 N/m^2. Therefore, the accuracy of the pressures is limited to that of the 34 474 N/m^2 electrical transducer, which is 0.5 percent of the full-scale deflection.

RESULTS AND DISCUSSION

Schlierens

Schlieren photographs of configurations 7 and 8 (70° sweep) at Mach numbers of 2.98, 3.71, and 4.44, a free-stream Reynolds number per meter of 9.85 × 10^6, and angles of attack from -10° to 10° are presented in figures 6 and 7, respectively.

The visible shocks on the instrumented surface (lower surface) were caused by the large sand particles (≈0.10-cm diameter) used to trip the boundary layer. It is believed that these shocks had no appreciable effect on either the heat-transfer or pressure data since the boundary layer undergoes transition to turbulent flow a short distance aft of the particles.

Flow Visualization

Oil-flow photographs of configuration 7 are presented in figure 8 for Mach numbers of 2.98 and 3.71 at angles of attack of 0° and ±5°. At $\alpha = 0^O$ (fig. 8(a)) for both Mach numbers the oil streaks on the model are essentially parallel to the wing center line and thus indicate very little if any spanwise flow. Similar results are shown on the windward surface at $\alpha = 5^O$ in figure 8(b). The oil-flow patterns occurring on the wing surface at $\alpha = -5^O$ (surface leeward) are radically different from the aforementioned patterns. Such a difference in the flow pattern is expected; however, as a result of the formation of coiled vortex sheets over the leeward surface. These vortex formations have previously been observed by experimenters (refs. 20 and 21) on delta wings at angles of attack where the product of β and A is small. At M = 2.98 and $\alpha = -5^O$ the direction of the oil streaks shown on the oil-flow photograph (fig. 8(c)) are in good agreement with the flow model presented in reference 21. For these test conditions the leading edges are near sonic, that is, the component of Mach number normal to the leading edge is approximately unity; this condition resulted in the coiled vortex sheet forming along the leading edge and reattaching on the leeward surface. Since the vortex formation is symmetrical about the wing center line, the spanwise velocity components on each side of the center line are equal in magnitude and opposite in direction. The resulting flow direction inboard of the attachment line is therefore parallel to the center line as indicated in the sketch. The flow outboard of the attachment line has a spanwise velocity component toward the wing leading edge. A second flow-separation region occurs as this spanwise flow approaches

the leading edge. The vortex attachment line and the secondary separation line as defined in the sketch are clearly visible in the oil-flow photographs.

At $M = 3.71$ and $\alpha = -5°$ the wing leading edges are supersonic and a different flow pattern exists over the leeward surface as shown in figure 8(d). The flow regions defined in the sketch are again clearly visible in the oil-flow photographs. The flow remains attached in the leading-edge region after passing through a supersonic expansion at the leading edge. The flow is then separated, however, after passing through the oblique shock wave originating from the wing apex. The resulting vortex attachment flow pattern confined inboard of the oblique shock formation is similar to that obtained on the leeward surface when the leading edge was subsonic.

Velocity Profiles

In order to insure that effective tripping of the boundary layer occurred, velocity profiles were determined from total-pressure surveys at several locations on configuration 7 and are presented in figure 9. The total temperature was assumed to remain constant through the boundary layer. Also shown in the figure is a curve having a slope corresponding to a 1/6-power velocity profile (which is indicative of turbulent flow) for comparison with the experimental data. For $\alpha = 0°$ (fig. 9(a)) the slopes of the velocity profiles are in good agreement with the slope of the 1/6-power profile for all survey stations and indicate that, at least as far upstream as the surveys were made, a fully developed turbulent boundary layer existed over the wing.

Velocity profiles for some of these same stations are presented in figure 9(b) for $\alpha = 5°$ (survey surface windward). The velocity profiles are again in fair agreement with the 1/6-power profile and there is no discernible change in the boundary-layer thickness compared to the profiles obtained at $\alpha = 0°$.

For an angle of attack of $-5°$ (survey surface leeward) the velocity profiles which are shown in figure 9(c) deviate from the power profiles. This deviation was expected, however, because of the vortex formation over the leeward surface as shown in the oil-flow photographs. A detailed discussion of these leeward data is considered unwarranted for two reasons: (1) the distributions are not of sufficient detail to provide conclusive information pertaining to vortex flow and (2) the large components of spanwise flow at some survey locations indicated in the oil-flow photographs could result in inaccurate total-pressure measurements since the pressure probe was always alined with the model center line.

Surface Pressure Distributions

Presented in figure 10(a) are the pressures obtained on configuration 1 for $M = 2.98$, $R = 9.85 \times 10^6$, and angles of attack of $0°$ and $\pm 10°$. At $\alpha = 0°$, the pressure

magnitudes are approximately constant and equal to the free-stream static pressure over the entire instrumented surface. Increasing the angle of attack to 10° (instrumentation windward) resulted in an increase in the magnitude of the pressures, the magnitude of the increase decreasing with increasing s. The resulting favorable pressure gradient consists of large pressure variations with s in the leading-edge region of the model and relatively small pressure variation toward the base of the model. The pressure magnitudes vary from a maximum value approximately 50 percent greater than the value from two-dimensional theory in the leading-edge region to a minimum value that falls between the two-dimensional and conical theoretical values (based on a cone semiapex angle equal to α) in the base region.

Decreasing the angle of attack to -10° resulted in a decrease in the pressures over the entire wing surface. The maximum decrease occurred in the vicinity of the wing leading edge, with the magnitude of the decrease decreasing with increasing s. The magnitude of the pressures on the aft portion of the wing are in fair agreement with the Prandtl-Meyer expansion theory. A slight favorable spanwise pressure gradient exists on the wing leeward surface and is believed to be associated with a vortex formation similar to that shown in the oil-flow photographs of the 70° swept wing. However, much larger variations in the pressures were obtained on the leeward surface of the 70° swept wing as will be discussed subsequently.

The shape of the pressure distributions throughout the test range of Mach and Reynolds numbers for the 60° swept wing having a sharp leading edge are very similar to those obtained at $M = 2.98$ and $R = 9.85 \times 10^6$ as can be seen by comparing figure 10(a) with figures 10(b) to 10(f). In general, throughout this test range of variables, the pressures on the aft portion of the windward wing surface approach a value that falls between the two-dimensional and conical theoretical values whereas the pressures on the leeward surface approach values approximately equal to those occurring across a Prandtl-Meyer expansion.

Pressure distributions obtained on a 70° swept wing (configuration 4) are presented in figure 11(a) for $M = 2.98$ and $R = 9.85 \times 10^6$. The results shown for $\alpha = 0^O$ and $\alpha = 5^O$ are very similar to the pressures obtained for the 60° swept wing presented in figure 10. The pressures obtained on the leeward surface are also quantitatively similar to the data obtained on the 60° swept wing; however, the spanwise pressure gradients for the 70° wing are considerably larger. The flow field associated with the pressure distributions for the leeward side of the 70° wing can be visualized by examining the oil-flow photographs presented in figure 8. The relatively high pressures occurring on the model center line are located within the parallel-flow region inboard of the vortex attachment line. The lower pressures obtained at $y = 0.152$ and 0.229 m are located outboard of the vortex attachment line. The pressures obtained at $y = 0.076$ m (square symbols)

increase from the low values on the forward portion of the chord where spanwise flow effects are present to the higher values on the aft portion of the wing where the flow is chordwise. Such an increase in pressure at this span was expected because of the intercept of the vortex attachment line with this span station as indicated in the oil-flow photograph. The magnitudes of the pressures within the parallel-flow region are seen to be in good agreement with the value represented by the Prandtl-Meyer expansion.

Pressure distributions obtained on the 70° swept wing at $M = 2.98$ and $R = 19.7 \times 10^6$ are presented in figure 11(b). At $\alpha = 0^O$ the leading-edge pressures near the wing tip are less than those obtained near the wing center line. This pressure drop is believed to be due to the model being at a slight angle of attack resulting from a combination of flow angularity and model deflection. In general, the pressure distributions obtained at all three angles of attack are approximately the same as those obtained at the lower Reynolds number. For $\alpha = -5^O$ the increase in pressure along the chord at $y = 0.076$ m is more pronounced than that obtained at the lower Reynolds number and occurs at a greater value of s, indicating that the vortex is larger and covers most of the wing surface.

Pressure distributions obtained on the 70° wing at a Mach number of 3.71 are presented in figure 11(c) for a range of angle of attack from -10° to 10°. With the exception of $\alpha = -10^O$, the trends of the variation of the pressure distributions with angle of attack are consistent with those noted at $M = 2.98$. At $\alpha = -10^O$, the vortex attachment line on the leeward surface is apparently confined to within the spanwise station $y = 0.076$ m as no increase in pressure is noted at this span, an indication that the vortex covers almost the entire wing surface. There was no significant effect on the pressure distribution as a result of increasing the Reynolds number from 9.85×10^6 to 19.7×10^6 as can be seen by comparing figures 11(c) and 11(d).

Pressure distributions obtained on the 70° swept wing at $M = 4.44$ for the angle-of-attack range, as shown in figures 11(e) and 11(f), are approximately the same as those previously discussed for the lower Mach numbers.

A summary of the Mach number effect on the pressure distributions of the 60° and 70° swept wing is presented in figures 12 and 13, respectively, for $\alpha = 0^O$. For both wings the variation of p_l/p_∞ with Mach number through the test range of Mach number is within the data accuracy.

The pressure distributions for the 60° and 70° swept wings are presented in figures 14 and 15, respectively, for leading edges varying from a sharp leading edge to a 0.635-cm-radius cylindrical leading edge. There was no effect of leading-edge bluntness on the pressure distributions through the range of variables of the investigation.

All the pressure data presented in figures 10 to 15 were obtained simultaneously with the heat-transfer data and, therefore, at a time when large thermal gradients existed throughout the model. In order to determine whether these thermal gradients, combined with the aerodynamic loading on the model, resulted in deformations large enough to affect the pressure measurements, model 3 was instrumented with pressure orifices and tested at approximately the same test conditions with the model at thermal equilibrium. The results from this model were, within data accuracy, the same as those obtained for configurations 4 and 6. Consequently, these data are not presented. Since the data from both models were in excellent agreement, the deformations caused by thermal gradients in the model had no effect on the pressure distributions.

Heat Transfer

Heat-transfer coefficient distributions obtained with configurations 1 and 4 through the range of variables of the investigation are presented in figures 16 and 17. Also presented in these figures, for comparison with the experimental data at $y = 0.076$ m, are theoretical estimates obtained by using the theory of reference 22, based on local conditions at this station. These local conditions consisted of (1) measured static pressures, (2) measured local wall temperatures, (3) a local total pressure corresponding to free-stream total pressure for $\alpha \leq 0^{\circ}$ and corresponding to that on a two-dimensional wedge having an included angle equal to the angle of attack for $\alpha > 0^{\circ}$, and (4) a local Reynolds number R_l based on s the longitudinal surface length behind the wing leading edge.

The heat-transfer coefficient distributions obtained on configuration 1 for $M = 2.98$ and $R = 9.85 \times 10^6$ are presented in figure 16(a) for angles of attack of 0° and $\pm 10^{\circ}$. For $\alpha = 0^{\circ}$ the data indicate that the boundary layer is fully turbulent at all instrumented stations for $s \geq 0.08$ m and both the magnitude and distribution of the measured heating rates downstream of this station are in fair agreement with theory. As shown in the figure, good correlation of the experimental data at all instrumented stations is obtained by plotting the heat-transfer coefficients as a function of the longitudinal surface length from the wing leading edge. This correlation was expected, however, because of the negligible spanwise flow for these conditions as indicated previously both by oil-flow photographs and pressure distributions. The magnitudes of the measured heating rates are approximately 10 percent less than the theoretical results, a difference which is within the accuracy of the experimental data.

Increasing the angle of attack to 10° resulted in a general increase in the magnitude of the heating rates with no apparent change in the locations at which the flow becomes fully turbulent. The magnitudes of these measured heating rates are again approximately 10 percent below the theoretical values and remain approximately constant for constant s at all instrumented stations.

Decreasing the angle of attack to -10° resulted in a decrease in the magnitude of the heating rates with the smallest decrease occurring along the wing center line. For a constant value of s the magnitudes of the heating rates for all stations outboard of the center line are approximately constant and are about 40 percent less than the center-line values. This spanwise heating gradient is believed to result from a vortex formation over the leeward surface similar to that indicated by the oil-flow photographs for the 70° swept wing. The magnitudes of the heating rates for $y \geq 0.076$ m are in fair agreement with the theoretical results; however, if the flow field over the leeward surface is as hypothesized, this agreement is fortuitous unless the wing leading edges are supersonic. The effect of increasing Reynolds number on the heating distributions for a given Mach number may be seen by comparing figures 16(a) and 16(b) or 16(c) and 16(d) or 16(e) and 16(f). This effect consists primarily of an increase in the magnitude of the heating rates with little change in the heating distributions or agreement with theory. By comparing figures 16(a), 16(c), and 16(e) or 16(b), 16(d), and 16(f), the effect of Mach number on the heating distributions at a given Reynolds number can be determined. The effect on the magnitude of h of increasing Mach number shows a trend opposite to that for the increase in Reynolds number; that is, the heating rate decreases.

Heating distributions obtained for configuration 4 at $M = 2.98$ and $R = 9.85 \times 10^6$ for angles of attack of 0° and $\pm 5^O$ are presented in figure 17(a). For $\alpha = 0^O$ the boundary layer becomes fully turbulent at $s \approx 0.13$ m, and for greater values of s the experimental heating rates are in good agreement with theory. Increasing angle of attack to 5° resulted in the anticipated increase in the magnitude of the heating rates with no apparent change in the location of the point at which the boundary layer becomes fully turbulent. For $\alpha = 0^O$ and 5° the magnitudes of the heating rates along any line parallel to the wing leading edge are constant, which is similar to the distributions shown for the 60° swept wing. The heating distributions obtained for $\alpha = -5^O$ (leeward surface) contain large heating gradients in both the chordwise and spanwise directions. These gradients are to be expected as a result of the vortex impingement on the leeward surface as shown by the oil-flow photographs and pressure distributions. In general, the longitudinal heating distributions are roughly the same as the pressure distributions presented in figure 11(a); however, the spanwise gradients are considerably different. The maximum heating rates on the leeward surface occurred at $y = 0.076$ m in the region of the vortex attachment line. The maximum heating rates in this region were even greater than the values obtained at $\alpha = 0^O$.

The effect of increasing Reynolds number on the heating distributions obtained on configuration 4 at $M = 2.98$ can be seen by comparing figures 17(a) and 17(b). For angles of attack of 0° and 5° the Reynolds number effect consists of the expected increase in heating. For $\alpha = -5^O$ the greatest increase in heating with increasing Reynolds

number was obtained in the region near and inboard of the vortex stagnation line. The heating rates obtained in the vicinity of the vortex stagnation line were again greater than those obtained at the same station for $\alpha = 0^\circ$.

Heating distributions obtained on configuration 4 at $M = 3.71$ and $R = 9.85 \times 10^6$ are presented in figure 17(c). At zero and positive angles of attack the magnitude and distribution of heating rates are in good agreement with theory. The large longitudinal and spanwise heating gradients that occurred on the leeward surface at $M = 2.98$ do not occur on the leeward surface at $M = 3.71$. This difference is apparently due to the wing leading edges being supersonic, as indicated by the oil-flow photographs. Similar results are shown through the remaining range of Mach numbers and Reynolds numbers in figures 17(d) to 17(f).

The effect of Mach number on the heating distributions for configurations 1 and 4 at zero angle of attack is summarized in figures 18 and 19, respectively. The values presented in these figures were obtained at $y = 0.076$ m; however, they are representative of the distributions obtained over the complete surface. In general, throughout the test Mach number range, both the magnitude and distribution of the heating rates are in good agreement with theory.

Presented in figure 20 are heating distributions obtained on the 60° swept wing for a range of leading-edge bluntness varying from the sharp leading edge to a 0.635-cm-radius cylindrical leading edge. The effect of varying the leading-edge bluntness through the range of variables of the investigation is negligible downstream of the region where the boundary layer is fully turbulent. Similar results are shown for the 70° swept wing in figure 21.

CONCLUSIONS

Heat-transfer and pressure measurements were obtained in an artificially tripped boundary layer on 60° and 70° swept delta wings at Mach numbers of 2.98, 3.71, and 4.44 and nominal Reynolds numbers per meter of 9.85×10^6 and 19.7×10^6. Results obtained lead to the following conclusions:

(1) Oil-flow photographs of a 70° swept delta wing with sharp leading edges at negative angles of attack indicated the presence of a vortex sheet formation over the leeward surface. Heat-transfer and pressure measurements obtained under these conditions revealed large gradients in both heating and pressure.

(2) For angles of attack from 0° to 10° (instrumentation windward) both the magnitude and distribution of heat-transfer measurements throughout the range of test conditions were generally in good agreement with turbulent flat-plate theory based on local

conditions. The measured heating rates through this range of angle of attack remained approximately constant along any line parallel to the wing leading edge.

(3) There was no noticeable effect throughout the range of test conditions on either the heat-transfer or pressure measurements as a result of increasing the wing leading-edge bluntness from a sharp leading edge to a cylindrical leading edge of 0.635-centimeter radius.

Langley Research Center,
    National Aeronautics and Space Administration,
        Langley Station, Hampton, Va., May 19, 1966,
            126-13-02-10-23.

REFERENCES

1. Speegle, Katherine C.: Heat-Transfer Measurements of Two Wing-Body Combinations at 8° Angle of Attack From a Flight Test for Mach Numbers to 4.86 and Reynolds Numbers to 19.2×10^6. NASA MEMO 10-25-58L, 1958.

2. Carter, Howard S.: Heat Transfer on the Lifting Surfaces of a 60° Delta Wing at Angle of Attack for Mach Number 1.98. NACA RM L56C23, 1956.

3. Bertram, Mitchel H.; and Henderson, Arthur, Jr.: Recent Hypersonic Studies of Wings and Bodies. ARS J., vol. 31, no. 8, Aug. 1961, pp. 1129-1139.

4. Dunavant, James C.: Heat Transfer to a Delta-Wing—Half-Cone Combination at Mach Numbers of 7 and 10. NASA TN D-2199, 1964.

5. O'Neal, Robert L.; and Bond, Aleck C.: Heat Transfer to 0° and 75° Swept Blunt Leading Edges in Free Flight at Mach Numbers From 1.90 to 3.07. NASA TN D-1256, 1962.

6. Stainback, P. Calvin: Heat-Transfer Measurements at a Mach Number of 4.95 on Two 60° Swept Delta Wings With Blunt Leading Edges and Dihedral Angles of 0° and 45°. NASA TN D-549, 1961.

7. Bond, Aleck C.; Feller, William V.; and Bland, William M., Jr.: Aerodynamic Heat Transfer to Wing Surfaces and Wing Leading Edges. NACA RM L57D22c, 1957.

8. Bertram, Mitchel H.; and Everhart, Philip E.: An Experimental Study of the Pressure and Heat-Transfer Distribution on a 70° Sweep Slab Delta Wing in Hypersonic Flow. NASA TR R-153, 1963.

9. Archer, R. D.; Melnik, W. L.; and Hermann, R.: Experimental Pressure and Heat Transfer Distributions on Blunt-Nose Delta Wings for Angles of Attack up to 30° at Mach Number 7. ARL 63-231, U.S. Air Force, Dec. 1963.

10. Stallings, Robert L., Jr.; Burbank, Paige B.; and Howell, Dorothy T.: Heat-Transfer and Pressure Measurements on Delta Wings at Mach Numbers of 3.51 and 4.65 and Angles of Attack From -45° to 45°. NASA TN D-2387, 1964.

11. Ceresuela, R.; Marguet, R.; and Vaucheret, X. (J. B. W. Edwards, trans.): Kinetic Heating on a Representative Model of a Supersonic Transport Aircraft. Libr. Transl. No. 1076, Brit. R.A.E., Aug. 1964.

12. Hiers, R. S.; Hillsamer, M. E.; and Morris, S. D.: Heat Transfer and Pressure Distribution Tests of Several Flat Plate and Delta Wing Shapes. AEDC-TN-61-40, U.S. Air Force, Apr. 1961.

13. Dunavant, James C.: Investigation of Heat Transfer and Pressures on Highly Swept Flat and Dihedraled Delta Wings at Mach Numbers of 6.8 and 9.6 and Angles of Attack to 90°. NASA TM X-688, 1962.

14. Royall, John F., Jr.; and Newcomb, John F.: Investigation of Heat Transfer on a Simulated 82° Swept Delta Wing in Free Flight at Angle of Attack at Mach Numbers up to 9.8. NASA TM X-622, 1962.

15. Jones, Robert A.; and Gallagher, James J.: Heat-Transfer and Pressure Distributions of a 60° Swept Delta Wing With Dihedral at a Mach Number of 6 and Angles of Attack From 0° to 52°. NASA TM X-544, 1961.

16. Jones, Robert A.; and Trimpi, Robert L.: Heat-Transfer and Pressure Distributions at a Mach Number of 6 for 70° Swept Slab Wings With Sharp and Spherical Noses and Cylindrical Leading Edges. NASA TM X-682, 1962.

17. Burbank, Paige B.; and Hodge, B. Leon: Distribution of Heat Transfer on a 10° Cone at Angles of Attack From 0° to 15° for Mach Numbers of 2.49 to 4.65 and a Solution to the Heat-Transfer Equation That Permits Complete Machine Calculations. NASA MEMO 6-4-59L, 1959.

18. Anon.: Manual for Users of the Unitary Plan Wind Tunnel Facilities of the National Advisory Committee for Aeronautics. NACA, 1956.

19. Taylor, Nancy L.; Hodge, Ward F.; and Burbank, Paige B.: Heat-Transfer and Pressure Measurements of a 1/7-Scale Model of a Mercury Capsule at Angles of Attack From 0° to ±20° at Mach Numbers of 3.50 and 4.44. NASA TM X-522, 1961.

20. Brown, C. E.; and Michael, W. H., Jr.: Effect of Leading-Edge Separation on the Lift of a Delta Wing. J. Aeron. Sci., vol. 21, no. 10, Oct. 1954, pp. 690-694, 706.

21. Stanbrook, A.; and Squire, L. C.: Possible Types of Flow at Swept Leading Edges. Aeron. Quart., vol. XV, pt. 1, Feb. 1964, pp. 72-82.

22. Van Driest, E. R.: Turbulent Boundary Layer in Compressible Fluids. J. Aeron. Sci., vol. 18, no. 3, Mar. 1951, pp. 145-160, 216.

TABLE I.- INSTRUMENTATION LOCATION

Orifice	Location on –				Thermocouple	Location on –			
	Model 1 ($\Lambda = 60°$)		Model 2 ($\Lambda = 70°$)			Model 1 ($\Lambda = 60°$)		Model 2 ($\Lambda = 70°$)	
	s, m	y, m	s, m	y, m		s, m	y, m	s, m	y, m
1	0.1334	0	0.1379	0	1	0.0572	0	0.1631	0
2	.2347		.2395		2	.0826		.1885	
3	.3363		.3411		3	.1080		.2139	
4	.4379		.4427		4	.1588		.2647	
5	.0274	0.0762	.5443		5	.1765	0.0127	.2553	0.0127
6	.0528		.6459		6	.1842	0	.2901	0
7	.0782		.7475		7	.1765	.0127	.2553	.0127
8	.1036		.0564	0.0762	8	.2096	0	.3155	0
9	.1290		.0818		9	.2604		.3663	
10	.1544		.1072		10	.2858		.3917	
11	.1798		.1326		11	.3112		.4171	
12	.2052		.1580		12	.3620	.0127	.4679	
13	.2306		.1834		13	.3708	0	.4933	
14	.2560		.2088		14	.3872		.5187	
15	.2814		.2342		15	.3708	.0127	.5695	
16	.3068		.2596		16	.4134	0	.5601	.0127
17	.3322		.2850		17	.4636		.5949	0
18	.3576		.3104		18	.4890		.5601	.0127
19	.3830		.3358		19	.5144		.6203	0
20	.0226	.1524	.3612		20	.0274	.0762	.6711	
21	.0480		.3866		21	.0528		.6965	
22	.0734		.4120		22	.0782		.7219	
23	.0988		.4374		23	.1036		.7727	
24	.1242		.4628		24	.1290		.7981	
25	.1496		.4882		25	.1544		.8235	
26	.1750		.5136		26	.1798		.0664	.0762
27	.2004		.5390		27	.2052		.0818	
28	.2258		.5644		28	.2306		.1072	
29	.2512		.5898		29	.2560		.1326	
30	.0224	.2286	.6152		30	.2814		.1580	
31	.0478		.0493	.1524	31	.3068		.1834	
32	.0732		.0747		32	.3322		.2088	
33	.0986		.1001		33	.3576		.2342	
34	.1240		.1255		34	.3830		.2596	
35			.1509		35	.0226	.1524	.2850	
36			.1763		36	.0480		.3104	
37			.2017		37	.0734		.3358	
38			.2271		38	.0988		.3612	
39			.2525		39	.1242		.3866	
40			.2779		40	.1496		.4120	
41			.3033		41	.1750		.4374	
42			.3287		42	.2004		.4628	
43			.3541		43	.2258		.4882	
44			.3795		44	.2512		.5136	
45			.4049		45	.0224	.2286	.5390	
46			.0432	.2286	46	.0478		.5644	
47			.0686		47	.0732		.5898	
48			.0940		48	.0986		.6152	
49			.1194		49	.1240		.0493	.1524
50			.1448		50			.0747	
51			.1702		51			.1000	
52			.1956		52			.1255	
					53			.1509	
					54			.1763	
					55			.2017	
					56			.2271	
					57			.2525	
					58			.2779	
					59			.3033	
					60			.3287	
					61			.3541	
					62			.3795	
					63			.4049	
					64			.0432	.2286
					65			.0686	
					66			.0940	
					67			.1194	
					68			.1448	
					69			.1702	
					70			.1956	

O Pressure orifices
◁ Thermocouples

s (typical)

60°

2.54 cm (typical)

0.527

0.889 cm

0.229

0.152

0.076

0.076

0.076

0.152

0.229

0.610

0.0762-cm inconel sheet

2.54 cm   15°

0.635 cm

Section A-A
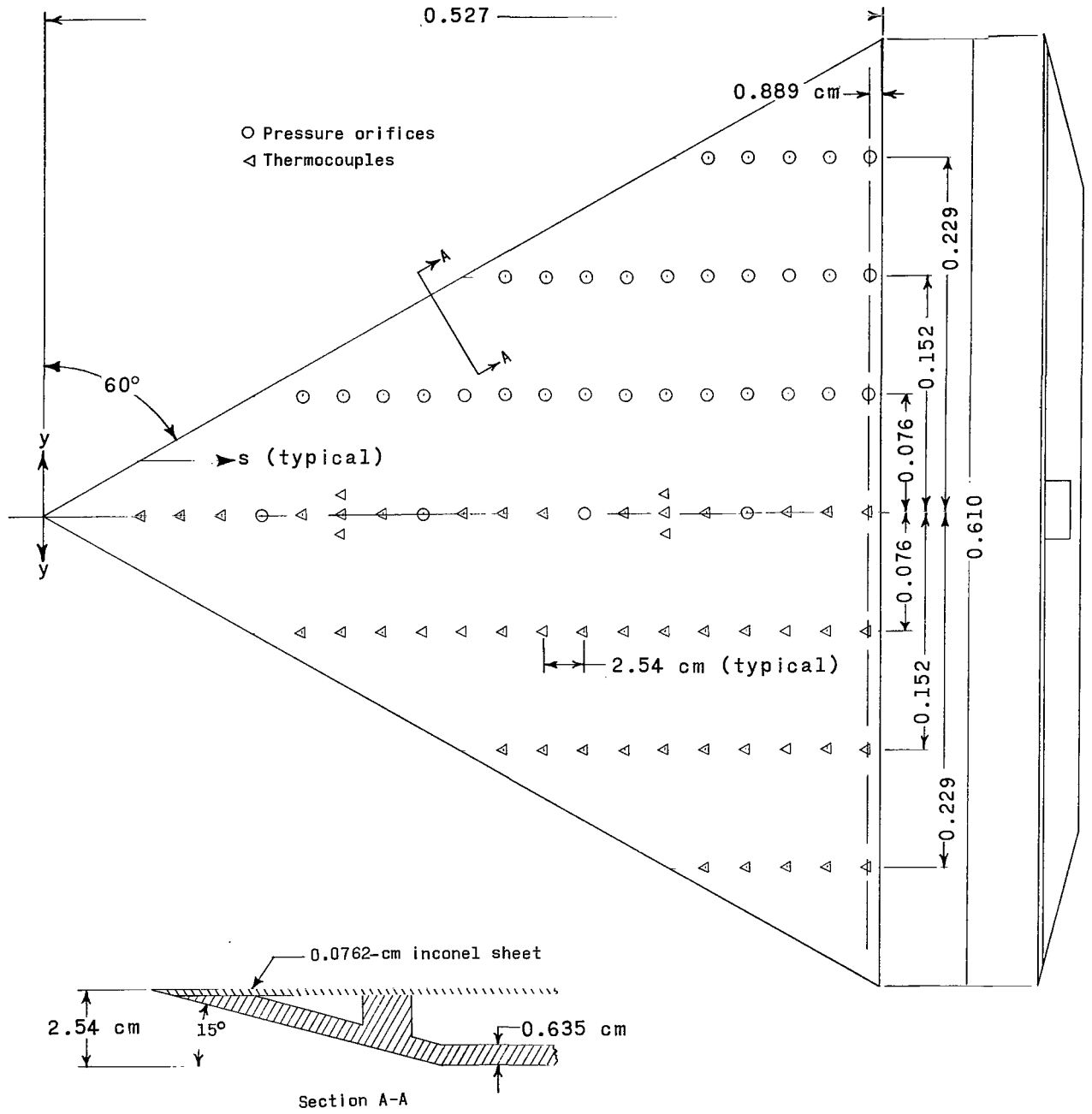
(a) Construction details of model 1.

Figure 1.- Models 1 and 2. All dimensions in meters unless otherwise noted.
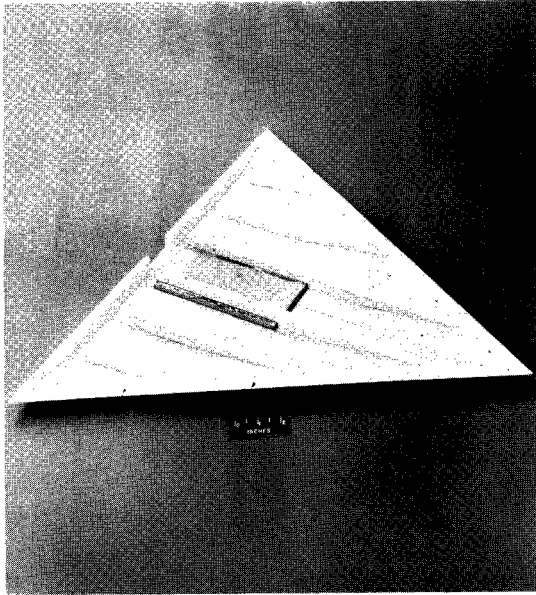
Fiber-glass shell   L-65-821   Instrumented plate   L-65-824
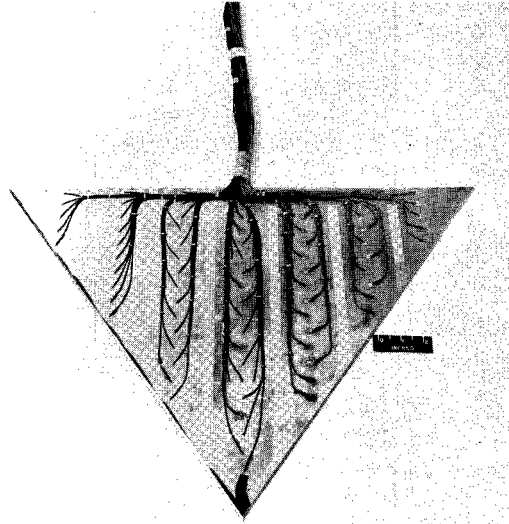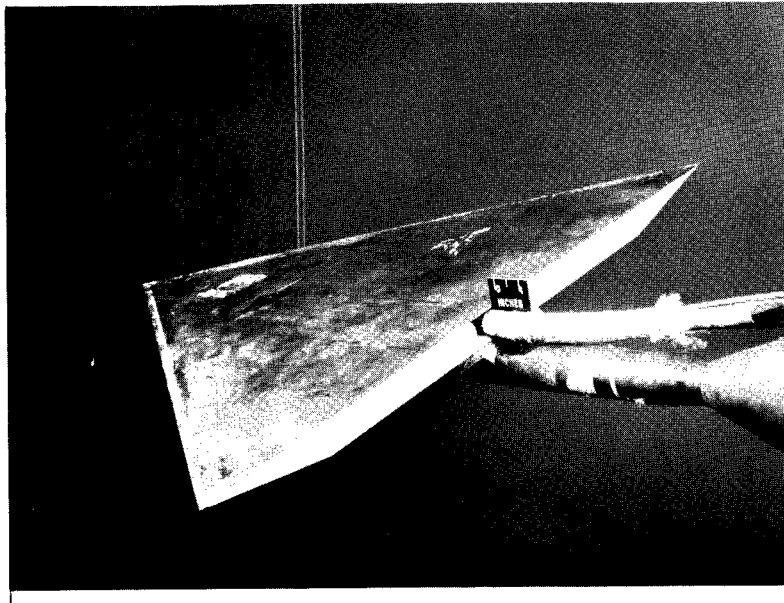
Complete model   L-65-5335

(b) Photographs of model 1.

Figure 1.- Continued.

O Pressure orifices
◁ Thermocouples
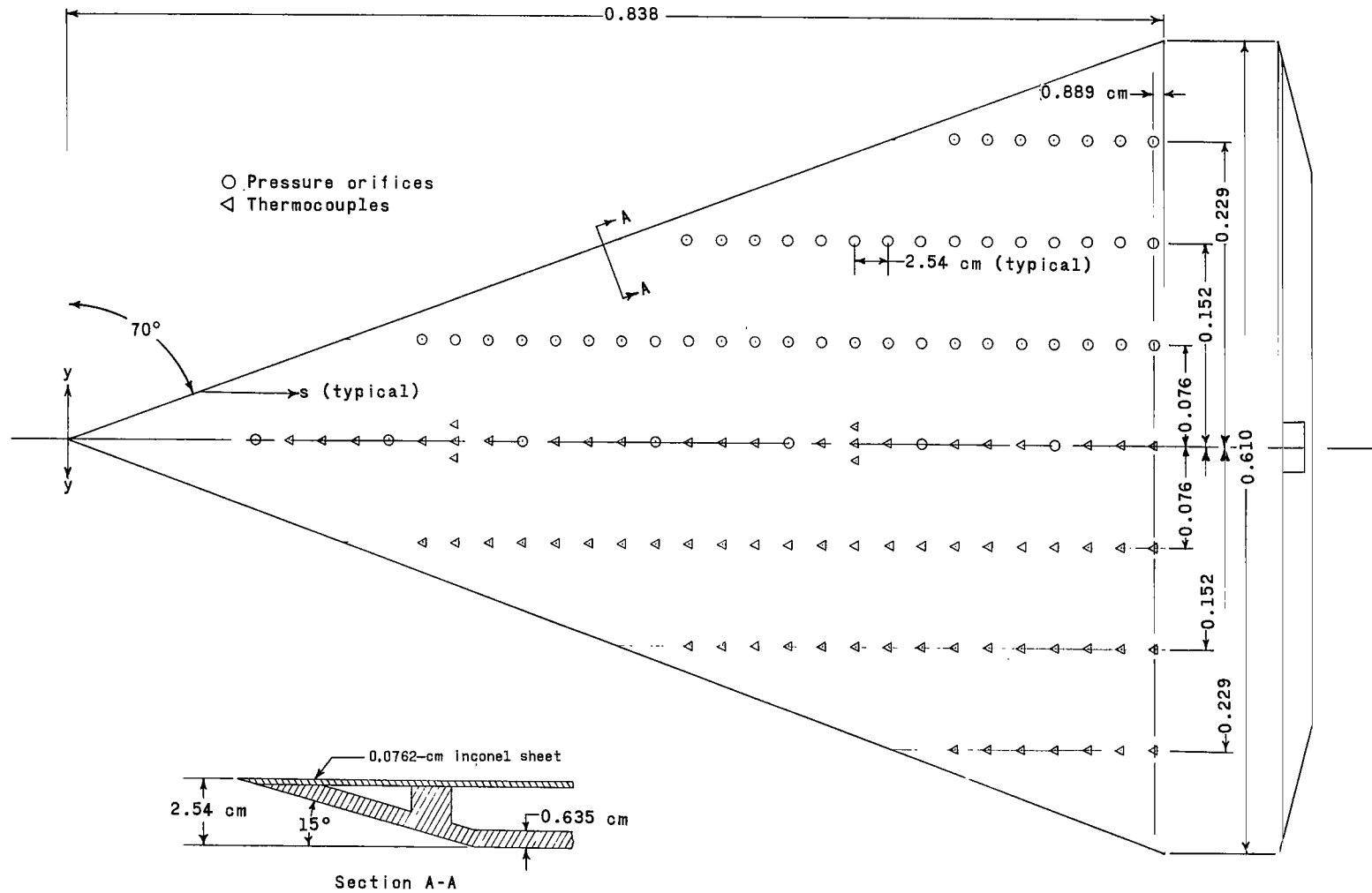
(c) Construction details of model 2.

Figure 1.- Continued.
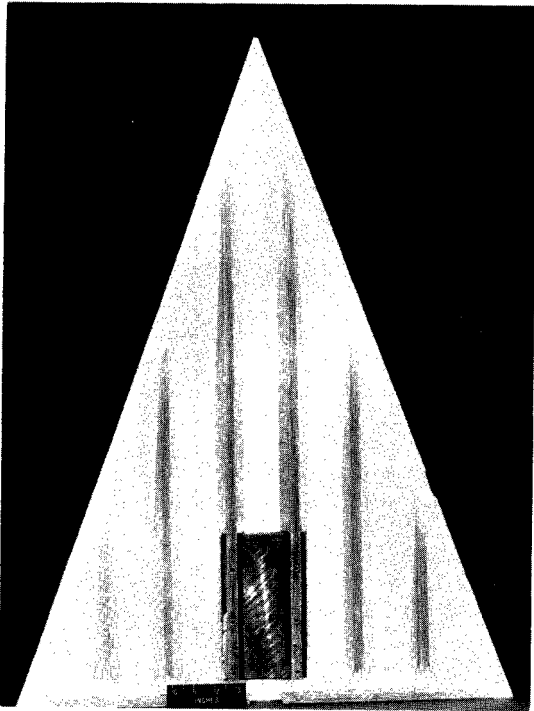
Fiber-glass shell   L-65-819   Instrumented plate   L-65-823
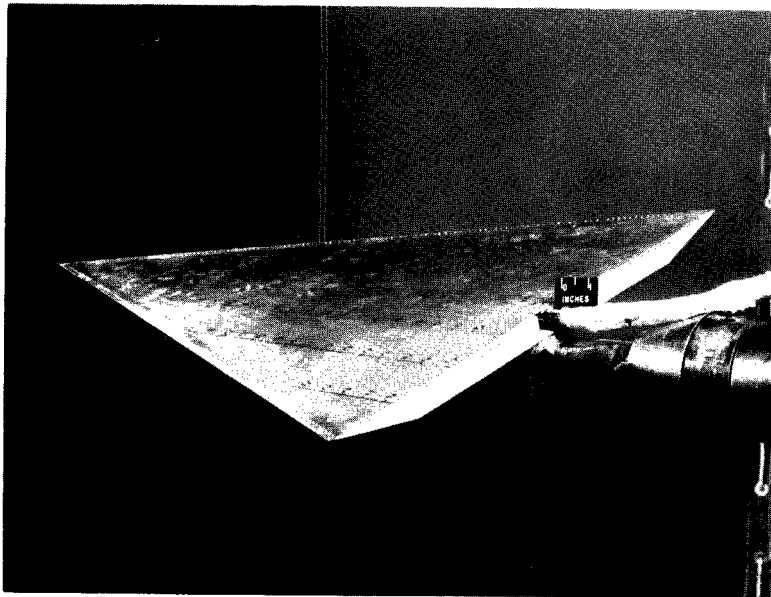
Complete model   L-65-4722

(d) Photographs of model 2.

Figure 1.- Concluded.

70°

A
A

5.08 cm — Typical

○   Pressure orifices

0.610

0.051

0.038

0.076

0.114

0.152

0.228

0.837

0.013

0.013   10°
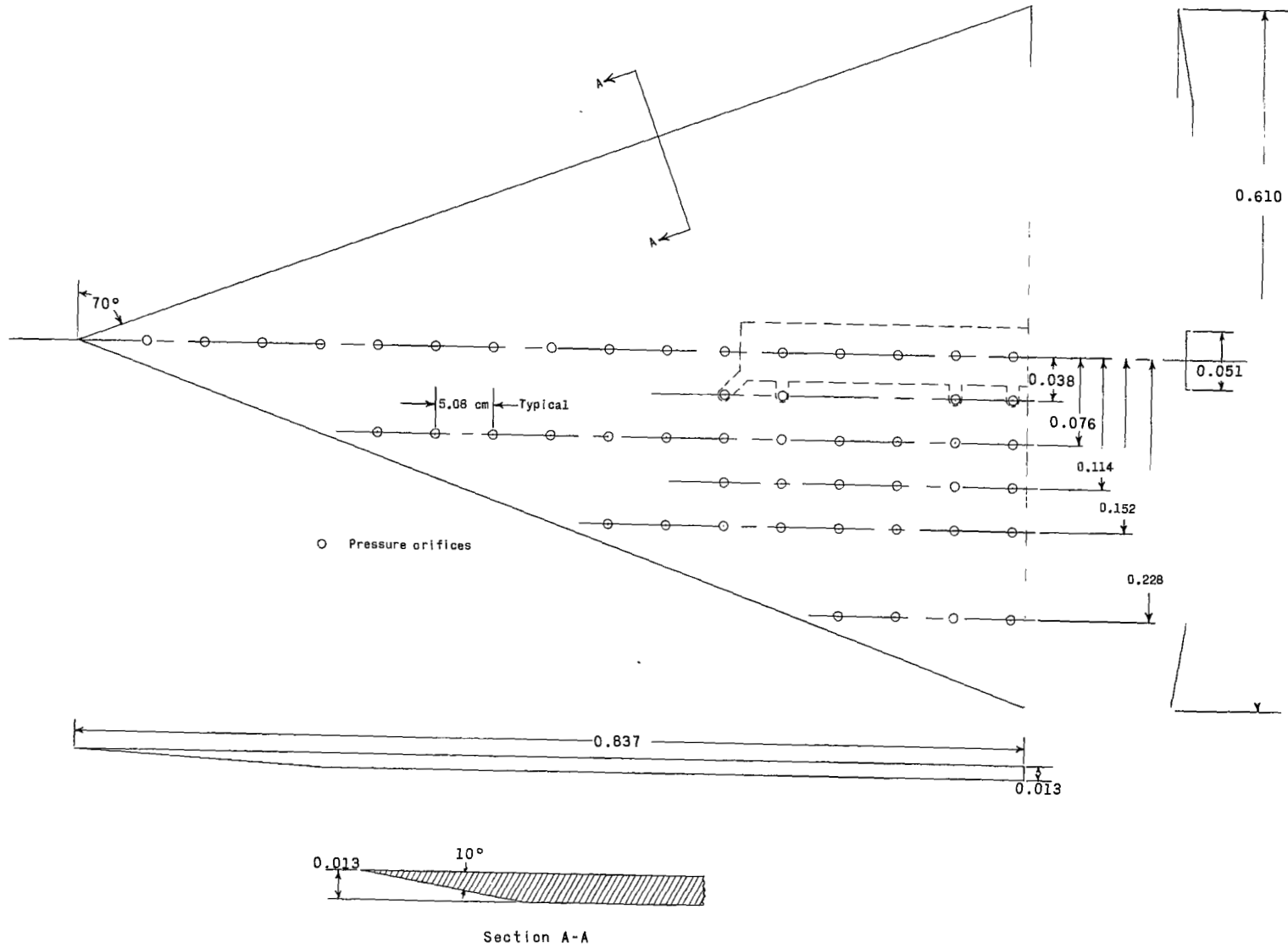
Section A-A

(a) Construction details.

Figure 2.- Model 3. All dimensions in meters unless otherwise noted.
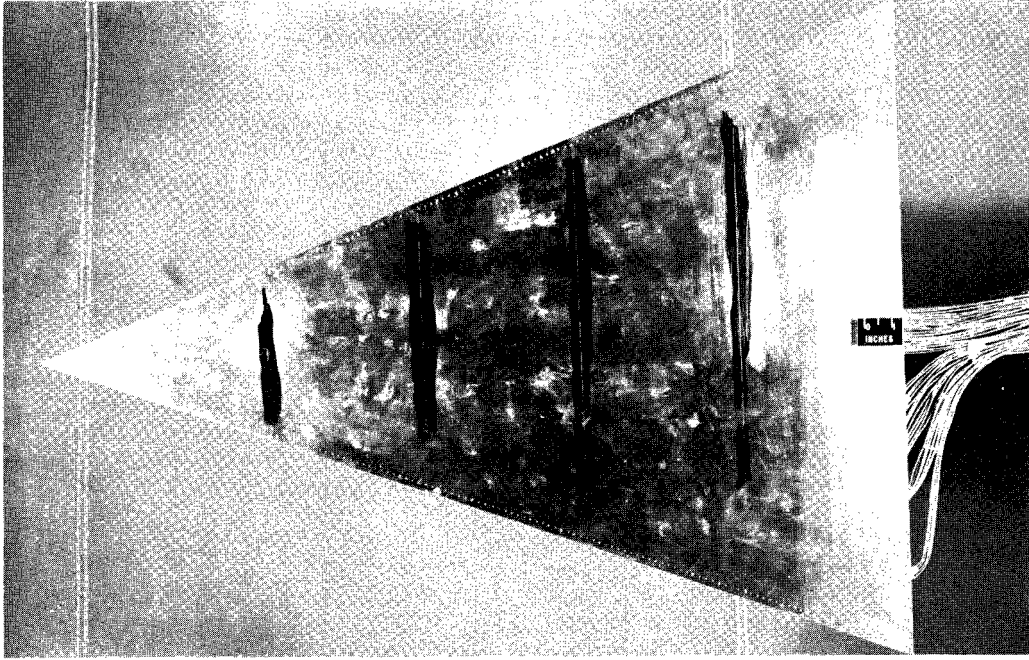
Instrumented surface   L-65-4726
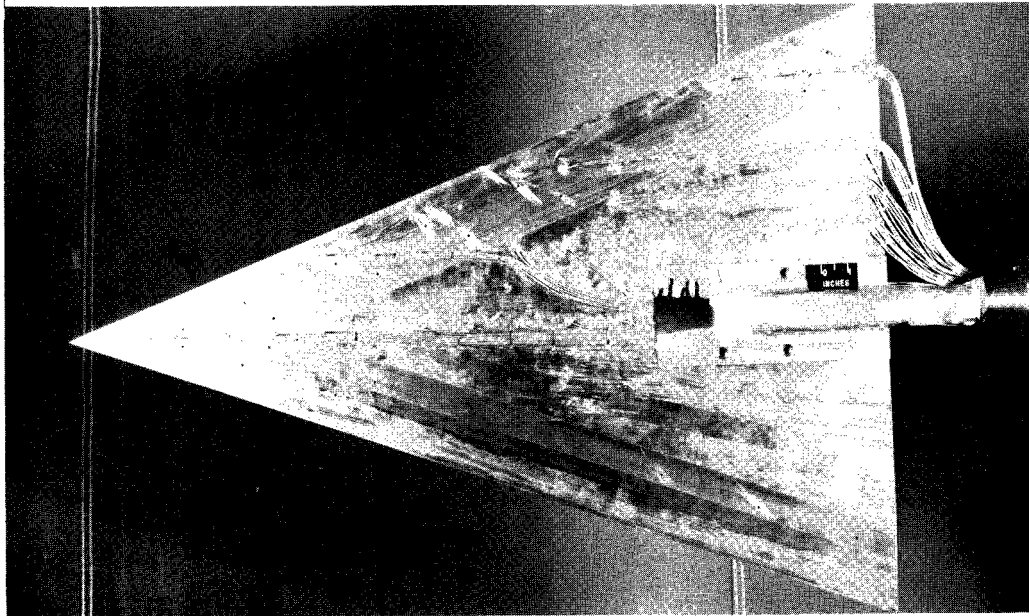
Instrumentation and sting attachment surface   L-65-4732

(b) Photographs.

Figure 2.- Concluded.
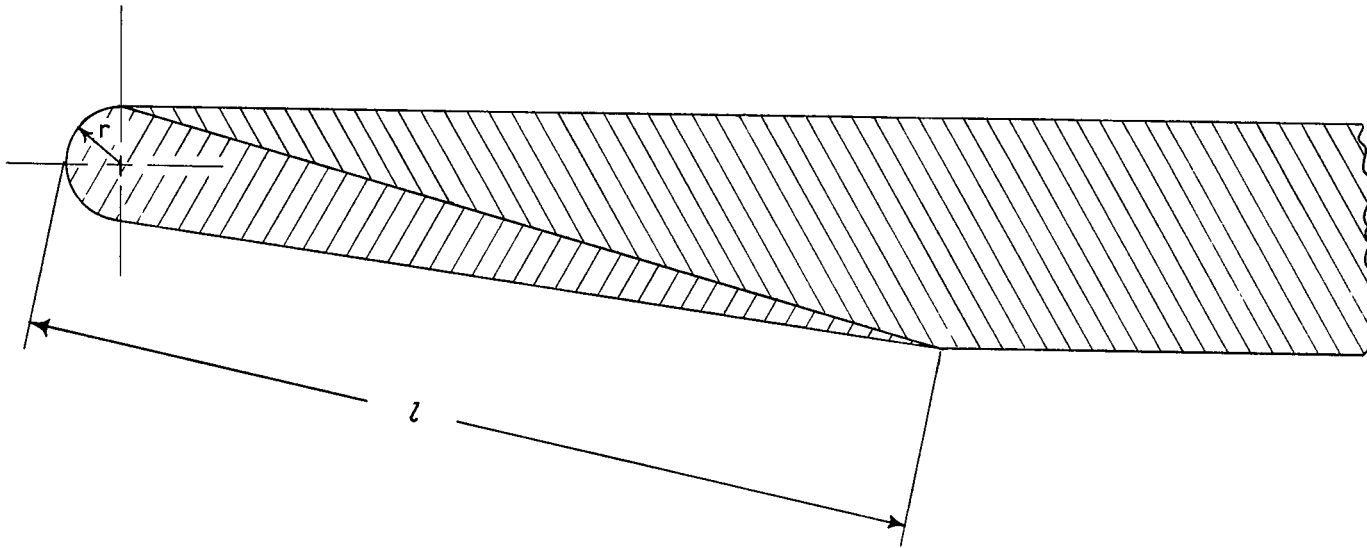
Typical section normal to wing leading edge

Configuration	Λ , degrees	r, cm	l, cm
2	60	0.317	8.90
3	60	.635	9.50
5	70	.317	8.90
6, 8	70	.635	9.50

Figure 3.- Blunt leading edges.
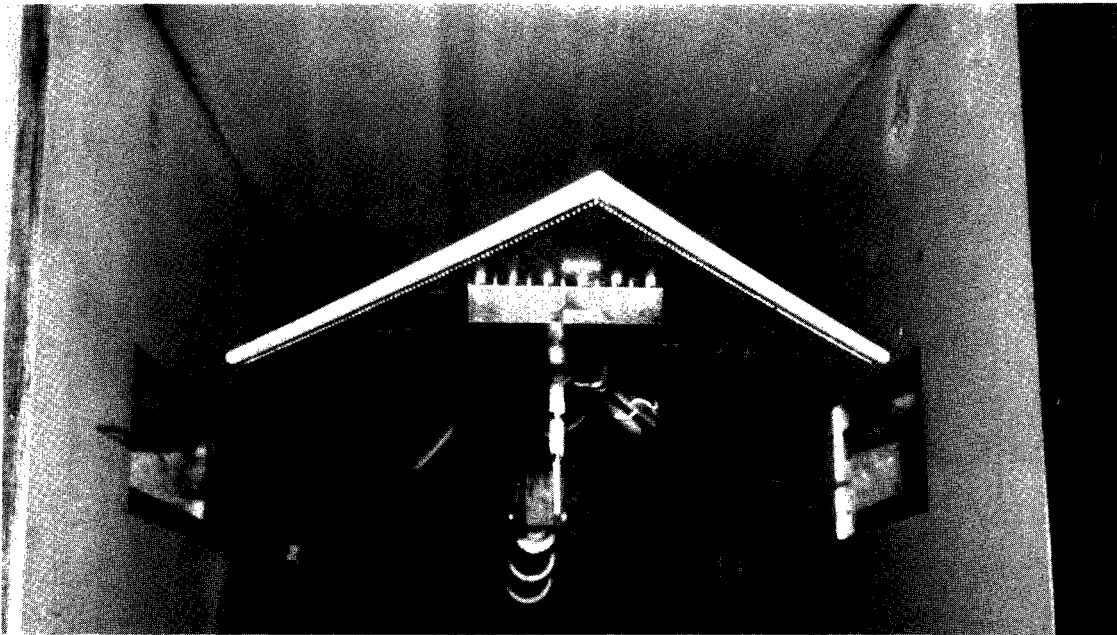
Front view   L-65-1418
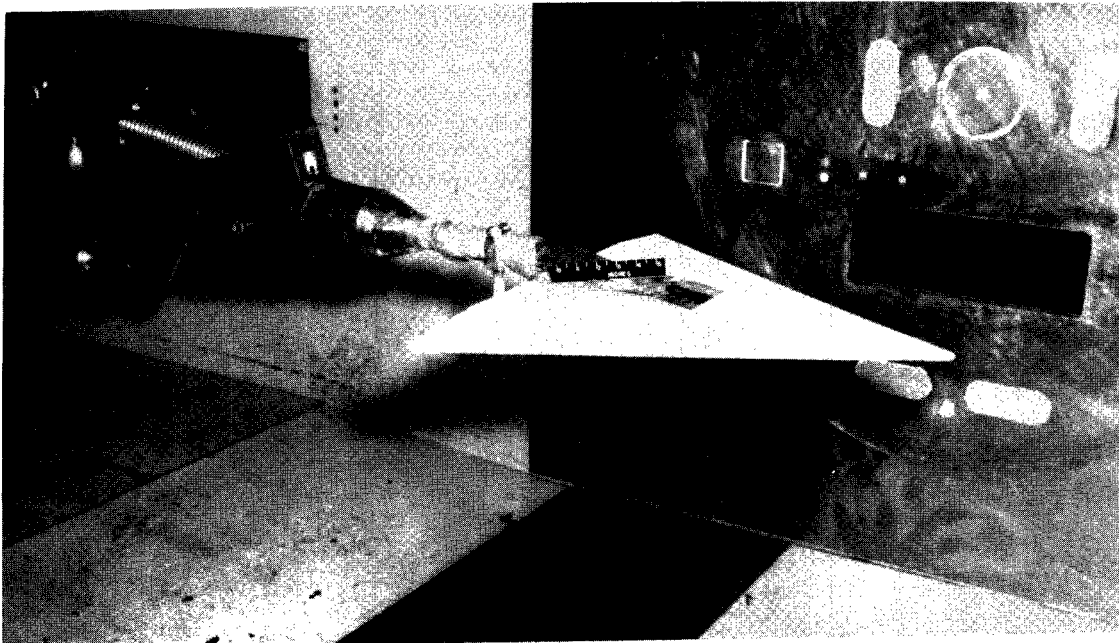
Side view   L-65-1416

Figure 4.- Photographs of typical model installation.
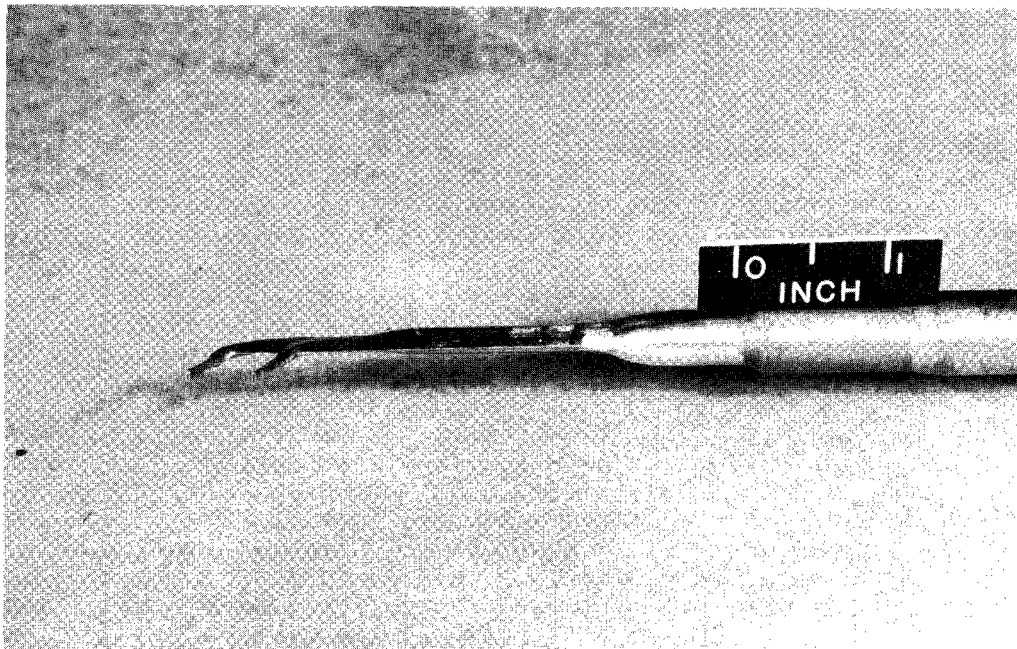
Front view   L-65-4729
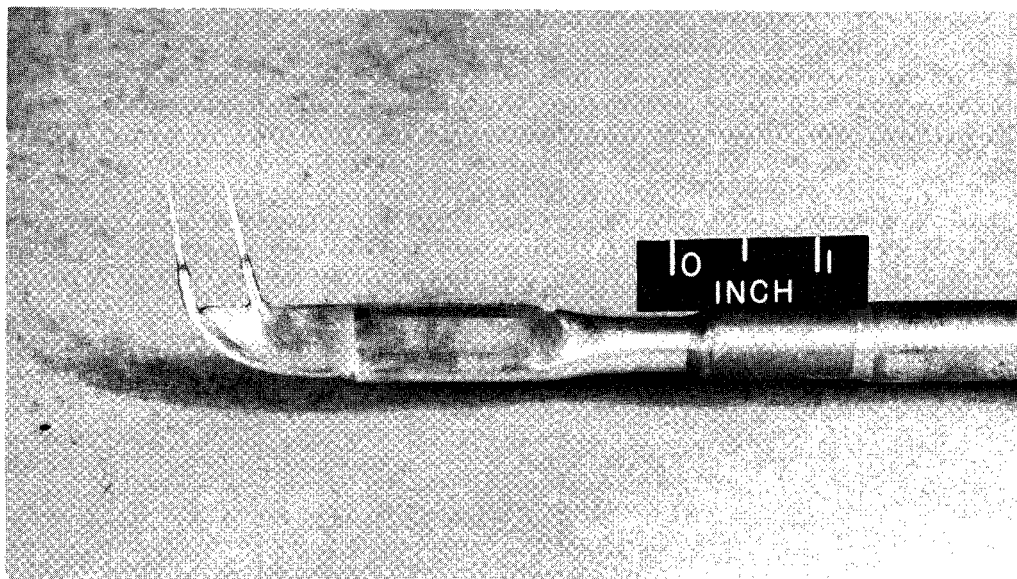
Side view   L-65-4730

(a) Probe head.

Figure 5.- Total-pressure survey apparatus.
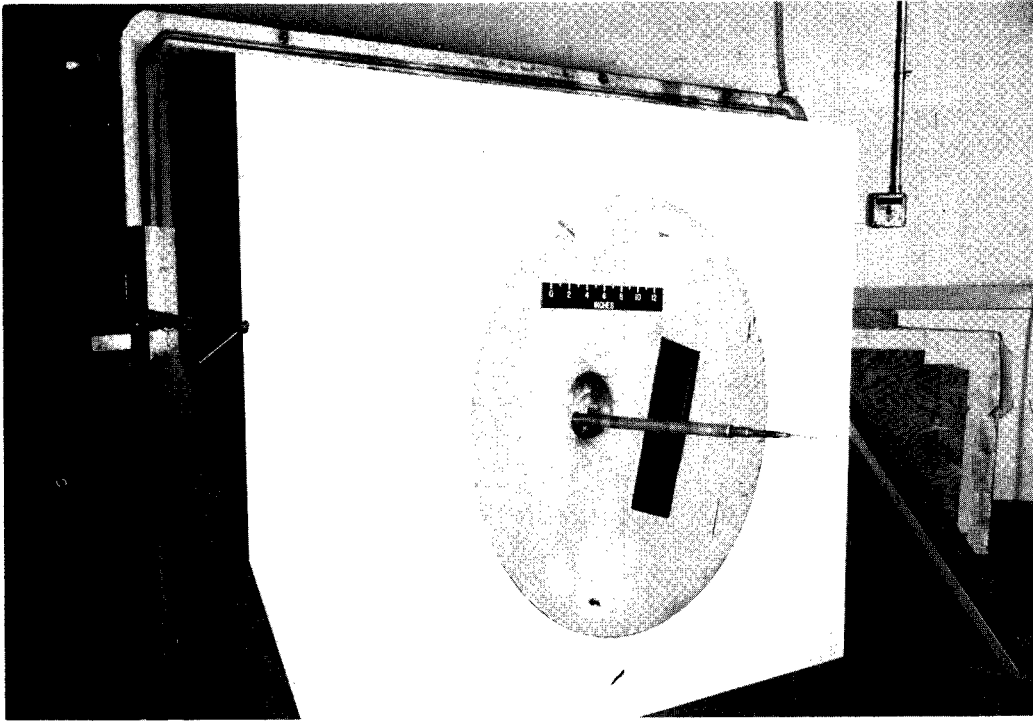
Inside of test-section door   L-65-4731
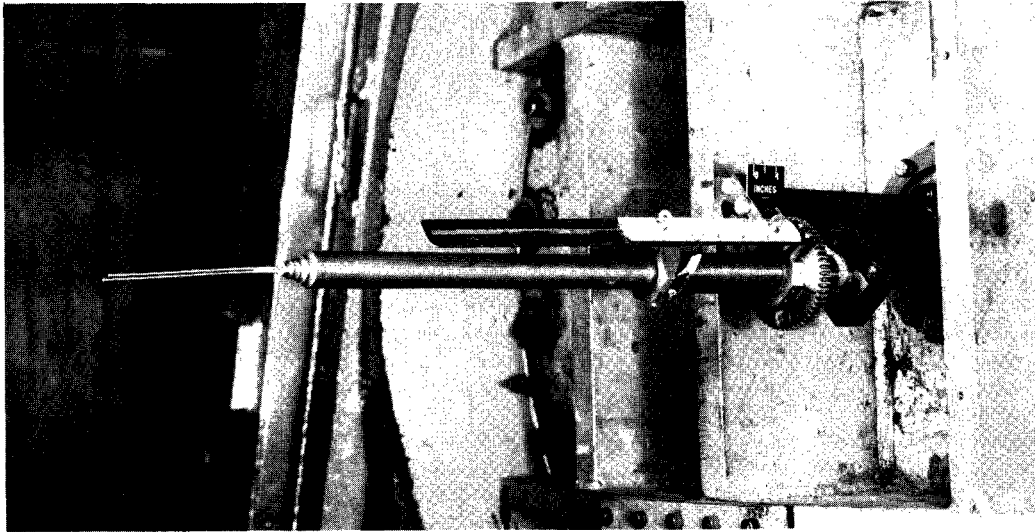
Outside of test-section door   L-65-4728

(b) Probe traversing mechanism.

Figure 5.- Concluded.

α = -10°

α = -5°

α = 0°

α = 5°

α = 10°
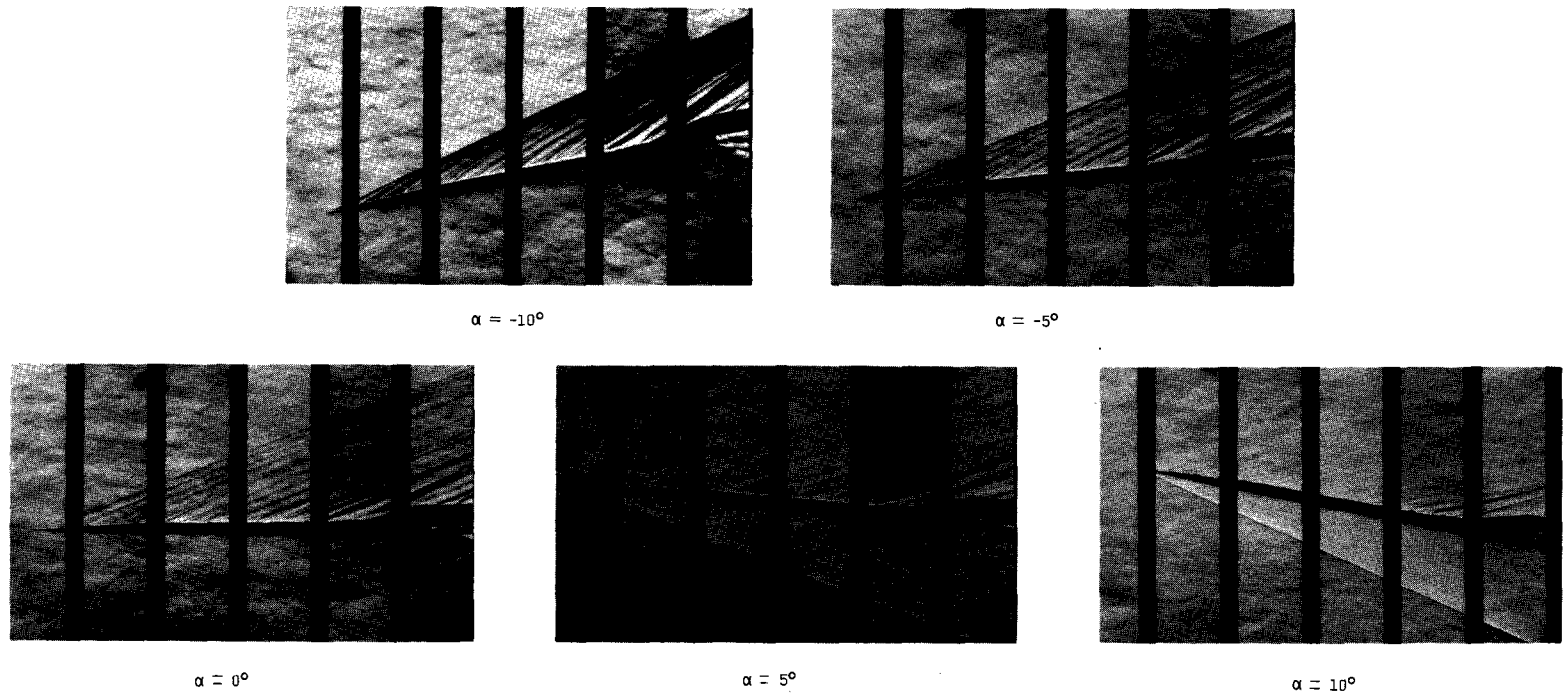
(a) M = 2.98.

L-66-4433

Figure 6.- Schlieren photographs of configuration 7. R = 9.85 × 10^6; Λ = 70°; r ≈ 0 cm.
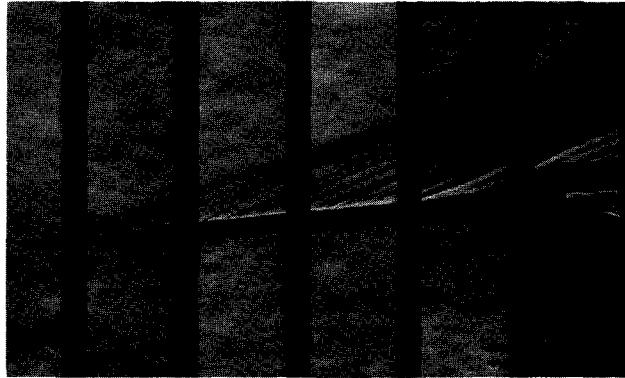
$\alpha = -5^{\circ}$
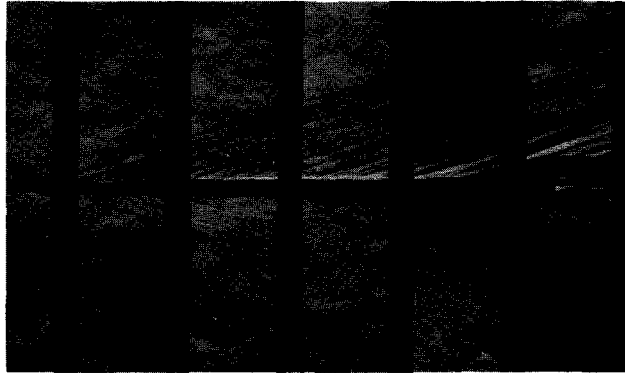
$\alpha = 0^{\circ}$
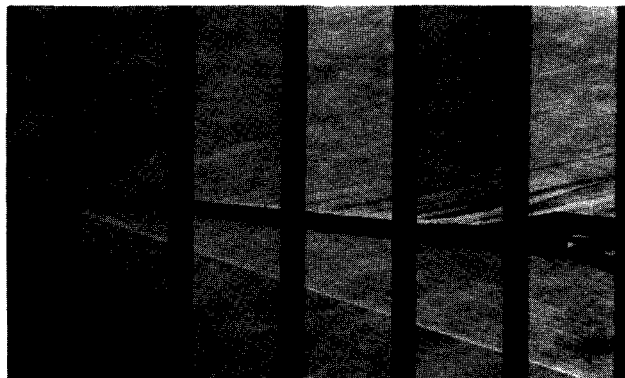
$\alpha = 5^{\circ}$

(b) M = 3.71.   L-66-4434

Figure 6.- Continued.

$\alpha = -5°$
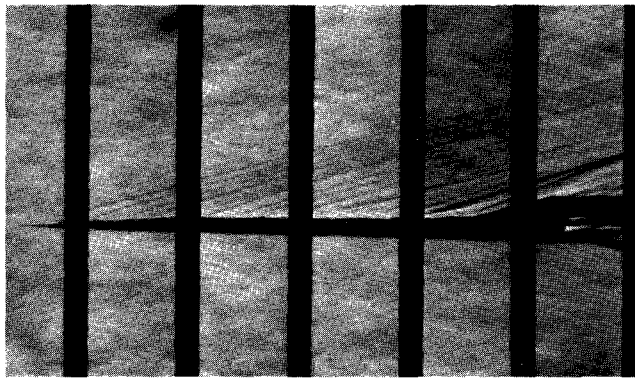
$\alpha = 0°$

$\alpha = 5°$

(c) M = 4.44.   L-66-4435

Figure 6.- Concluded.

(a) $\alpha = -5^0$.

(b) $\alpha = 0^0$.

(c) $\alpha = 5^0$.
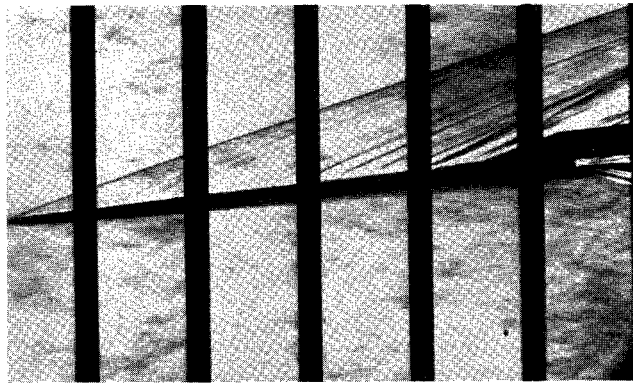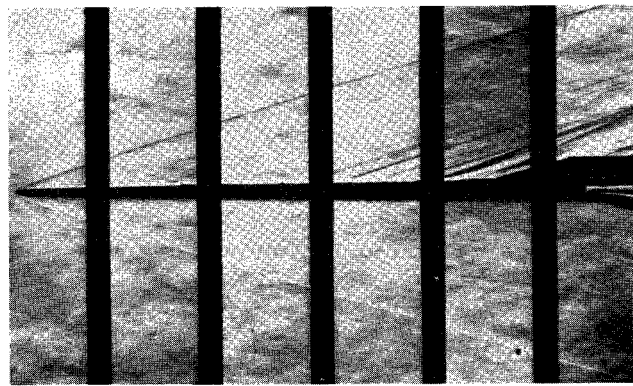
L-66-4436

Figure 7.- Schlieren photographs of configuration 8. $M = 3.71$; $R = 9.85 \times 10^6$; $\Lambda = 70^0$; $r = 0.635$ cm.
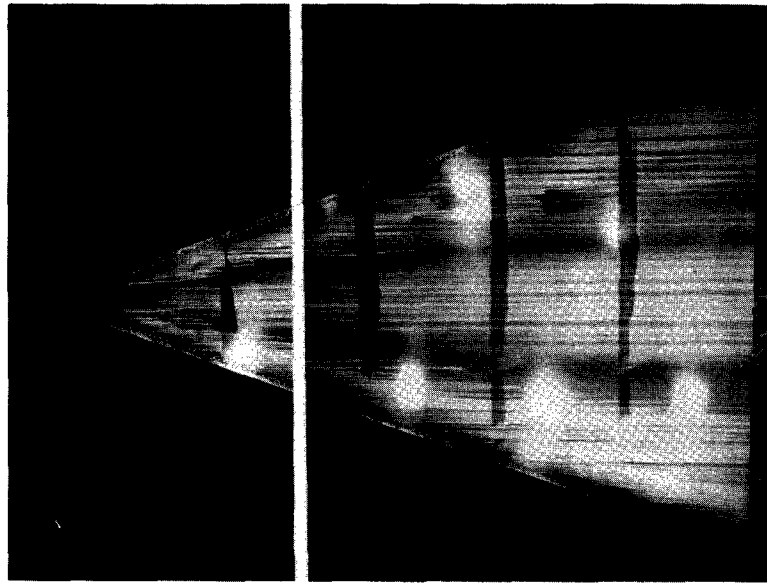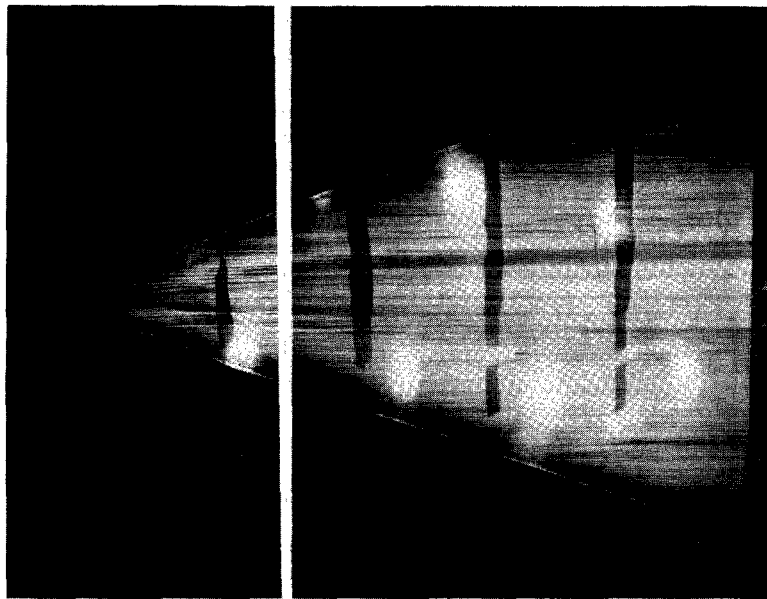
M = 2.98

M = 3.71

(a) α = 0°.   L-66-4437

Figure 8.- Oil-flow photographs of configuration 7. R = 9.85 × 10⁶; Λ = 70°; r ≈ 0 cm.
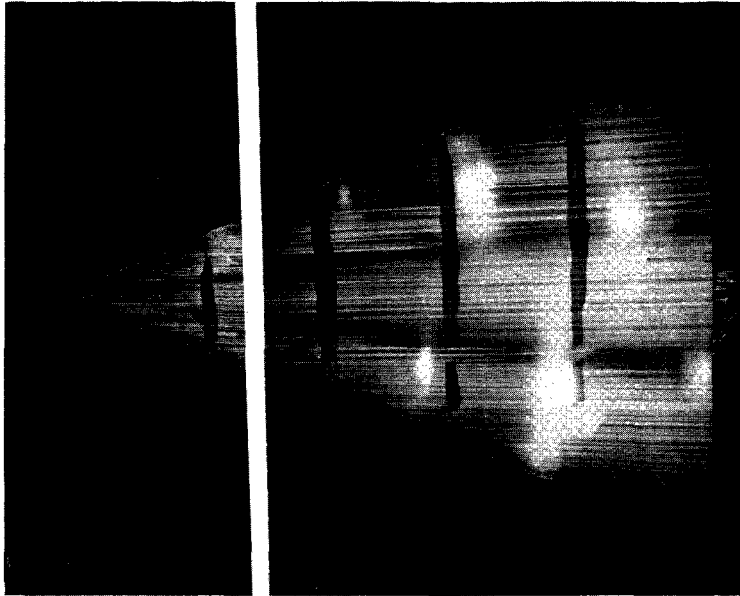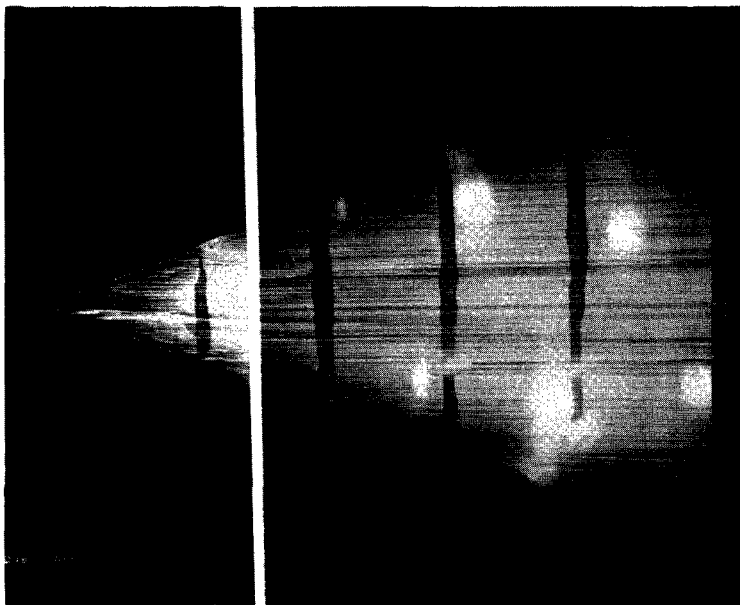
M ◻ 2.98

M = 3.71

(b) α = 5⁰ (windward).   L-66-4438

Figure 8.- Continued.

L-66-4439

Coiled vortex sheet

Secondary separation

Attachment line
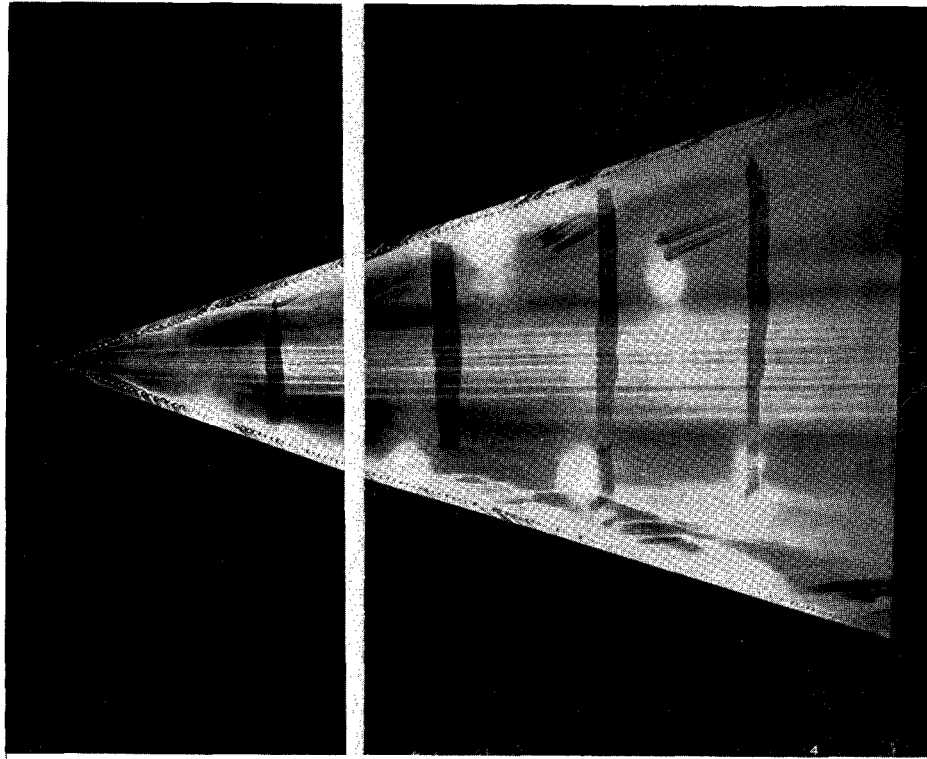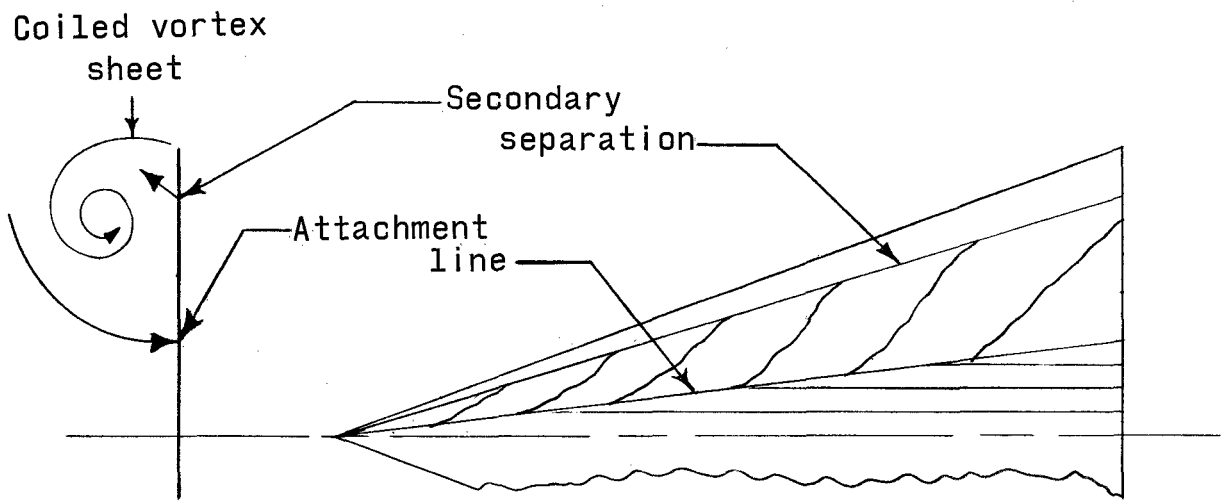
(c) M = 2.98; α = -5⁰ (leeward).

Figure 8.- Continued.

L-66-4440

Oblique
shock
wave

Flow attached to surface
near leading edge

Separation
at base of
shock wave

Coiled
vortex
sheet
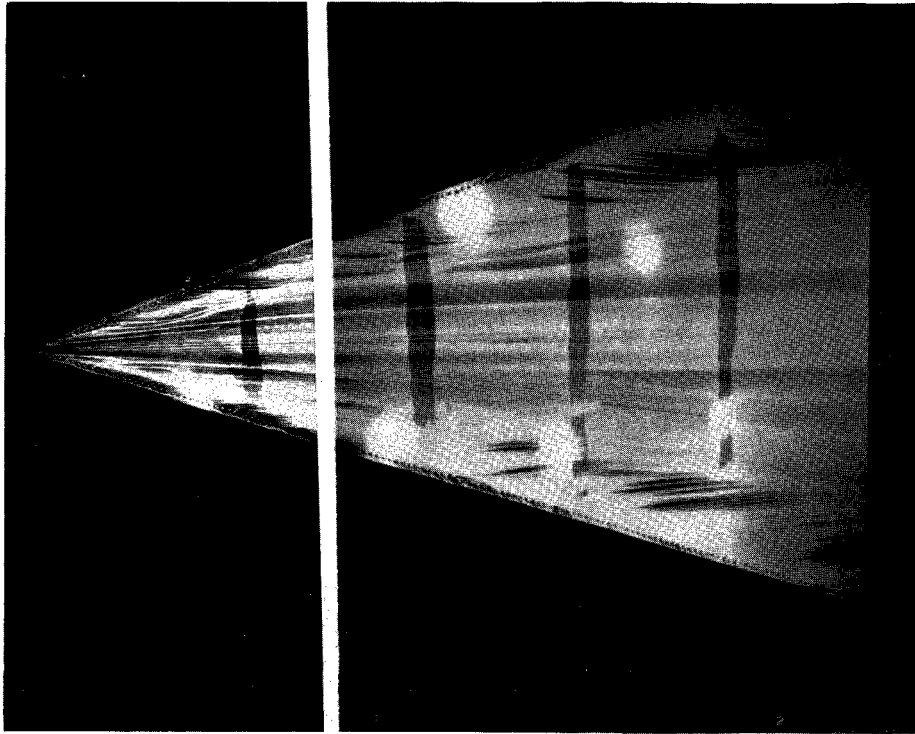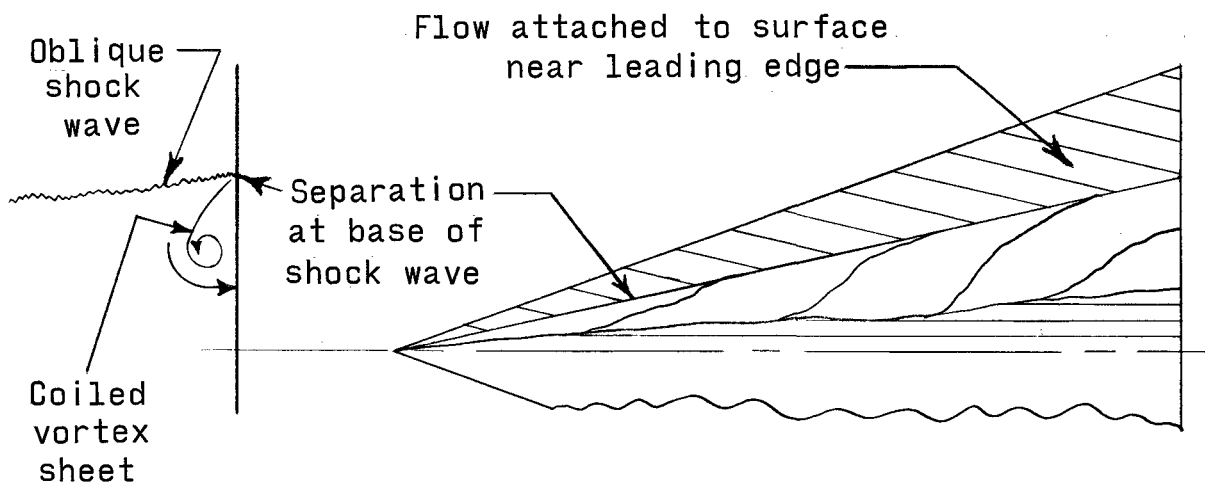
(d) M = 3.71; α = -5° (leeward).

Figure 8.- Concluded.
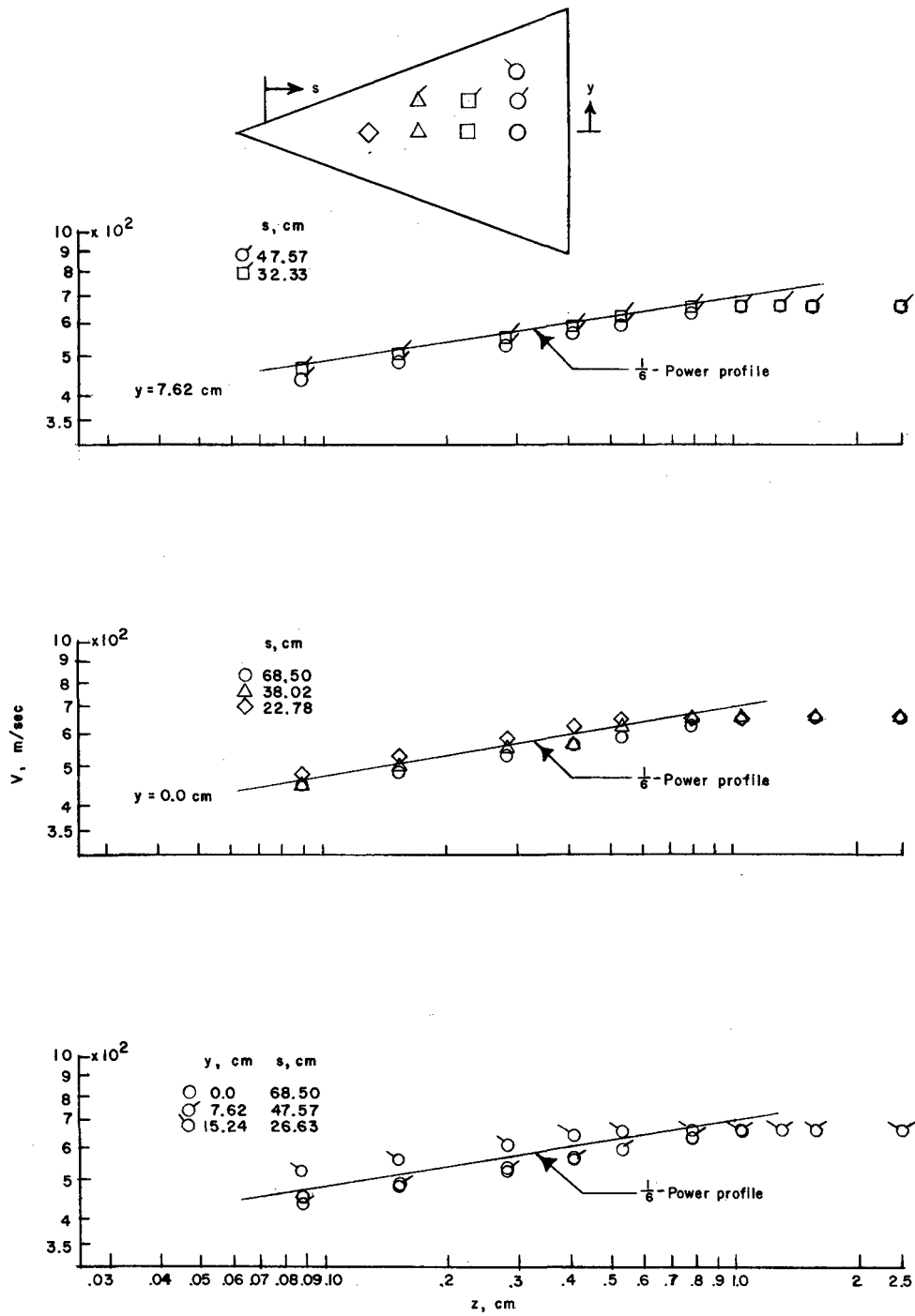
(a) α = 0°.

Figure 9.- Boundary-layer velocity profiles for configuration 7. M = 2.98; R = 9.85 × 10⁶; Λ = 70°; r ≈ 0 cm.

36

(b) $\alpha = 5^0$.
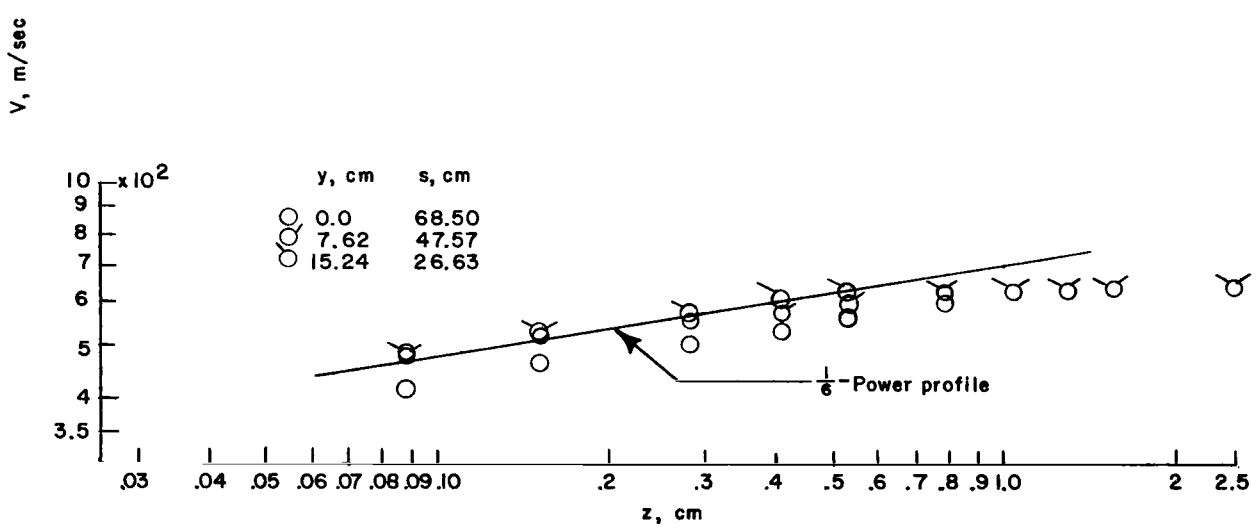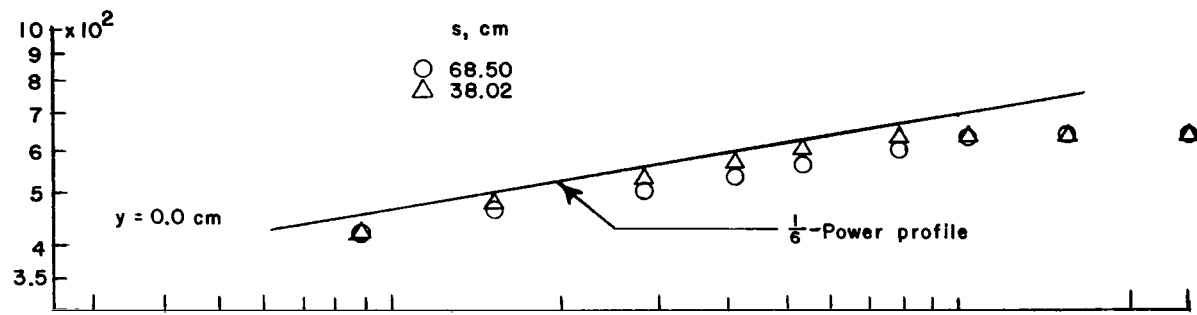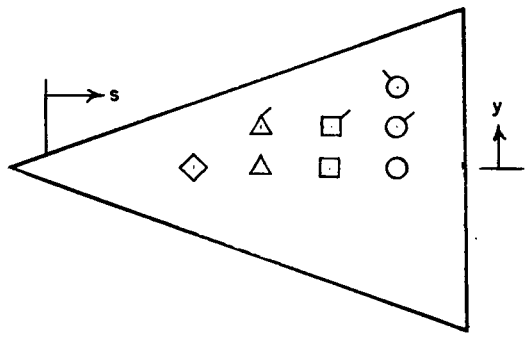
Figure 9.- Continued.

(c) $\alpha = -5^0$.
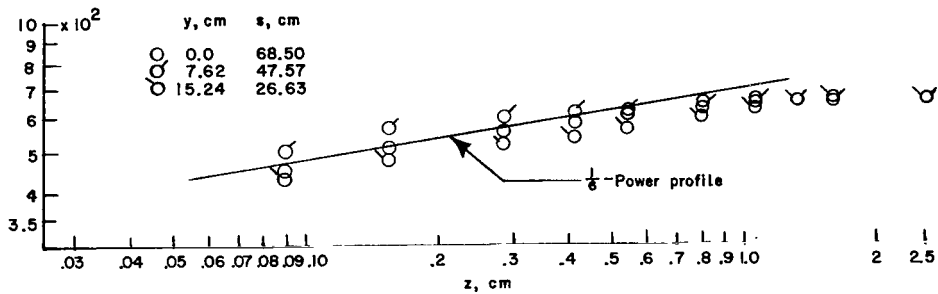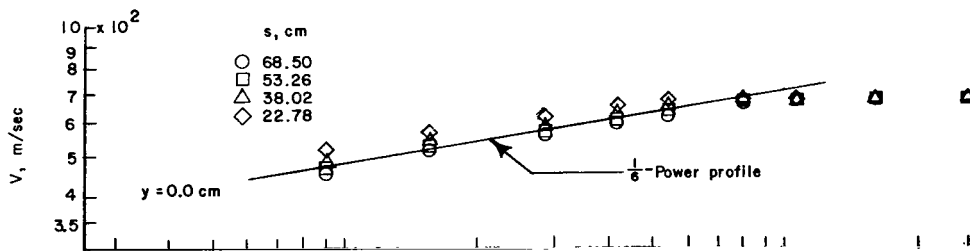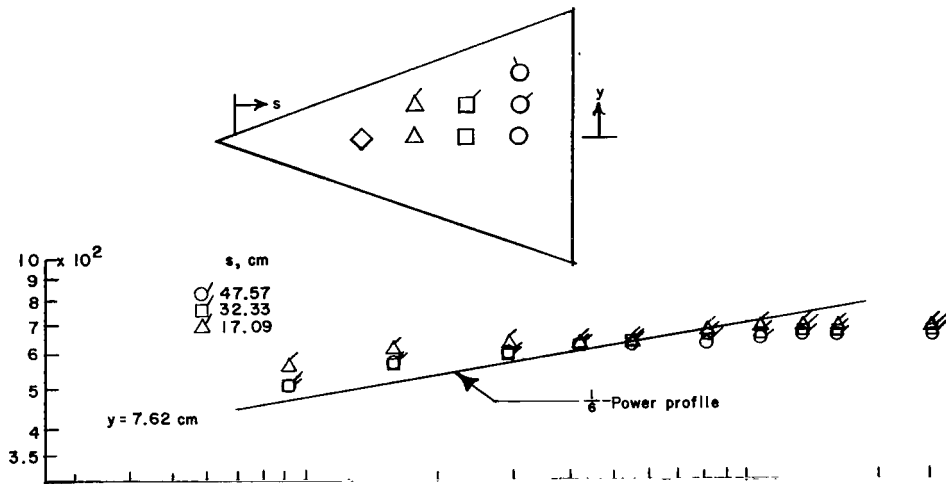
Figure 9.- Concluded.
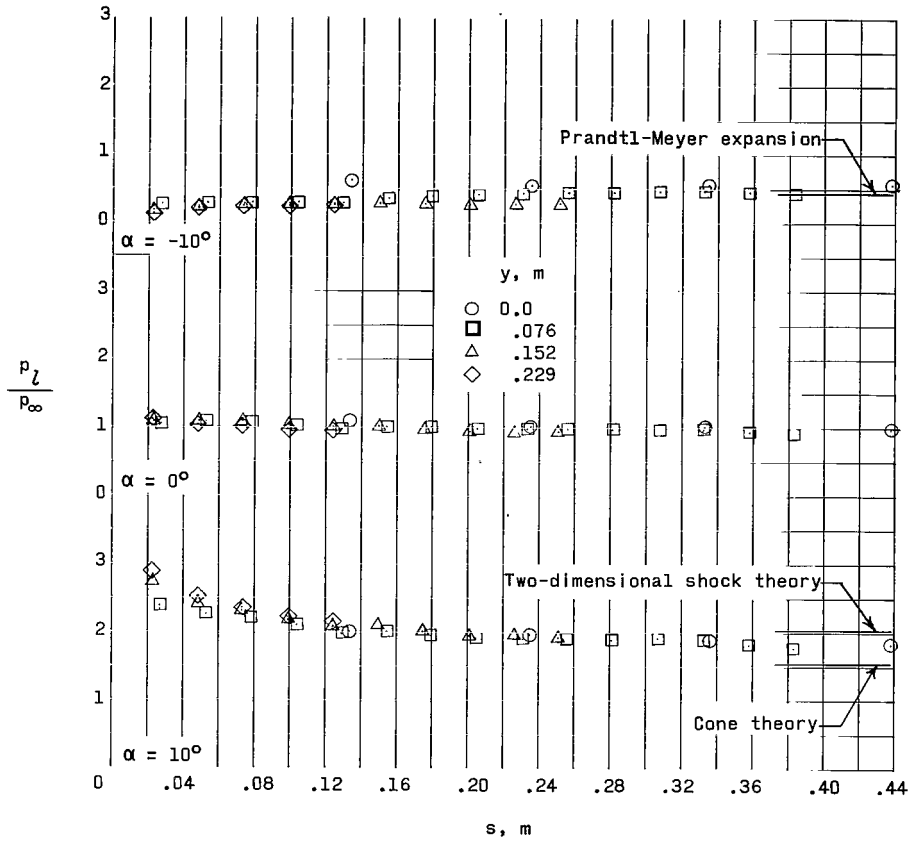
(a) M = 2.98; R = 9.85 × 10^6.

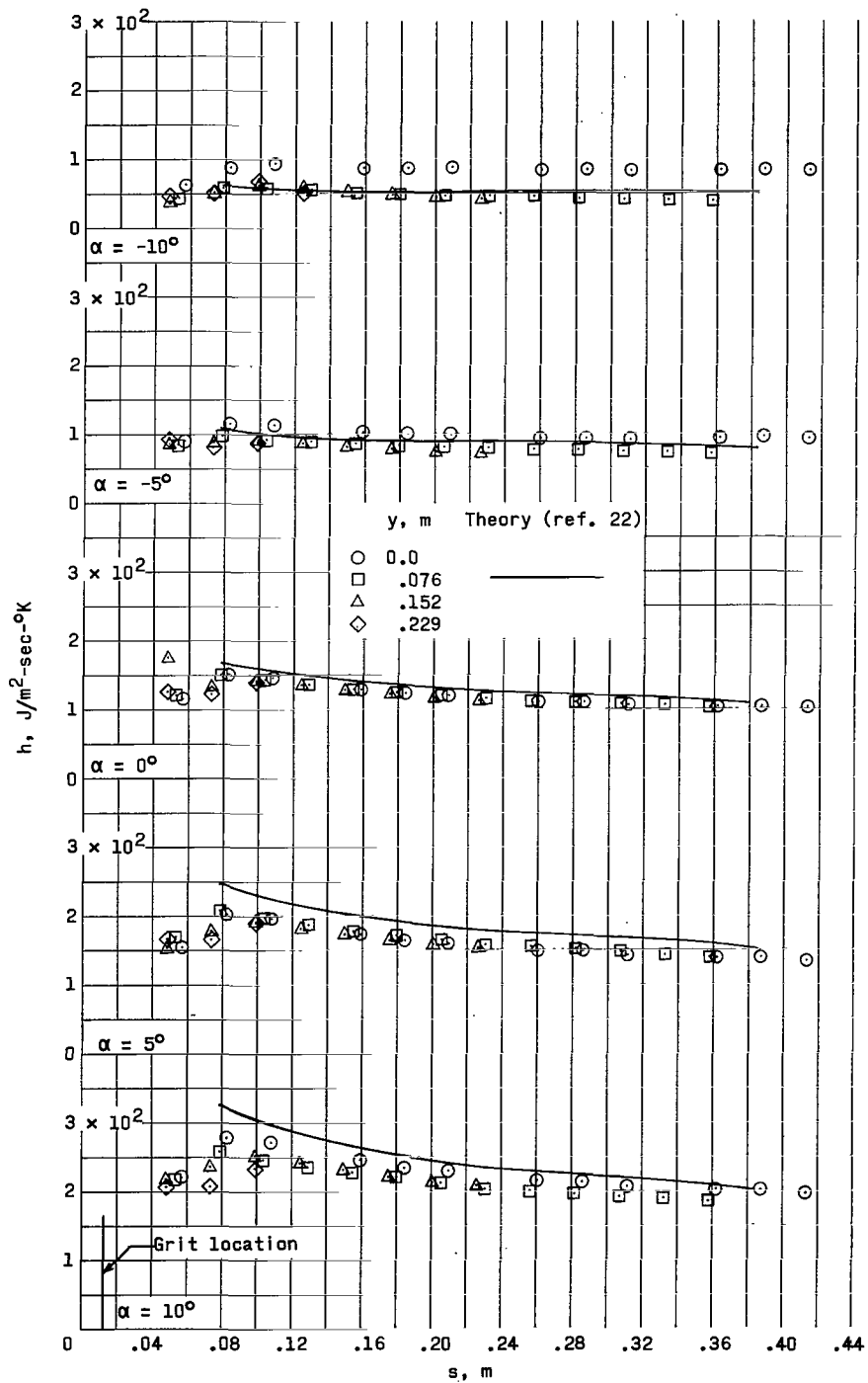Figure 10.- Effect of angle of attack on the surface-pressure distributions of configuration 1. Λ = 60°; r ≈ 0 cm.
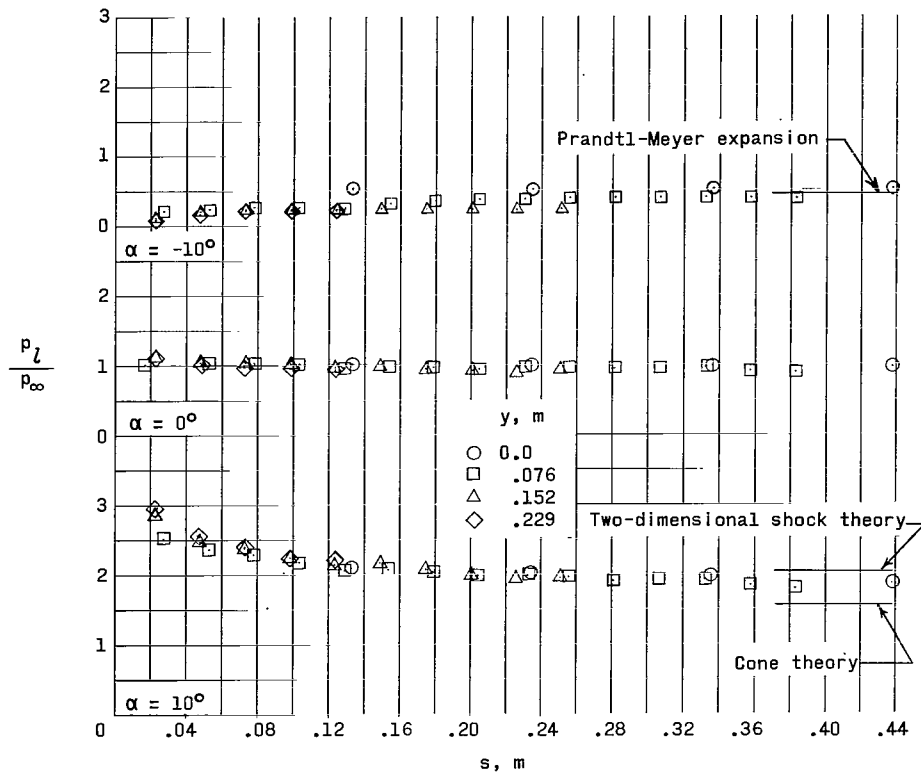
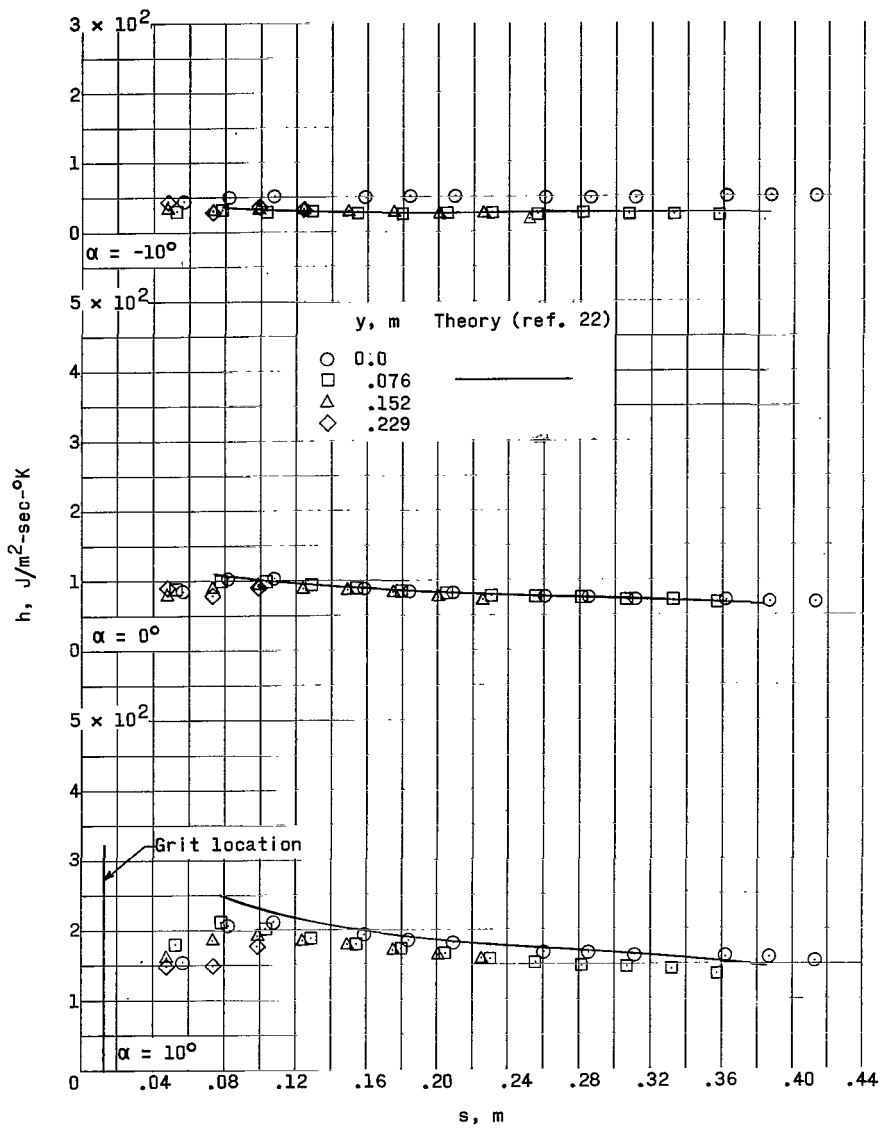(b) M = 2.98; R = 19.7 × 10^6.

Figure 10.- Continued.
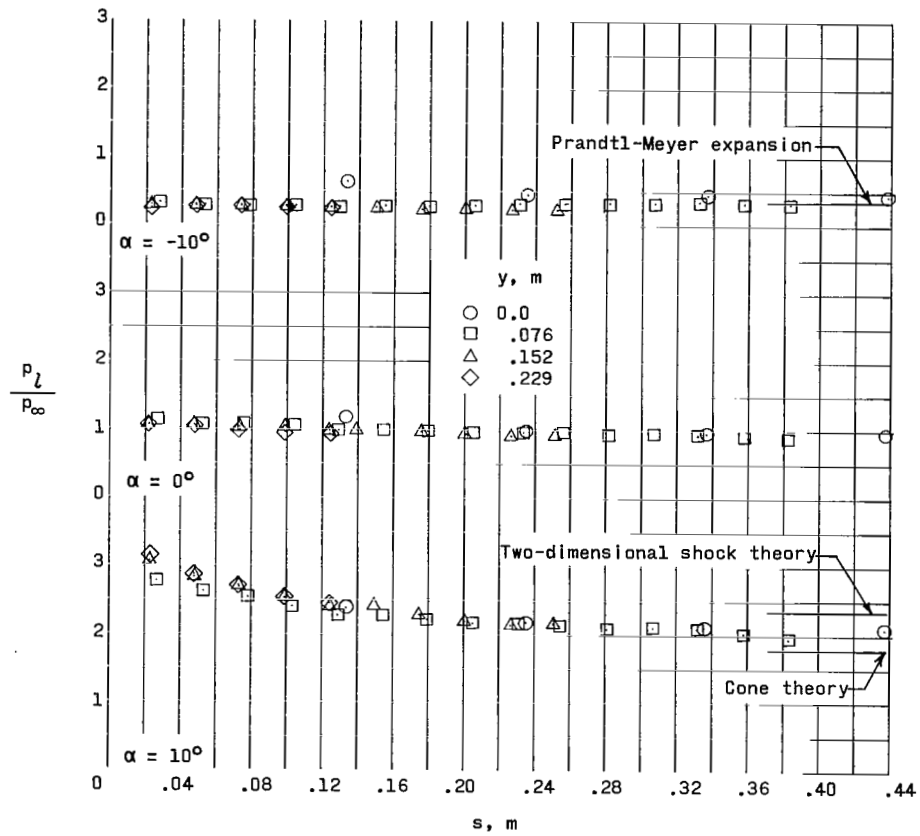
(c) $M = 3.71$; $R = 9.85 \times 10^6$.

Figure 10.- Continued.
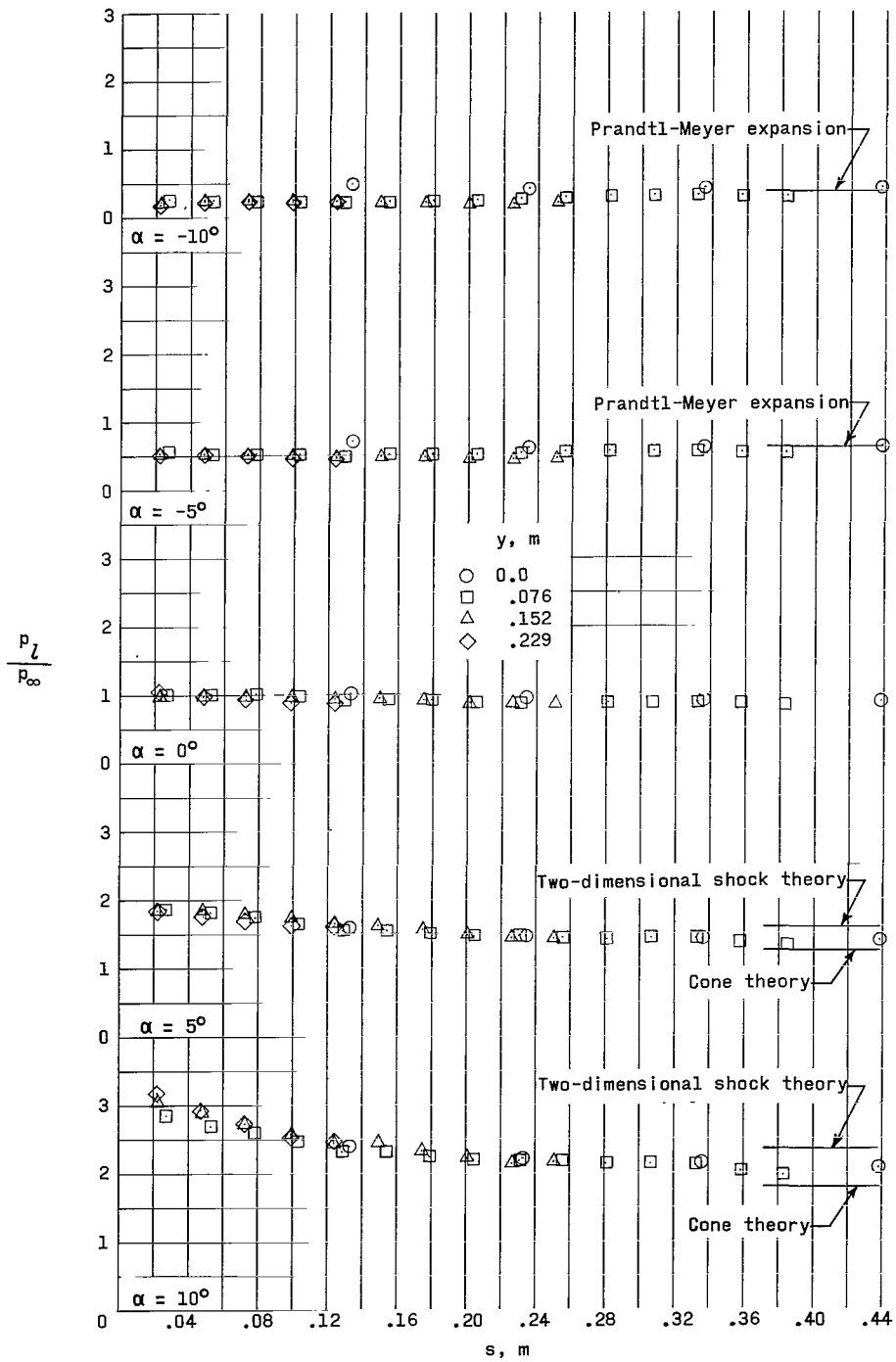
(d) $M = 3.71$; $R = 19.7 \times 10^6$.

Figure 10.- Continued.
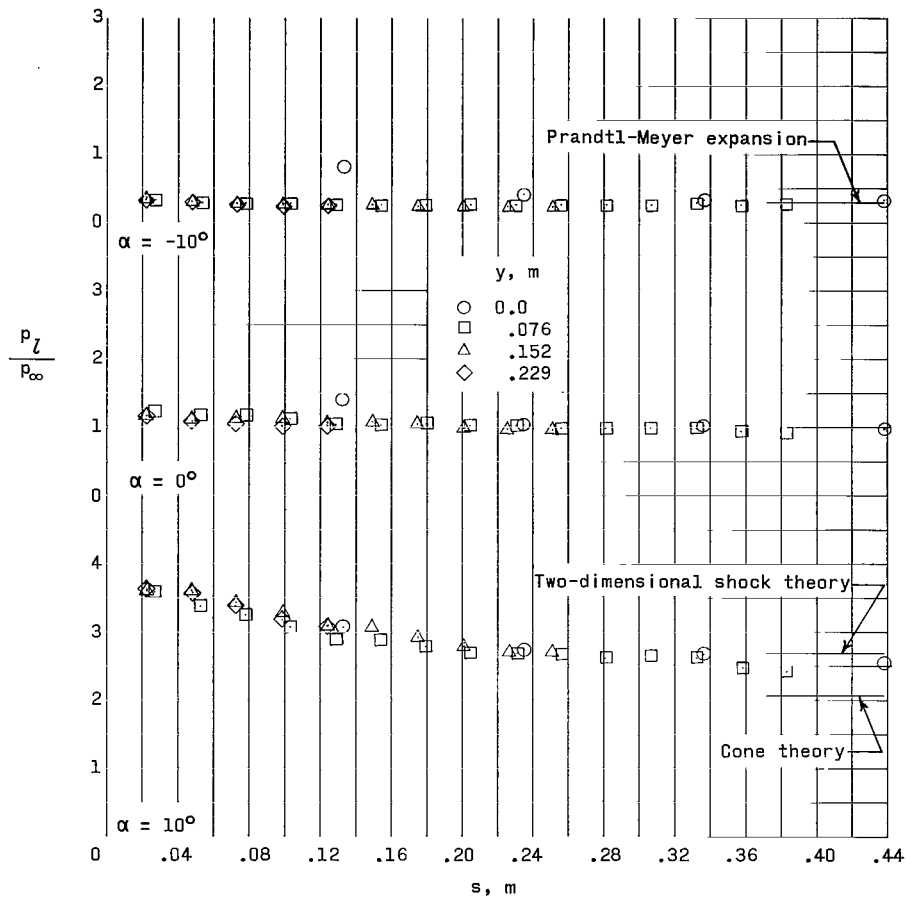
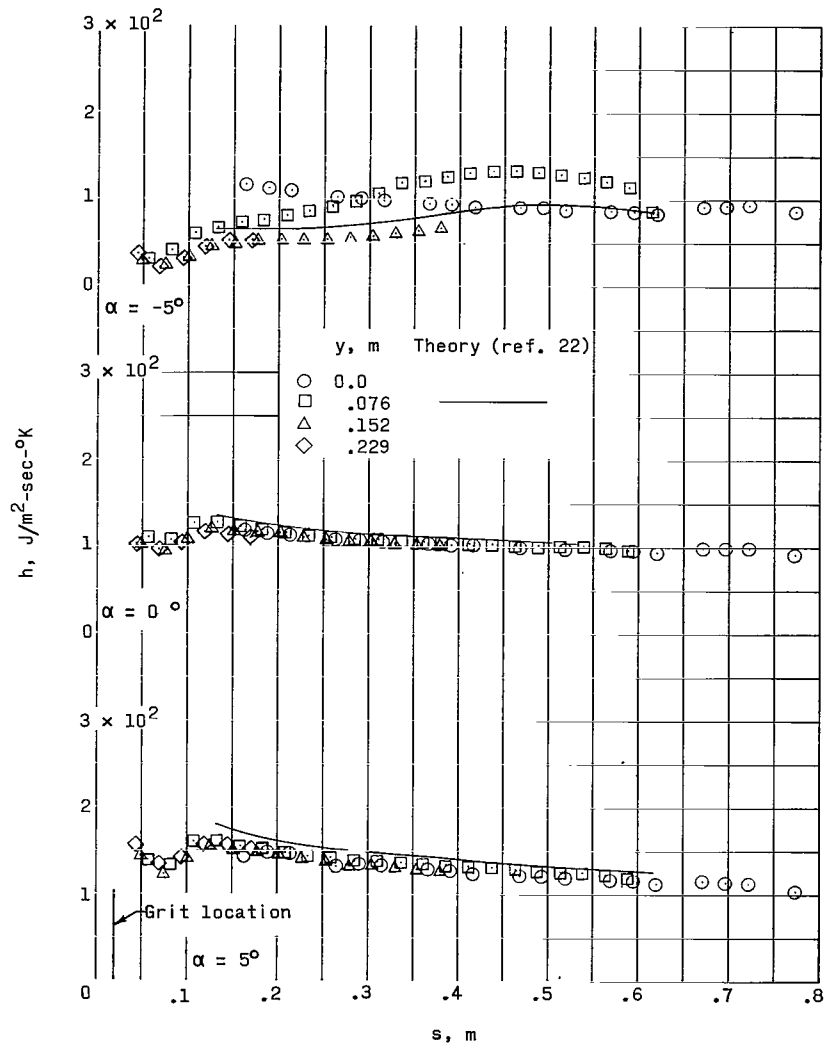(e) $M = 4.44$; $R = 9.85 \times 10^6$.

Figure 10.- Continued.
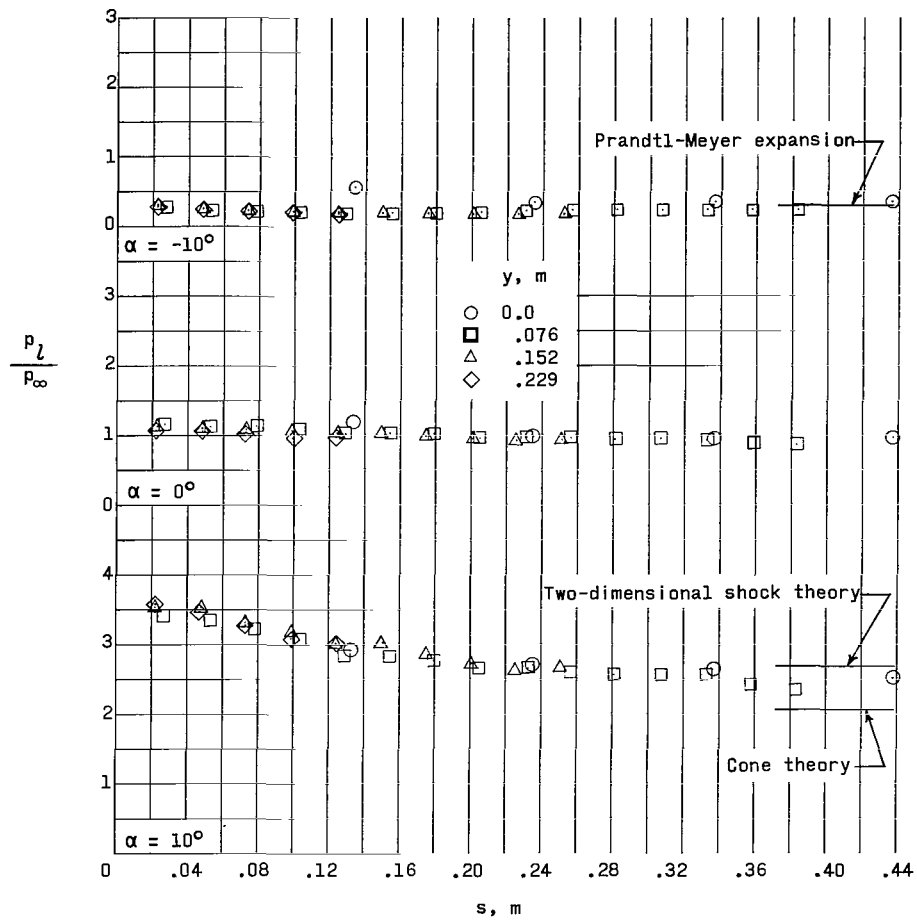
(f) $M = 4.44$; $R = 19.7 \times 10^6$.

Figure 10.- Concluded.
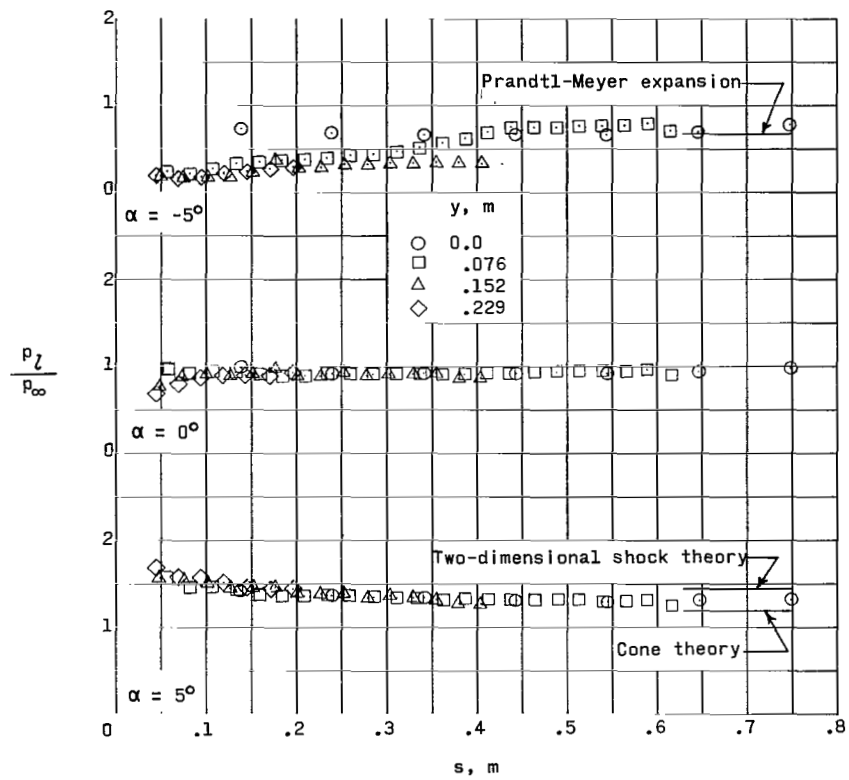
(a) M = 2.98; R = 9.85 × 10⁶.

Figure 11.- Effect of angle of attack on the surface-pressure distributions of configuration 4. Λ = 70°; r ≈ 0 cm.

45
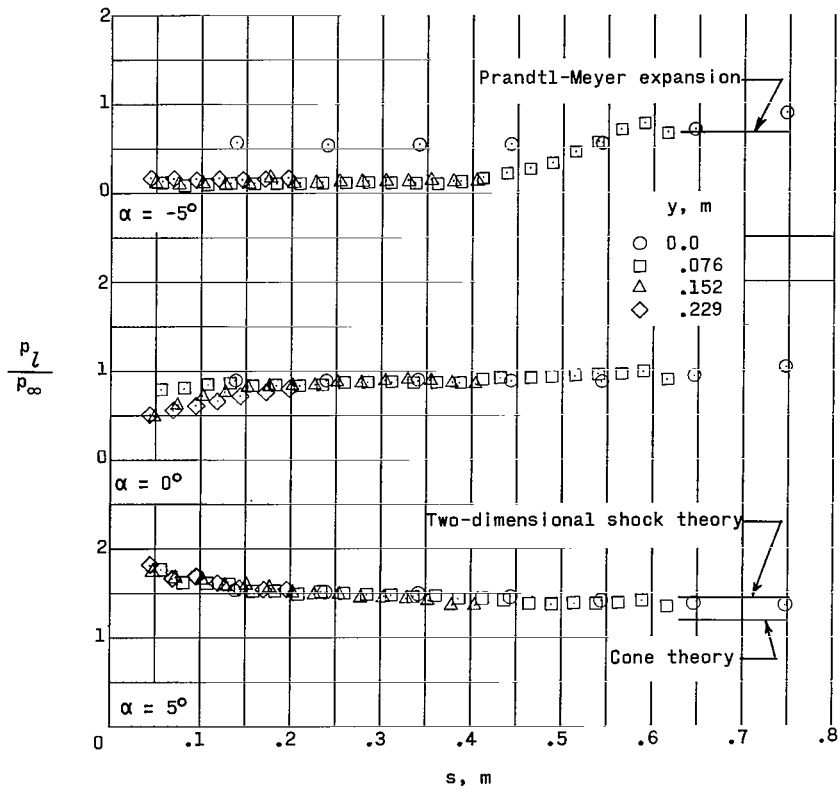
(b) M = 2.98; R = 19.7 × 10⁶.

Figure 11.- Continued.
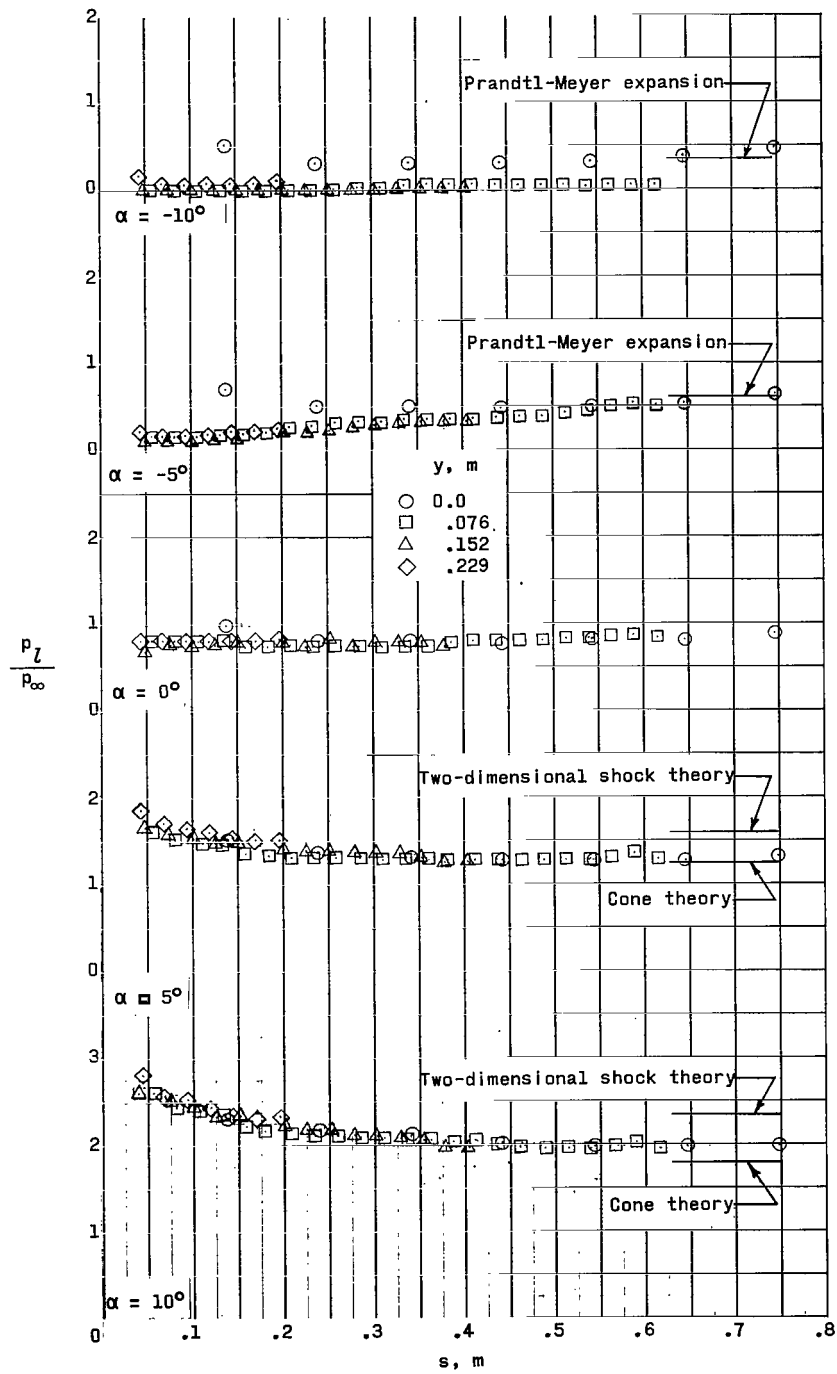
(c) M = 3.71; R = 9.85 × 10⁶.

Figure 11.- Continued.
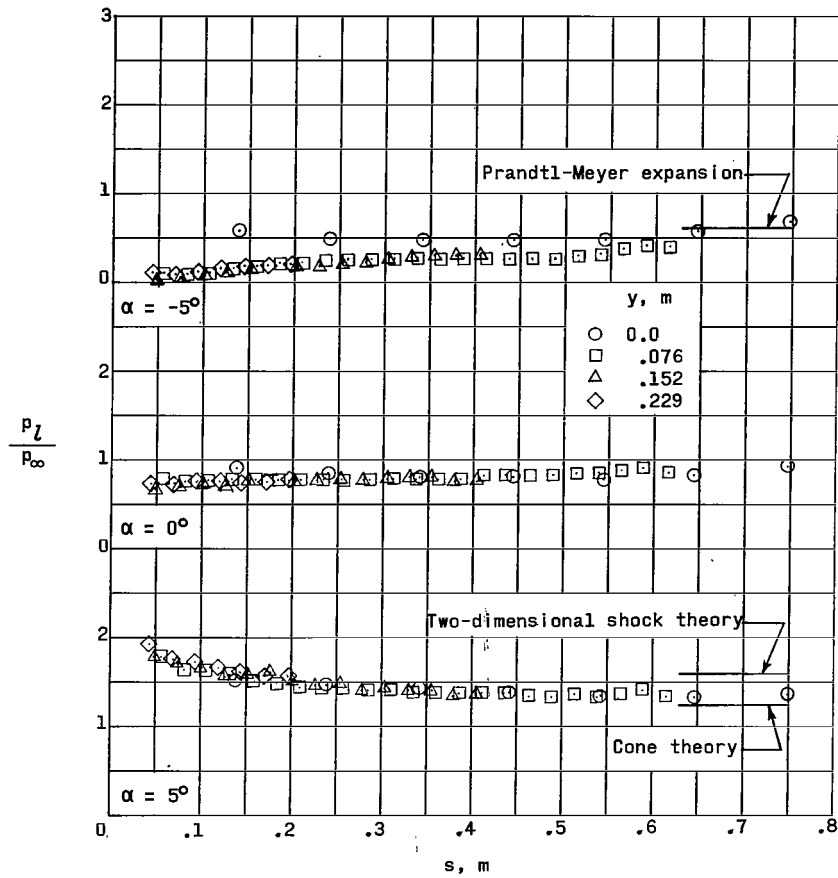
(d) M = 3.71; R = 19.7 × 10⁶.

Figure 11.- Continued.
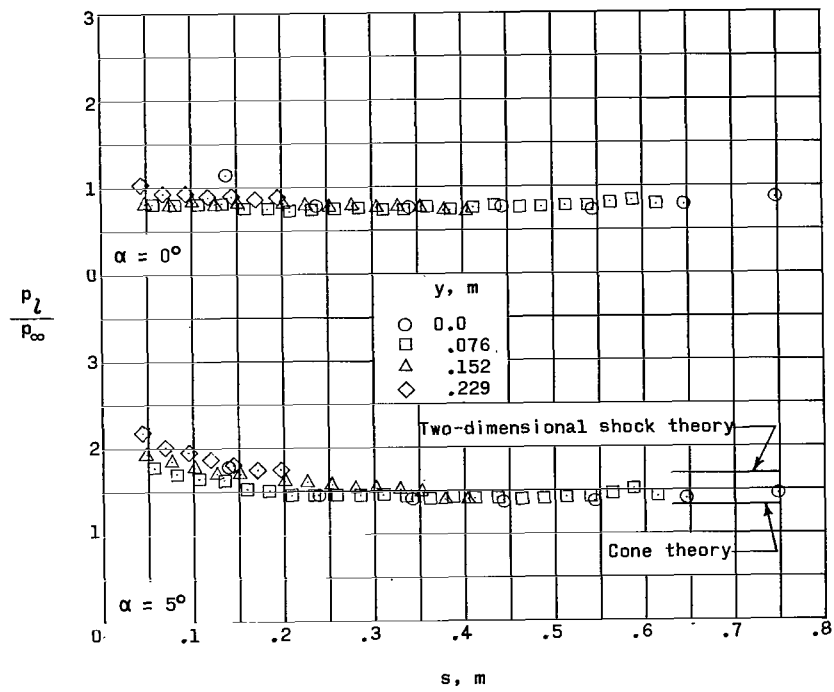
(e) $M = 4.44$; $R = 9.85 \times 10^6$.

Figure 11.- Continued.
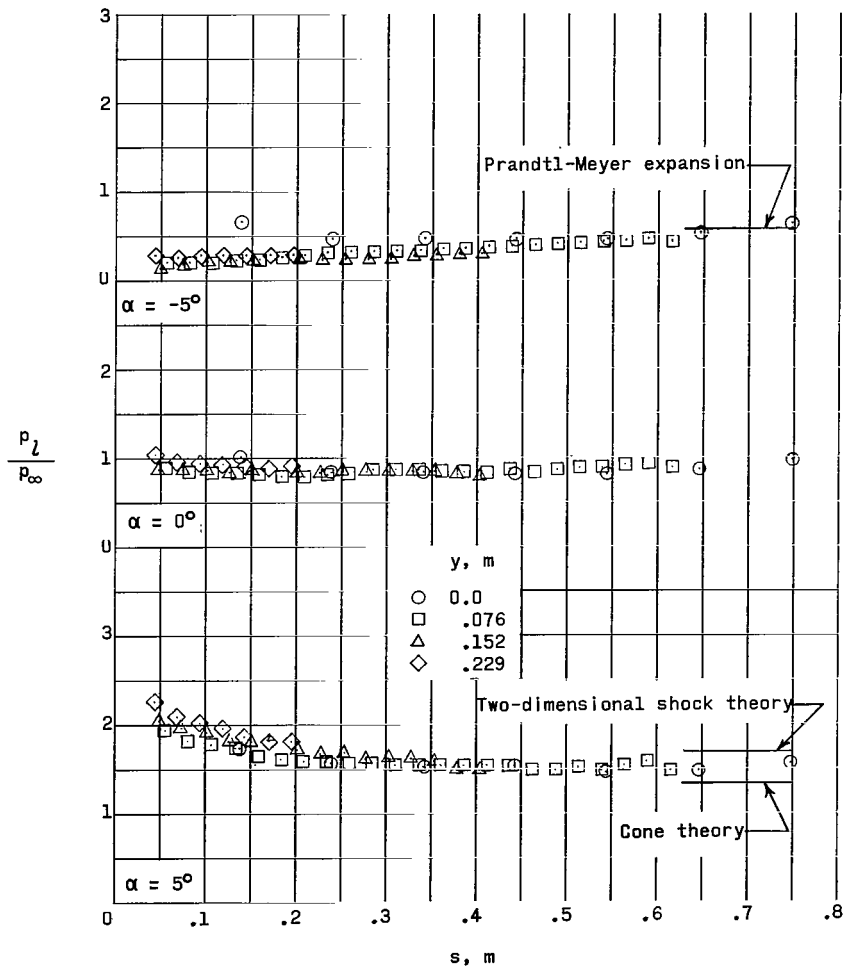
(f) $M = 4.44$; $R = 19.7 \times 10^6$.
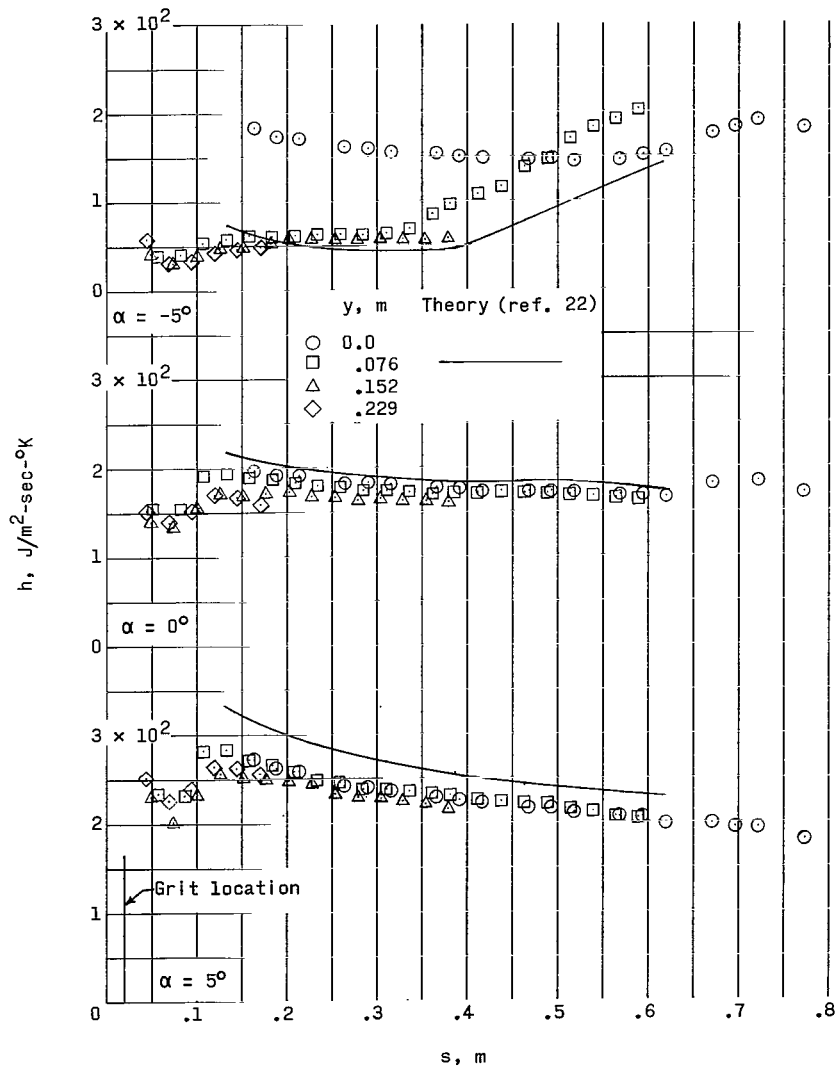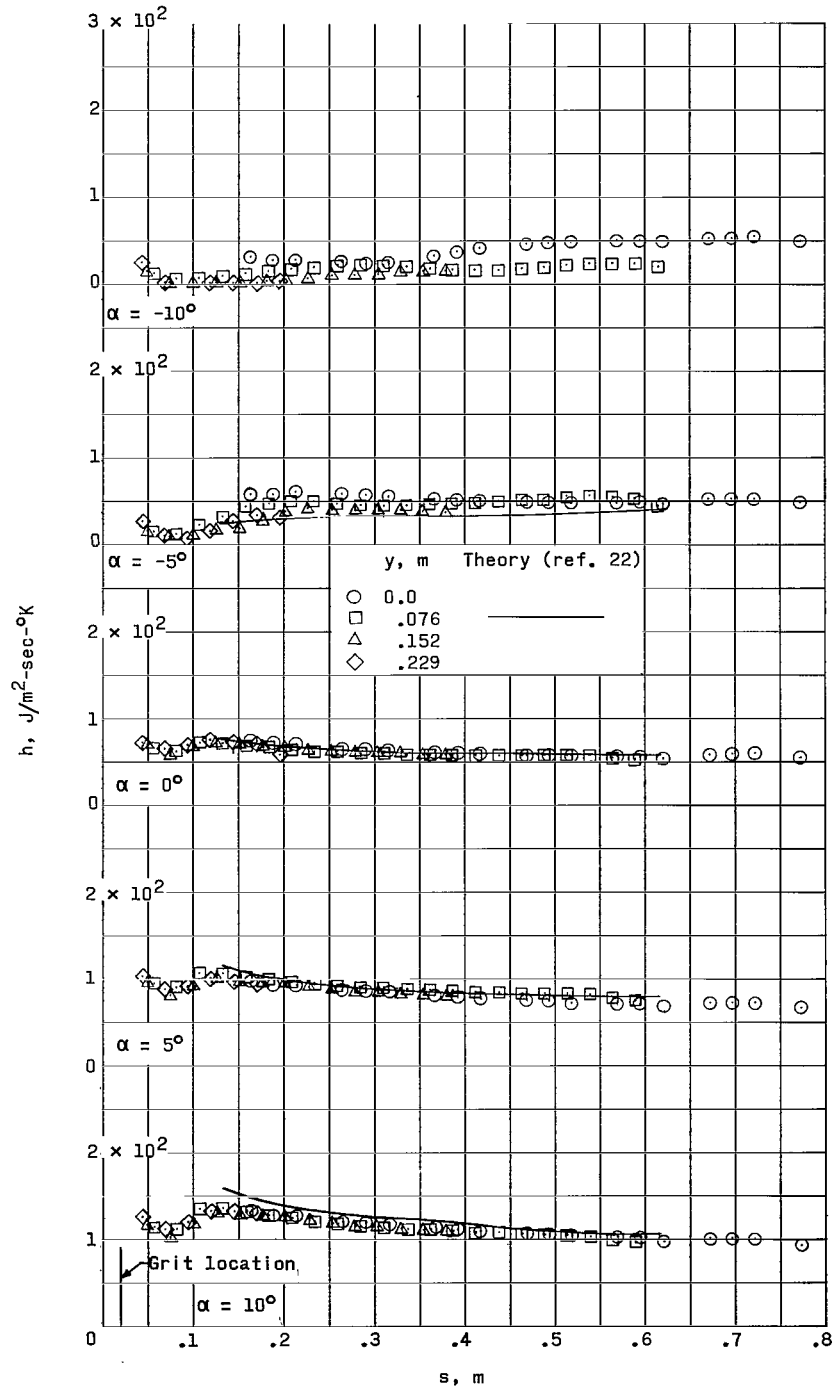
Figure 11.- Concluded.
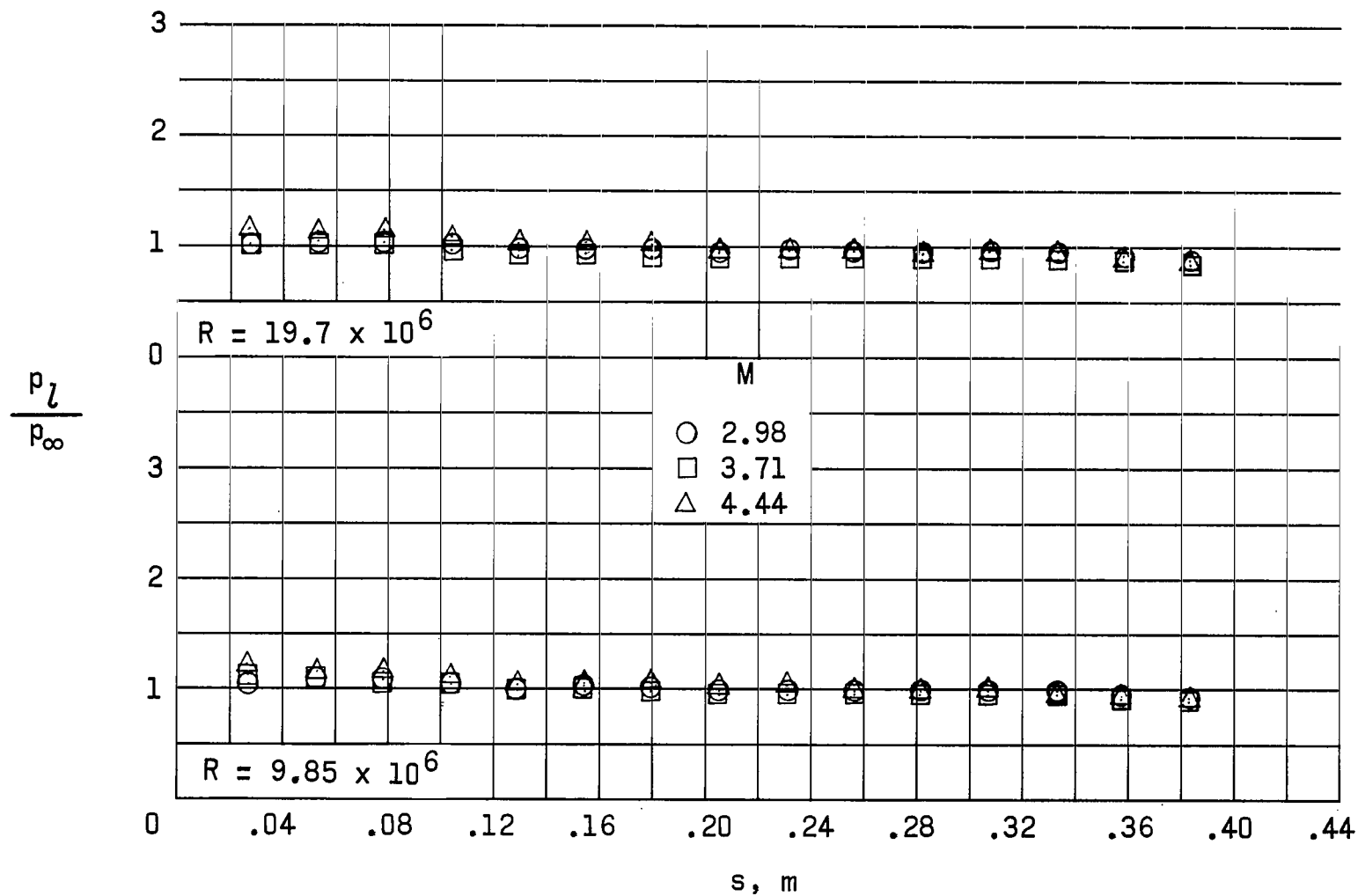
Figure 12.- Effect of Mach number on the surface-pressure distributions of configuration 1. $\alpha = 0^0$; $y = 0.076$ m; $\Lambda = 60^0$; $r \approx 0$ cm.
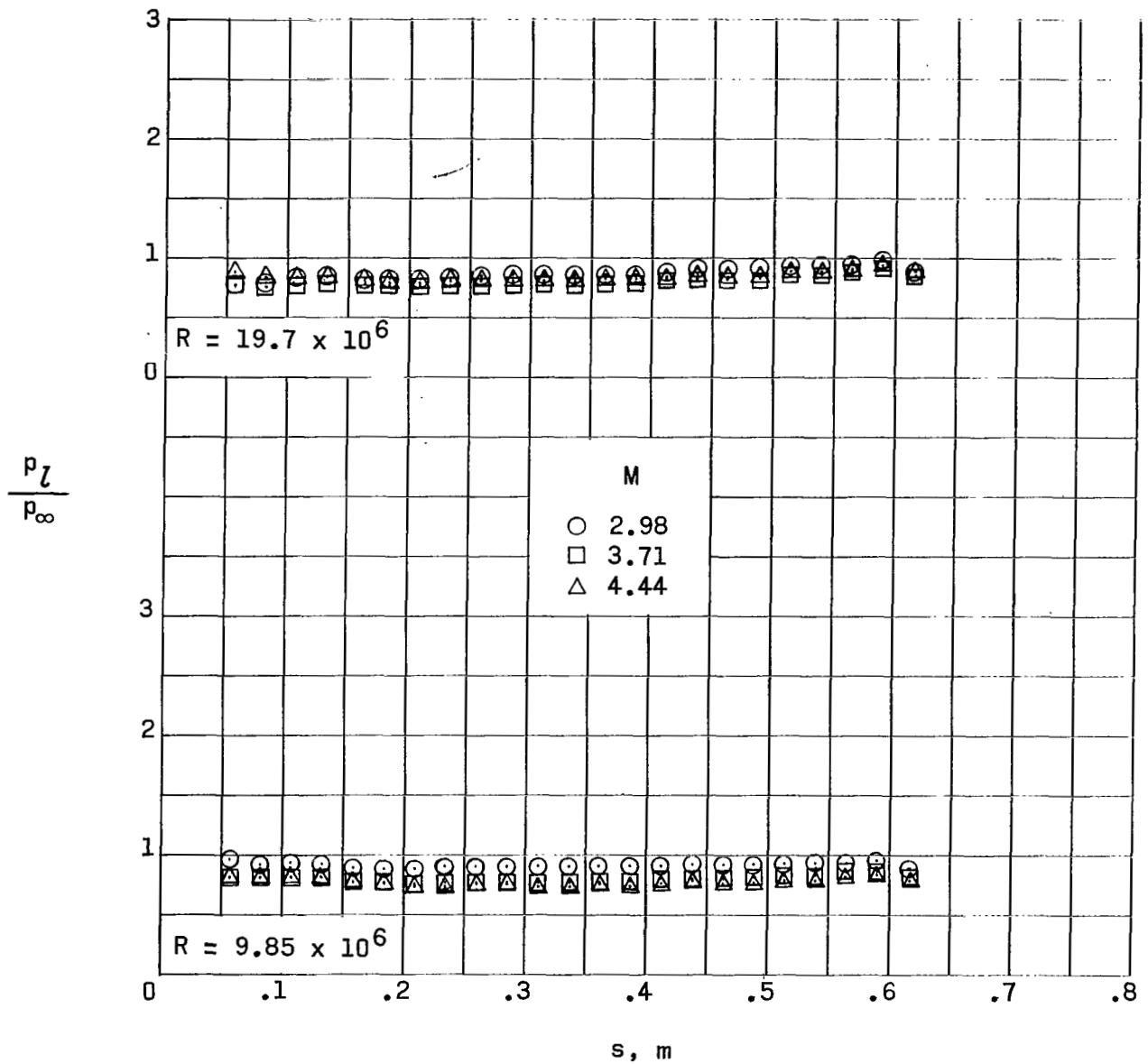
Figure 13.- Effect of Mach number on the surface-pressure distributions of configuration 4. $\alpha = 0^0$; $y = 0.076$ m; $\Lambda = 70^0$; $r \approx 0$ cm.
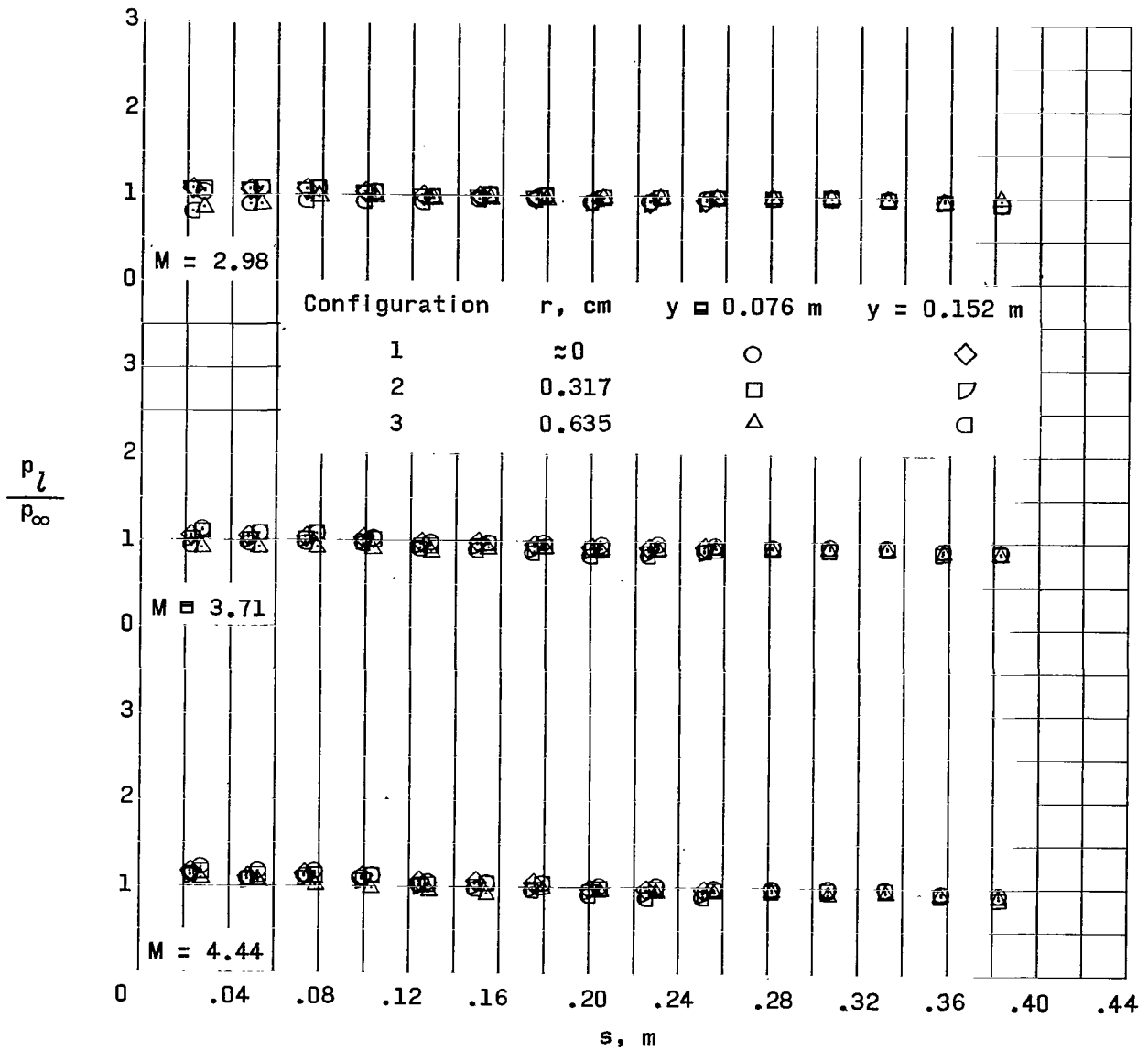
(a) R = 9.85 × 10⁶.

Figure 14.- Effect of leading-edge bluntness on the surface-pressure distributions of model 1. α = 0°; Λ = 60°.
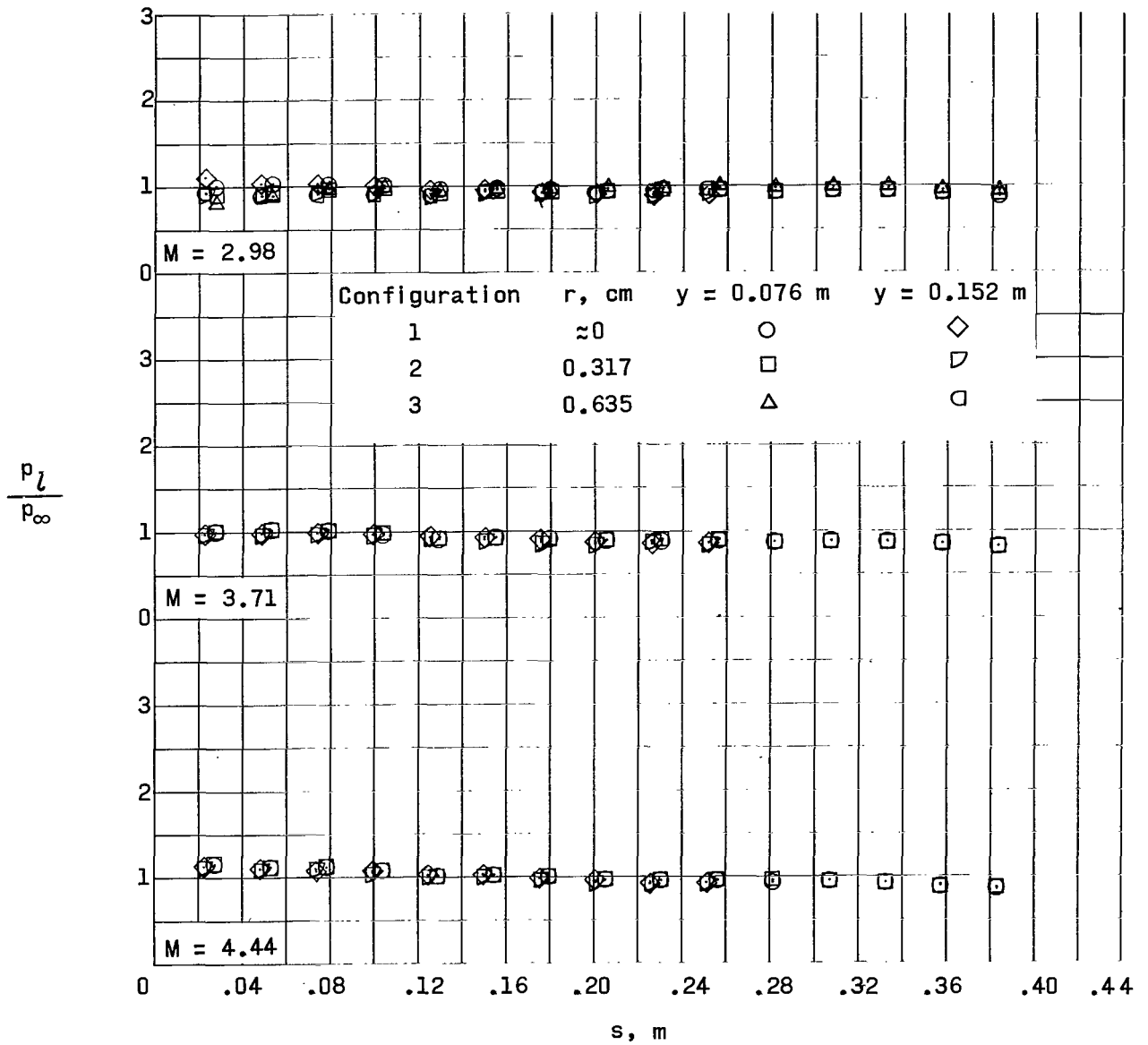
(b) $R = 19.7 \times 10^6$.

Figure 14.- Concluded.

$\dfrac{p_l}{p_\infty}$

M = 2.98

Configuration	r, cm	y ▫ 0.076 m	y = 0.152 m
4	≈ 0	○	◇
5	0.317	□	▽
6	0.635	△	◁

M = 3.71

M = 4.44

s, m
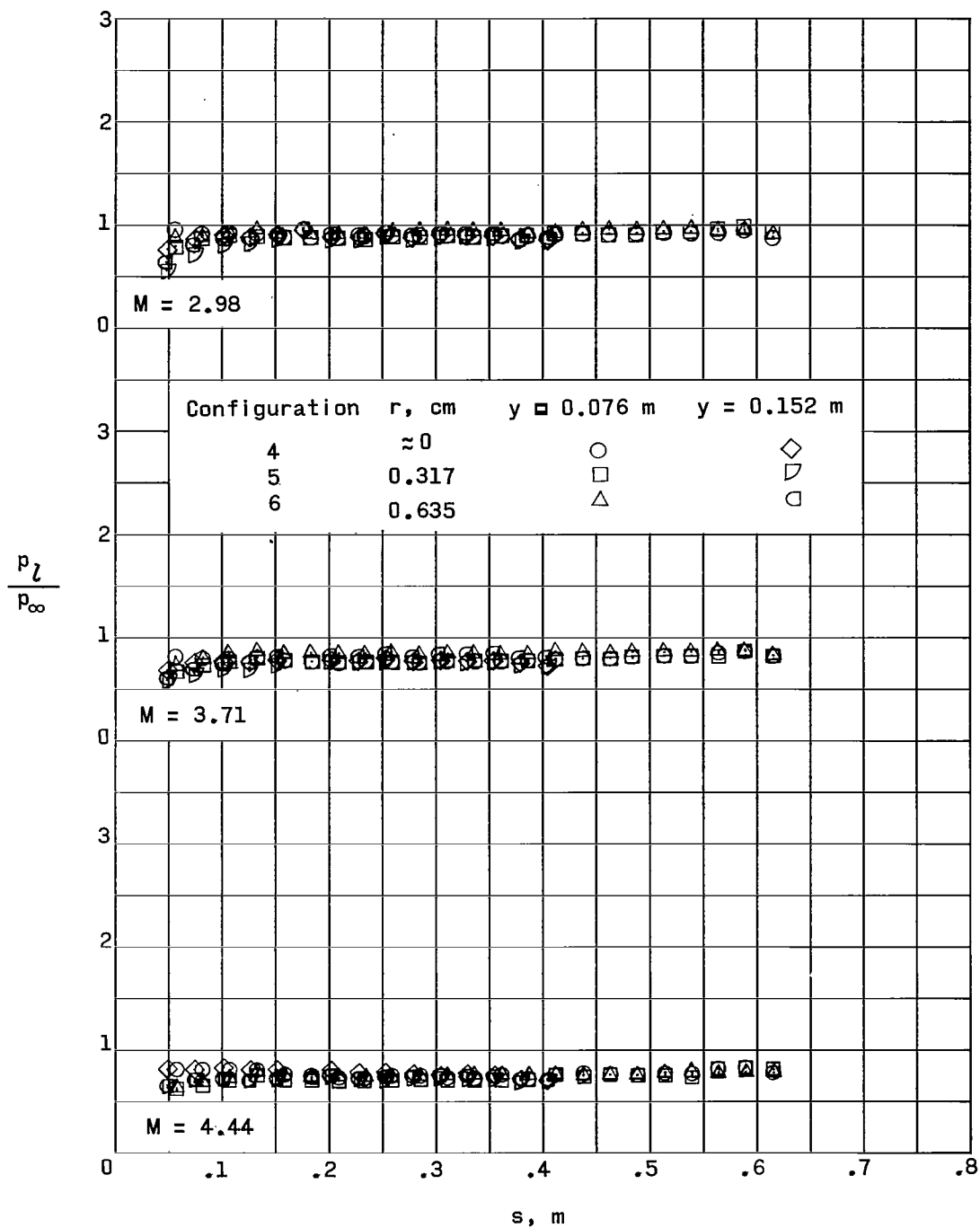
(a) R = 9.85 × 10^6.

Figure 15.- Effect of leading-edge bluntness on the surface-pressure distributions of model 2. α = 0°; Λ = 70°.

(b) $R = 19.7 \times 10^6$.

Figure 15.- Concluded.
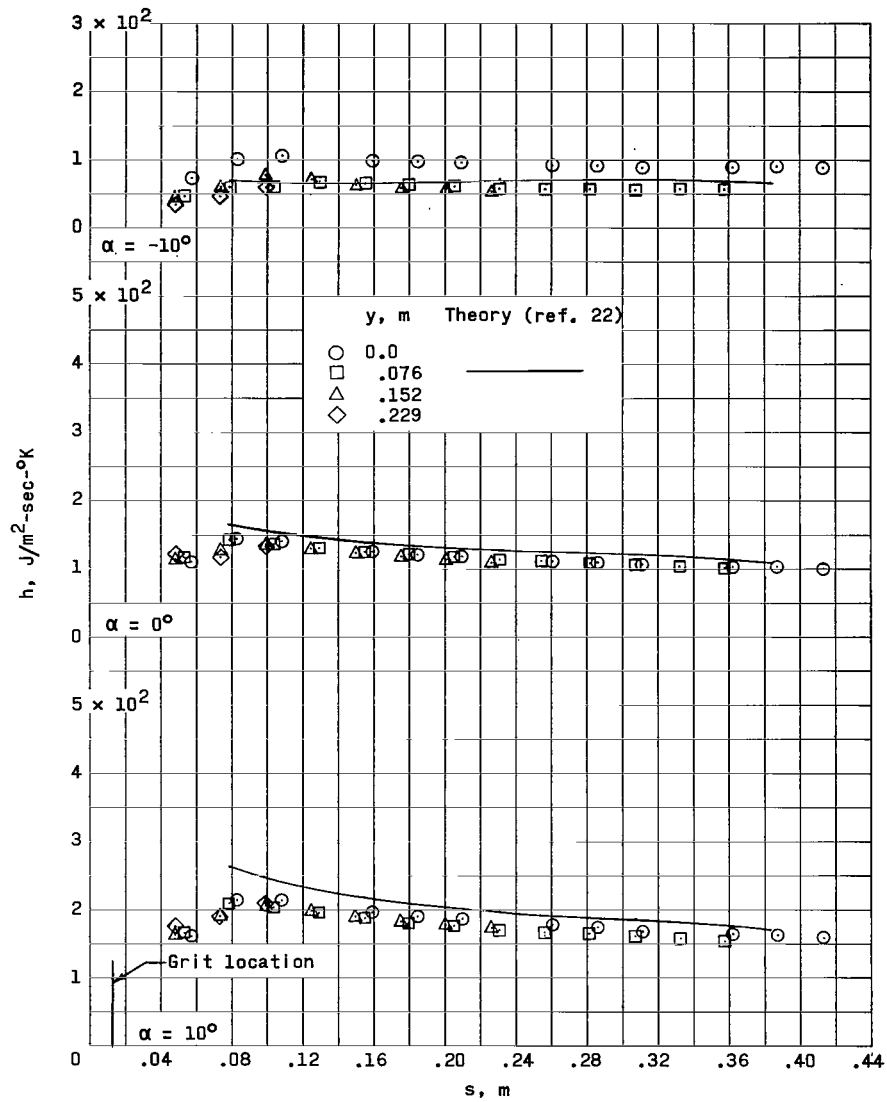
(a) M = 2.98; R = 9.85 × 10⁶.

Figure 16.- Effect of angle of attack on the heat-transfer coefficient distributions of configuration 1. Λ = 60⁰; r ≈ 0 cm.
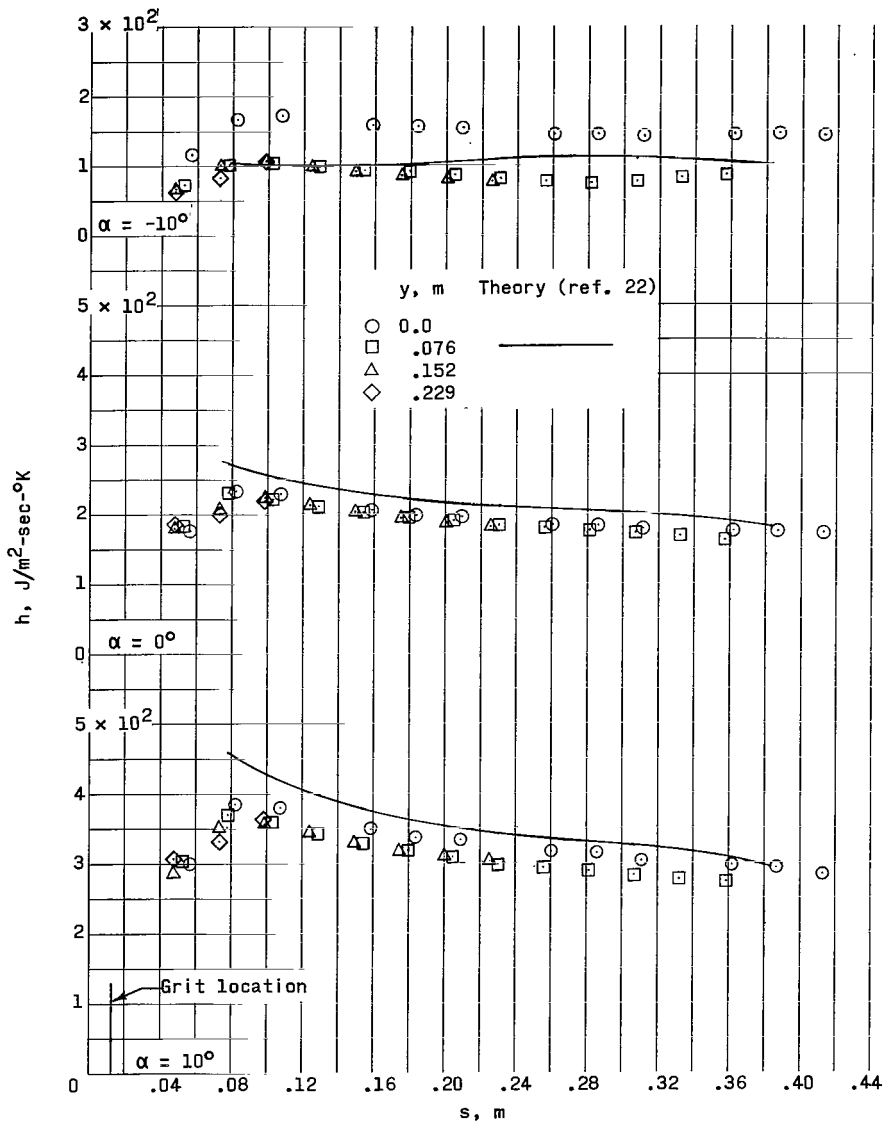
(b) M = 2.98; R = 19.7 × 10^6.

Figure 16.- Continued.
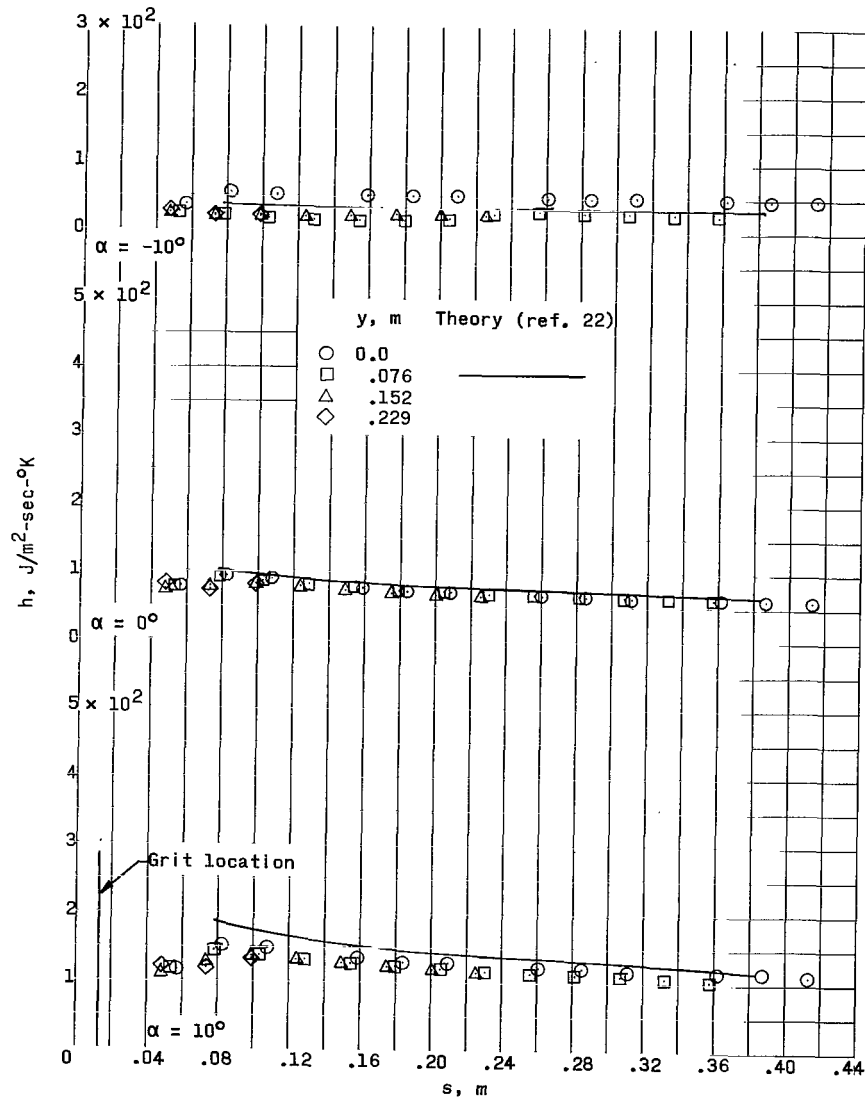
(c) M = 3.71; R = 9.85 × 10⁶.

Figure 16.- Continued.

(d) M = 3.71; R = 19.7 × 10⁶.

Figure 16.- Continued.

(e) $M = 4.44$; $R = 9.85 \times 10^6$.

Figure 16.- Continued.

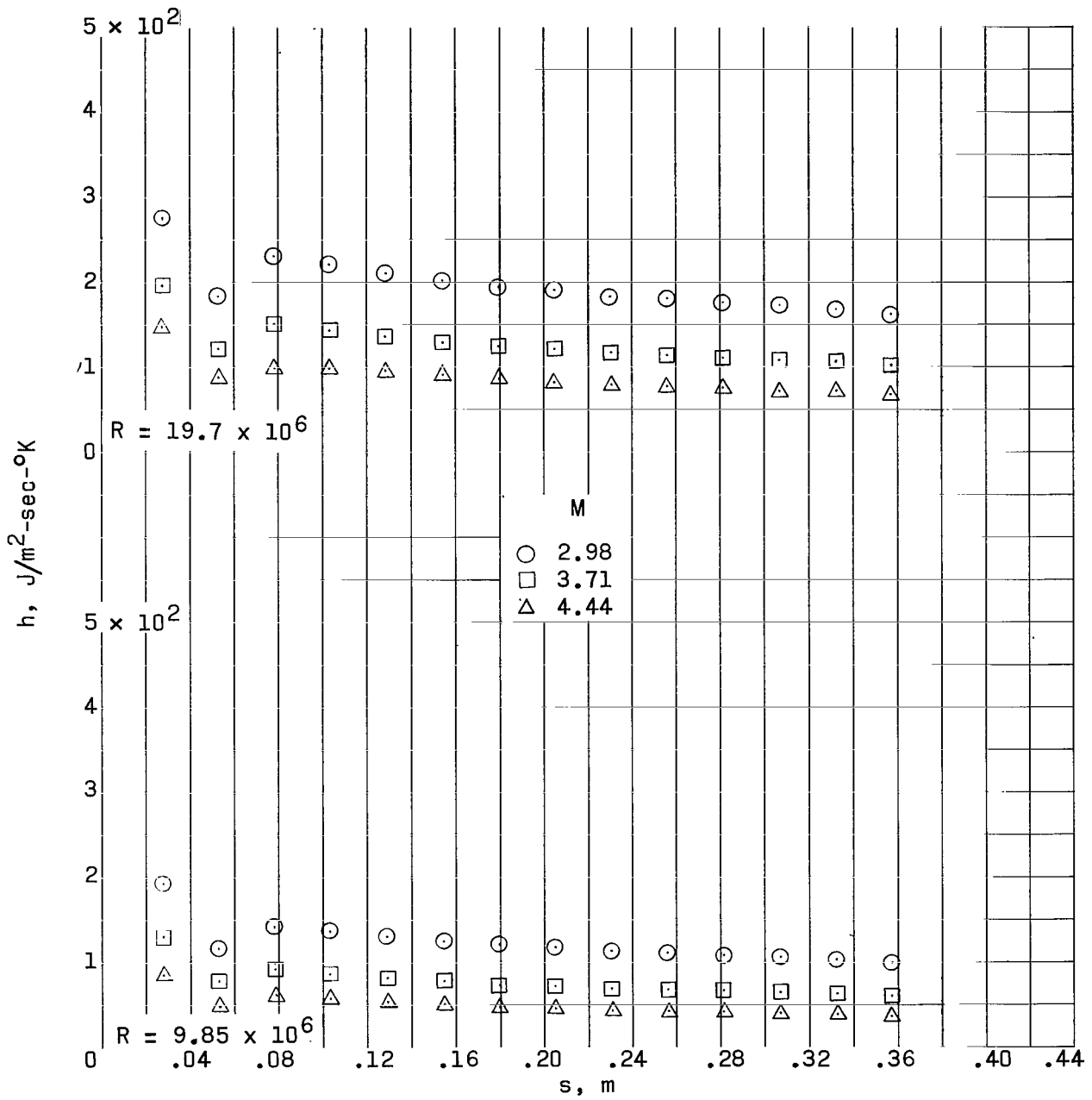(f) $M = 4.44$; $R = 19.7 \times 10^6$.

Figure 16.- Concluded.

(a) M = 2.98; R = 9.85 × 10⁶.

Figure 17.- Effect of angle of attack on the heat-transfer coefficient distributions of configuration 4. $\Lambda = 70^0$; $r \approx 0$ cm.

(b) M = 2.98; R = 19.7 × 10⁶.

Figure 17.- Continued.

(c) M = 3.71; R = 9.85 × 10⁶.

Figure 17.- Continued.

65
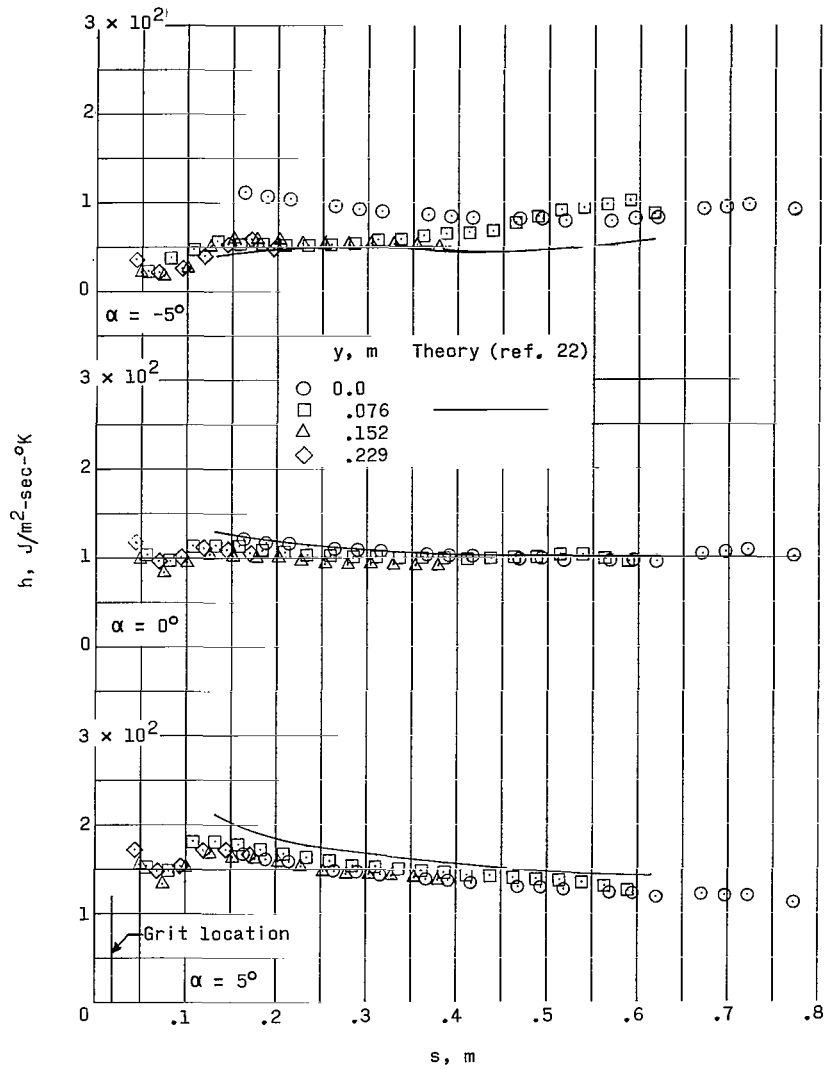
(d) M = 3.71; R = 19.7 × 10^6.

Figure 17.- Continued.
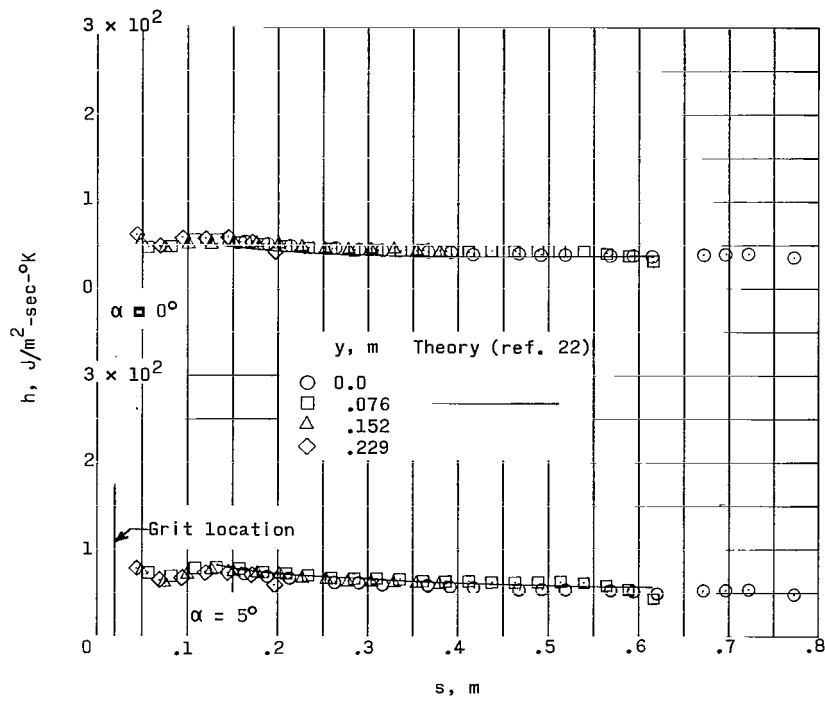
(e) M = 4.44; R = 9.85 × 10⁶.

Figure 17.- Continued.
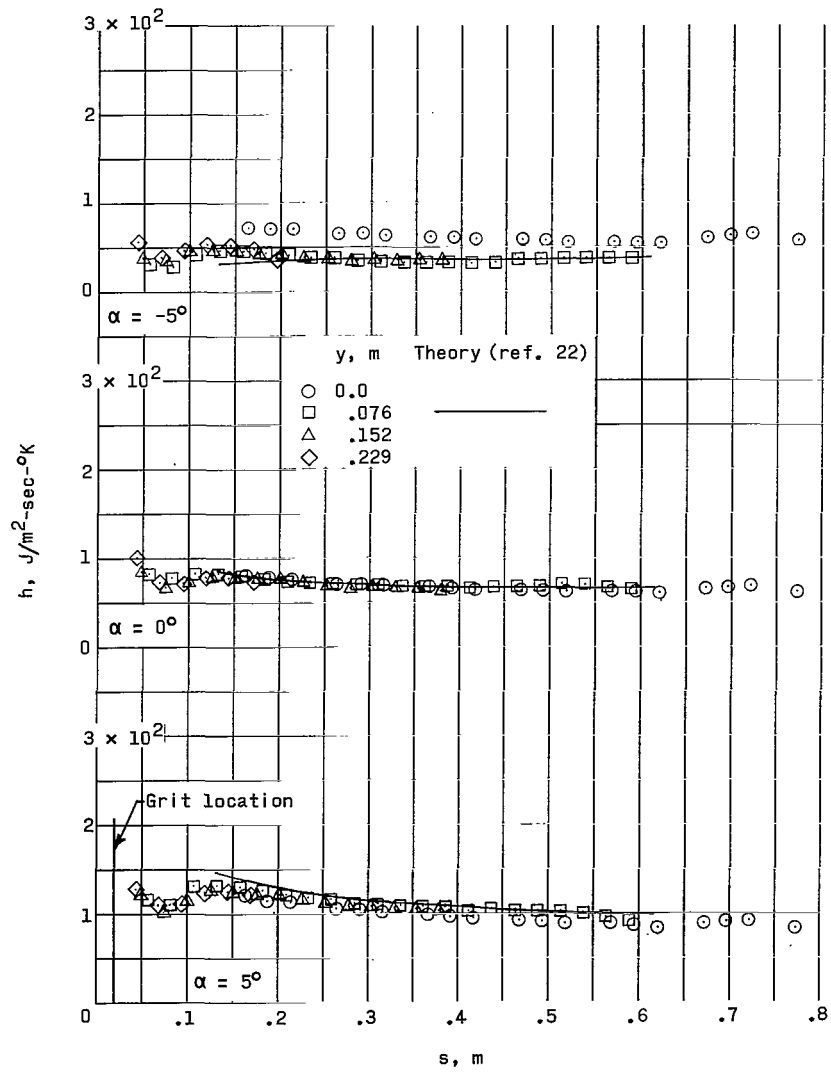
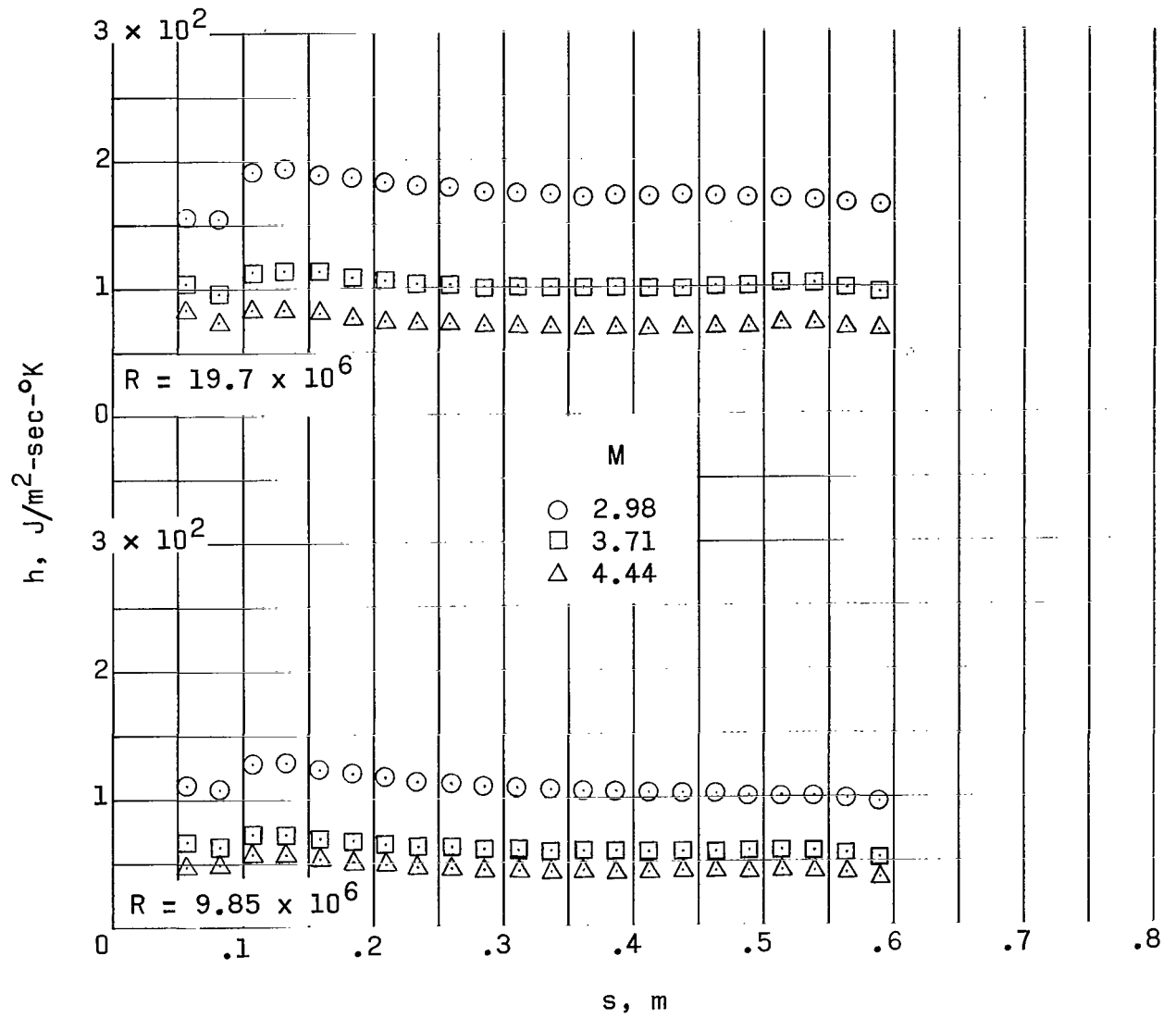(f) $M = 4.44$; $R = 19.7 \times 10^6$.

Figure 17.- Concluded.

Figure 18.- Effect of Mach number on the heat-transfer coefficient distributions of configuration 1. $\alpha = 0^0$; $y = 0.076$ m; $\Lambda = 60^0$; $r \approx 0$ cm.
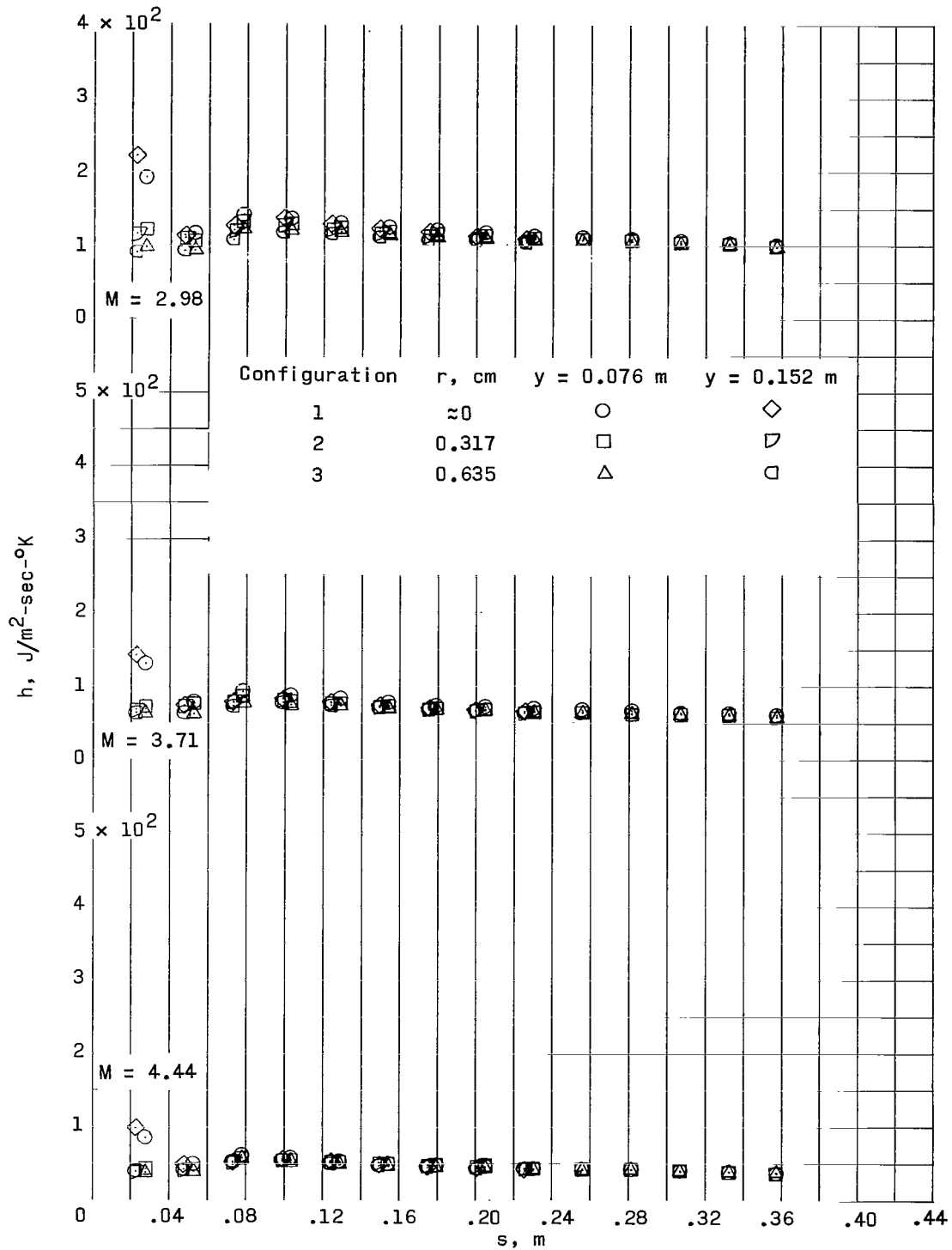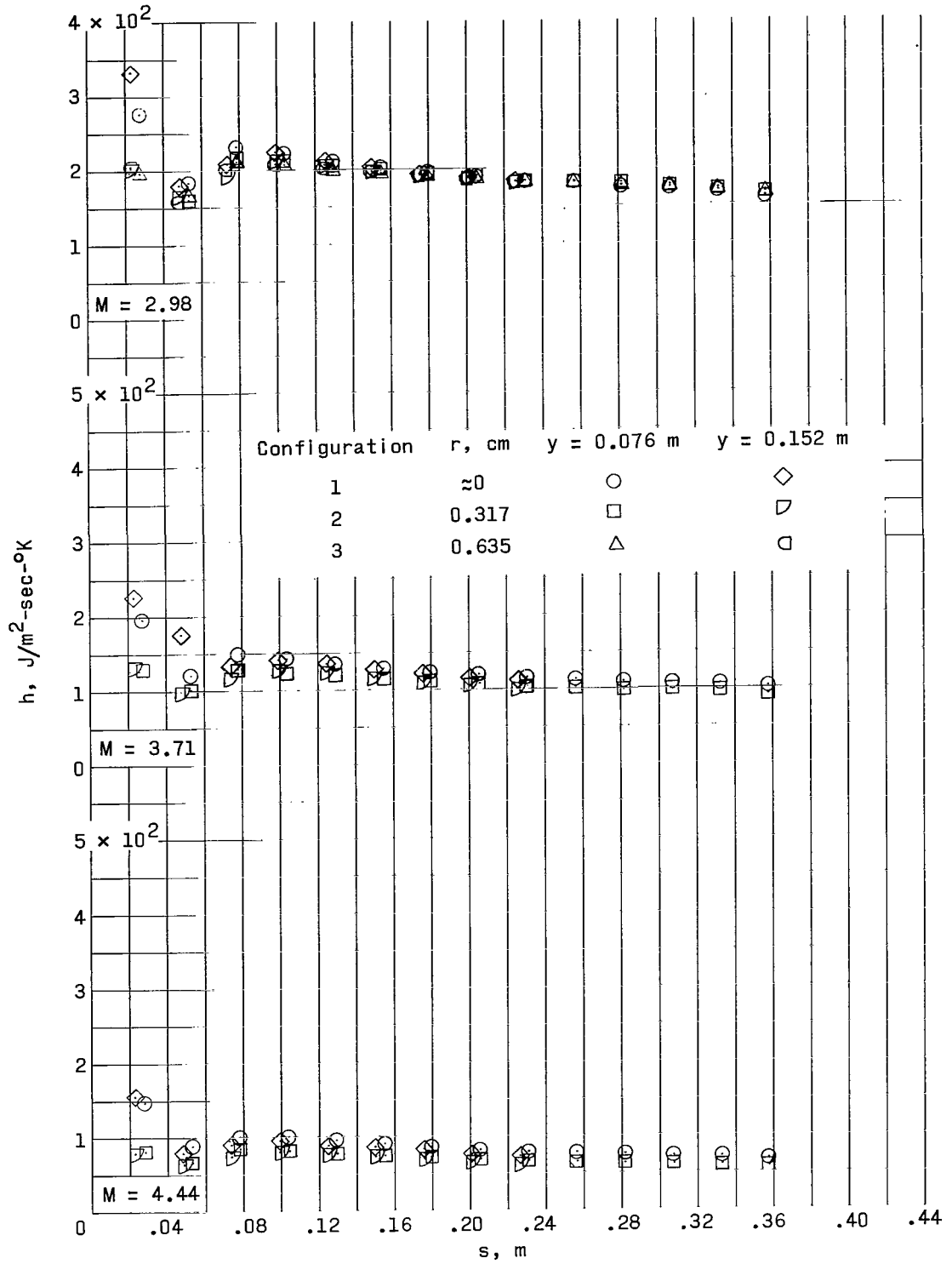
Figure 19.- Effect of Mach number on the heat-transfer coefficient distributions of configuration 4. $\alpha = 0^0$; $y = 0.076$ m; $\Lambda = 70^0$; $r \approx 0$ cm.
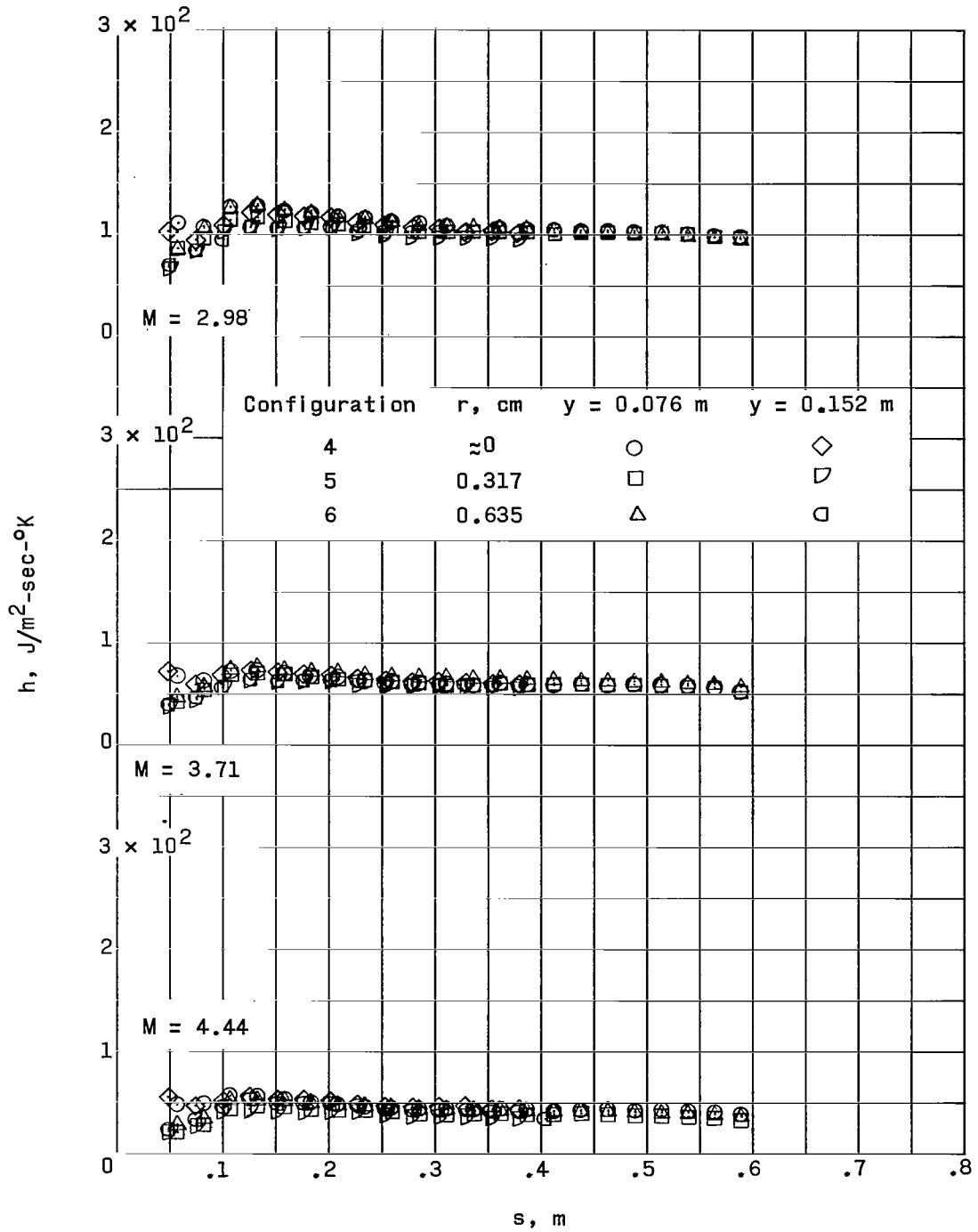
(a) $R = 9.85 \times 10^6$.

Figure 20.- Effect of leading-edge bluntness on the heat-transfer coefficient distributions of model 1. $\alpha = 0^0$; $\Lambda = 60^0$.

(b) R = 19.7 × 10⁶.

Figure 20.- Concluded.

(a) R = 9.85 × 10⁶.

Figure 21.- Effect of leading-edge bluntness on the heat-transfer coefficient distributions of model 2. $\alpha = 0^0$; $\Lambda = 70^0$.

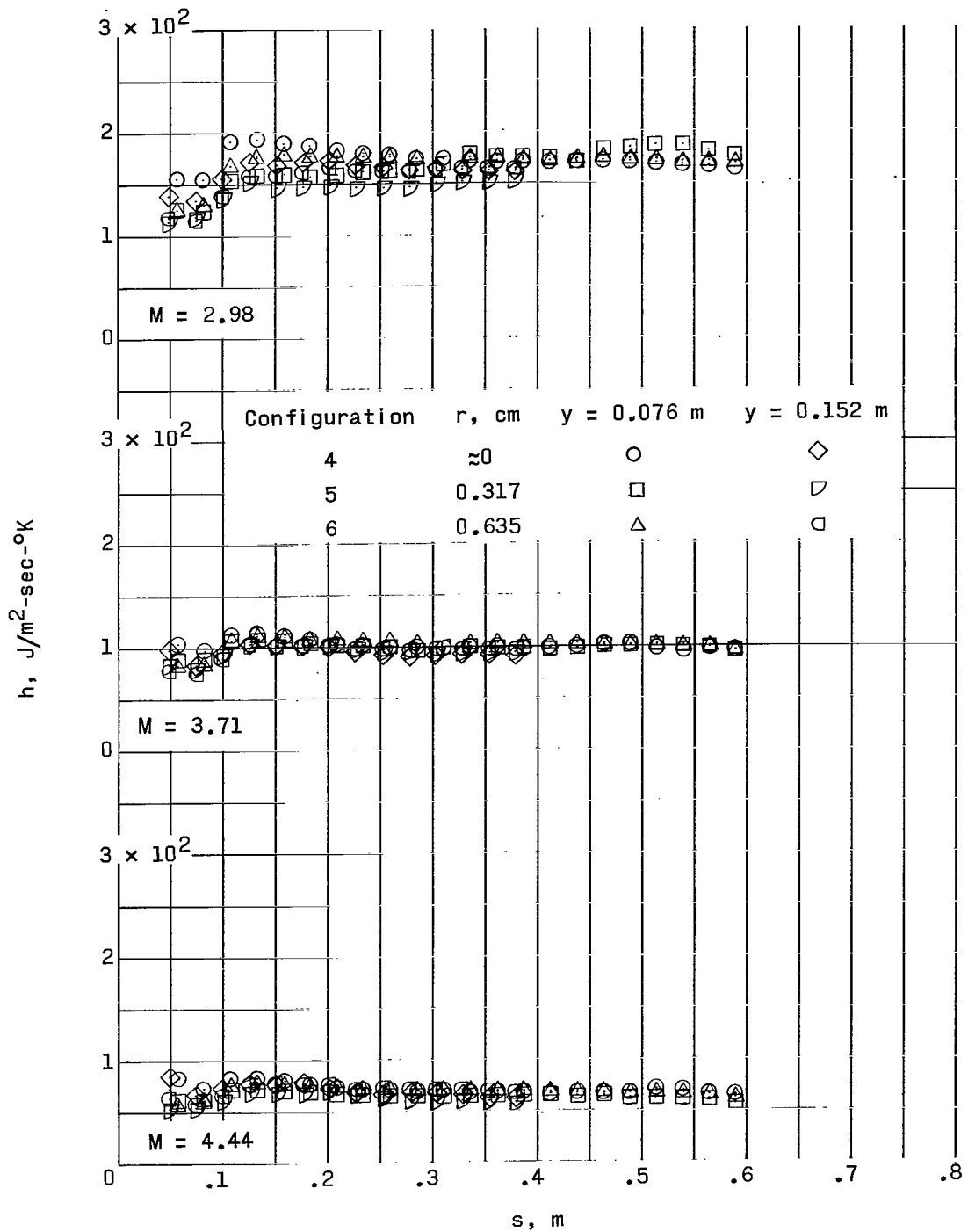(b) R = 19.7 × 10^6.

Figure 21.- Concluded.

"The aeronautical and space activities of the United States shall be conducted so as to contribute . . . to the expansion of human knowledge of phenomena in the atmosphere and space. The Administration shall provide for the widest practicable and appropriate dissemination of information concerning its activities and the results thereof."

—NATIONAL AERONAUTICS AND SPACE ACT OF 1958

NASA SCIENTIFIC AND TECHNICAL PUBLICATIONS

TECHNICAL REPORTS: Scientific and technical information considered important, complete, and a lasting contribution to existing knowledge.

TECHNICAL NOTES: Information less broad in scope but nevertheless of importance as a contribution to existing knowledge.

TECHNICAL MEMORANDUMS: Information receiving limited distribution because of preliminary data, security classification, or other reasons.

CONTRACTOR REPORTS: Technical information generated in connection with a NASA contract or grant and released under NASA auspices.

TECHNICAL TRANSLATIONS: Information published in a foreign language considered to merit NASA distribution in English.

TECHNICAL REPRINTS: Information derived from NASA activities and initially published in the form of journal articles.

SPECIAL PUBLICATIONS: Information derived from or of value to NASA activities but not necessarily reporting the results of individual NASA-programmed scientific efforts. Publications include conference proceedings, monographs, data compilations, handbooks, sourcebooks, and special bibliographies.

Details on the availability of these publications may be obtained from:

SCIENTIFIC AND TECHNICAL INFORMATION DIVISION

NATIONAL AERONAUTICS AND SPACE ADMINISTRATION

Washington, D.C. 20546